

**Optical investigation of cyclic variability
in direct-injection spark-ignition engines**

Von der Fakultät für Ingenieurwissenschaften, Abteilung Maschinenbau und
Verfahrenstechnik der

Universität Duisburg-Essen

zur Erlangung des akademischen Grades

einer

Doktorin der Ingenieurwissenschaften

Dr.-Ing.

genehmigte Dissertation

von

Judith Laichter

aus

Oberhausen

Gutachter: Univ.-Prof. Dr.-Ing. Sebastian Kaiser
Dr. Brian Peterson

Tag der mündlichen Prüfung: 08.03.2024

Acknowledgement

First and foremost, I would like to express my appreciation to my PhD supervisor Sebastian A. Kaiser. Thank you for guiding me with your advice and patience during this research journey. Your support has played a significant role in both my academic and personal growth. I am truly grateful to have had you as a mentor, and I know I owe much of my current success to your influence.

I would like to extend my sincere appreciation to Ales Srna, my supervisor during my time at Sandia National Laboratories. Ales shared his knowledge and experience with me and contributed to the quality of this work by asking the right questions. Working together evolved into a meaningful friendship. I am grateful for the opportunities he provided, and the great teamwork.

I want to thank my colleagues, whose collaboration have enriched my research experience. The sharing of ideas and the shared quest of knowledge within our academic community played a significant role in expanding my viewpoints. My special gratitude goes to Niklas Jüngst and Jonas Kühlmann, whose friendship and shared laughter were a source of strength and comfort during the tough times in my PhD journey. I would also like to thank Natascha Schlösser, Erdal Akyildiz, Jörg Albrecht, Beate Endres and Birgit Nelius for their support in the laboratory and wherever help was needed. Without their commitment, I would not have been able to successfully complete the experiments. Special thanks go to Barbara Nota, Kerstin Czaplinski and Sonay Saritas for their efficient administration and prompt handling of purchasing.

I want to thank my friends and family for always having my back. Their support and understanding kept me going through the ups and downs of this academic journey. A heartfelt thank you to Katja Adolph for being an incredible friend and continually inspiring me with her encouragement. Your belief in me has strengthened my commitment to push through. And last but not least, I would like to thank my boyfriend, Dennis. Your consistent support during both the successes and challenges, along with your understanding of my work, has been incredibly valuable.

Abstract

Optical diagnostics were used in two different single-cylinder research engines to investigate cycle-to-cycle variations (CCV). A range of physical characteristics, including the flow field, mixture formation, and flame propagation, were measured in two dimensions and subsequently combined with pressure-based analysis. Fuel was primarily injected through direct-injection (DI). Depending on the specific aspects of the study reference cases with port-fuel injection (PFI) were also measured. By varying parameters like injection timing, injection pressure, and ignition location the impact of the resulting changes in flow field and fuel concentration at ignition on CCV was investigated.

To determine the in-cylinder flow field, particle image velocimetry (PIV) was performed. Laser-induced fluorescence (LIF) of a tracer (anisole or di-fluorobenzene) evaporated into the fuel allowed examining mixture formation at selected crank angles during the compression stroke. The natural chemiluminescence of the flame was used to image flame growth and movement. Subsequently, the acquired data was analyzed and correlated in conditional averages, correlation maps, and independent component analysis (ICA) – the latter being further developed here specifically for analysis of engine CCV.

In the case of a homogeneous air-isooctane mixture delivered via PFI, it was observed that in slower cycles, the flame tends to move closer to the intake side of the spark plug. With inhomogeneous mixtures provided by DI the flame preferentially burns towards the exhaust side. Flames in fast cycles, on the other hand, increasingly burn centrally in the combustion chamber for both types of mixtures. Particularly with PFI, flow field analysis showed different movements of the vortex centers for fast and slow combustion, which were further investigated through ICA. The results of this analysis reveal various flow patterns that correlate with the combustion speed.

Correlation maps of the flow field and flame growth showed regions that correlate with the combustion process, often deviating from the location of the tumble vortex center. With DI, correlations between the equivalence ratio and combustion speed showed a significant impact of the mixture gradient on combustion behavior.

In the second part of this work, iso-octane was replaced with hydrogen (H_2). In motored operation, the variability of mixture formation was investigated. As expected, retarding injection timing and reducing injection pressure increases mixture inhomogeneity in some regions of the combustion chamber. A subsequent analysis with fired operation demonstrated that later injection timings reduce combustion CCV. This suggests that in terms of CCV, the benefits of increased turbulence associated with later injections outweigh the drawbacks of mixture inhomogeneity in the given experimental conditions.

Kurzfassung

Zur Untersuchung von zyklischen Schwankungen (CCV) wurden verschiedene optische Diagnostiken in zwei verschiedenen Einzylinder-Forschungsmotoren eingesetzt. Eine Reihe von physikalischen Größen, darunter das Strömungsfeld, die Gemischbildung und die Flammenausbreitung, wurden zweidimensional gemessen und anschließend mit druckbasierten Analysen kombiniert. Der Kraftstoff wurde hauptsächlich durch Direkteinspritzung (DI) eingespritzt. Je nach den spezifischen Aspekten der Studie wurden auch Referenzfälle mit Saugrohr-Einspritzung (PFI) gemessen. Durch Variation von Parametern wie Einspritzzeitpunkt, Einspritzdruck und Zündort wurden die Auswirkungen der daraus resultierenden Änderungen des Strömungsfeldes und der Kraftstoffkonzentration bei der Zündung auf die CCV untersucht.

Zur Bestimmung des Strömungsfeldes im Zylinder wurde Particle Image Velocimetry (PIV) durchgeführt. Die laserinduzierte Fluoreszenz (LIF) eines in den Kraftstoff eingebrachten Tracers (Anisol oder Di-Fluorbenzol) ermöglichte die Untersuchung der Gemischbildung bei ausgewählten Kurbelwinkeln während des Verdichtungstaktes. Die natürliche Chemilumineszenz der Flamme wurde zur Darstellung von Flammenwachstum und -bewegung genutzt. Anschließend wurden die gewonnenen Daten mit Hilfe von konditionierten Mittelwerten, Korrelationskarten und der Independent Component Analysis (ICA) analysiert und korreliert - letztere wurde hier speziell für die Analyse der CCV des Motors weiterentwickelt.

In einem homogenen Luft-Isoktan-Gemisch bewegt sich die Flamme in langsameren Zyklen tendenziell in Richtung der Ansaugseite der Zündkerze. Bei inhomogenen Gemischen, die durch DI bereitgestellt werden, brennt die Flamme vorzugsweise zur Auslasseite hin. In schnellen Zyklen verbleibt die Flamme hingegen zentral im Brennraum für beide Arten von Gemischen. Insbesondere bei PFI zeigte die Strömungsfeldanalyse unterschiedliche Bewegungen der Wirbelzentren bei schneller und langsamer Verbrennung, die mittels ICA weiter untersucht wurden. Die Ergebnisse dieser Analyse zeigen verschiedene Strömungsmuster welche mit der Verbrennungsgeschwindigkeit korrelieren.

Korrelationskarten des Strömungsfeldes und des Flammenwachstums zeigen Regionen, die mit dem Verbrennungsprozess korrelieren und oft von der Lage des Tumble-Wirbelzentrums abweichen. Bei DI zeigen die Korrelationen zwischen dem Äquivalenzverhältnis und der Verbrennungsgeschwindigkeit einen signifikanten Einfluss des Gemischgradienten auf das Verbrennungsverhalten.

Im zweiten Teil dieser Arbeit wurde Iso-Oktan durch Wasserstoff ersetzt. Im gefeuerten Betrieb führte eine höhere Inhomogenität durch spätere Einblasung zu weniger CCV. Dies deutet darauf hin, dass unter den gegebenen Versuchsbedingungen die Vorteile der mit den späteren Einspritzungen verbundenen erhöhten Turbulenz die Nachteile der Inhomogenität des Gemischs aufwiegen.

List of symbols

Symbol	Meaning	Unit
A	Mixture matrix	m/s / pixel
A_{flame}	Equivalent flame area	mm ²
f_n	Two-dimensional flow field	m/s / pixel
f_A, f_B	Velocity vectors	m/s
$ f_A , f_B $	Velocity magnitude	m/s
I	Fluorescence intensity	Counts
I_{DI}	Intensity image with direct injection	Counts/pixel
I_{PFI}	Intensity image with port fuel injection	Counts/pixel
I_L	Incident laser light intensity	Counts
$I_{\phi, DI}$	Equivalence ratio image	-/pixel
k_{fl}	Rate of spontaneous fluorescence	s ⁻¹
$\tilde{k}_q^{O_2}$	Bimolecular quenching rate coefficient of oxygen	m ³ /s
k_{tot}	Rates of all other deexcitation mechanisms	s ⁻¹
m, n	Number of rows and columns, respectively	-
m_{air}	Air mass	kg
$m_{air, stoich}$	Stoichiometric air mass	kg
n_i	Number density of the bath gas composition	cm ⁻³
n_{oxy}	Oxygen number density	cm ⁻³
n_{tr}	Tracer number density	cm ⁻³
p	Pressure	Pa
p_{ind}	Indicated mean effective pressure	
P_{inj}	Injection pressure	bar
r_{flame}	Equivalent flame radius	mm
$R_{x,y}$	Correlation coefficient	-
$ R_{x,y} $	Correlation coefficient magnitude	-
RI	Relevance index	-
$ RI $	Magnitude of the relevance index	-
\overline{RI}	Average relevance index	-
$ \overline{RI} $	Average magnitude of the relevance index	-
s_n	Two-dimensional independent flow structure	m/s per pixel
t	Time	s
T	Temperature	K
v	Velocity	m/s
$ v $	Velocity magnitude	m/s
V	Volume	m ³
W	Indicated Work	J
\mathbf{W}	Reciprocal of A	s/m / pixel
x_i	$ v $ or ϕ	m/s or -

\bar{x}	Average of x_i	m/s or -
y_i	r_{flame} or CA10	mm or °CA
\bar{y}	Average of y_i	mm or °CA
Δt	Temporal differences (e.g., delay)	μs
λ	Air/fuel ratio	-
η	Detection efficiency	-
Π	Collection efficiency	-
σ_{abs}	Absorption cross section	mm^2
σ_{IMEP}	Standard deviation in IMEP	bar
ϕ	Fuel/air ratio	-
Φ_{fl}	Fluorescence quantum yield	-

List of abbreviations

Abbreviation	Description
BDC	Bottom dead center (piston position)
BG	Background
CA	Crank angle
CCD	Charge-coupled device
CCV	Cycle-to-cycle variations
CFD	Computational fluid dynamics
CMOS	Complementary metal-oxid semiconductor
COV	Coefficient of variation
DBI	Diffuse-Background illumination
DFB	1,4-difluorobenzene
DI	Direct injection
ECN	Engine combustion network
EGR	Exhaust gas recirculation
FARLIF	Fuel/air ratio LIF
FF	Flat field
FFT	Fast-Fourier transformation
FOV	Field of view
FQY	Fluorescence quantum yield
FWHM	Full width at half maximum
HHR	Heat-release rate
HS	High speed
ICE	Internal combustion engine
ICCD	Intensified CCD-camera
IMEP	Indicated mean effective pressure
IRO	Intensified relay optics
IVC	Intake valve closing
LES	Large eddy simulation
LIF	Laser induced fluorescence
Nd:YAG	Neodymium-doped yttrium aluminum garnet
Nd:YVO ₄	Neodymium-doped yttrium orthovanadate
PFI	Port fuel injection
PIV	Particle image velocimetry
ROI	Region of interest
rpm	Revolutions per minute
SI	Spark ignition
SOI	Start of injection
TDC	Top dead center (piston position)
UV	Ultraviolet

Table of contents

Acknowledgement	I
Abstract	III
Kurzfassung	V
List of symbols	VII
List of abbreviations	IX
Table of contents	XI
1 Introduction	1
2 Cyclic variability and optical diagnostics in SI engines.....	4
2.1 Four-stroke engine cycle	4
2.2 Fuel injection	6
2.3 Cyclic variations in SI engines	6
2.4 Optical diagnostics for internal combustion engines.....	12
2.5 Optically accessible engine	19
2.6 Light sources and detectors	21
3 Effects of different injections strategies on CCV in an isoctane-fueled SI engine	24
3.1 State of the art.....	24
3.2 Experimental setup	25
3.3 Results	29
3.4 Chapter conclusions.....	37
4 Statistical analysis of flow field variations via independent component analysis.....	38
4.1 State of the art.....	38
4.2 Experimental set-up and PIV measurements.....	39
4.3 Methodology.....	42
4.4 Results	50
4.5 Chapter conclusion	57
5 Analysis of the mixture distribution in a hydrogen-fueled heavy-duty engine	58
5.1 State of the art.....	58
5.2 Heavy-duty optical engine.....	60
5.3 Results	68
5.4 Chapter conclusion	87
6 Cyclic variability in a hydrogen-fueled heavy-duty engine	88

6.1	State of the art	88
6.2	Heavy-duty optical engine and operating conditions.....	89
6.3	Results.....	94
6.4	Chapter conclusion.....	111
7	Conclusions and future work	113
7	Bibliography.....	116
7.1	References.....	116
7.2	Contributions of the author	128
8	Appendix.....	130

1 Introduction

Motivation

The goal set by the German Government is to achieve a 55% reduction in greenhouse gas emissions by 2030, in comparison to the level in 1990. While Germany has made significant strides in reducing greenhouse gas emissions since 1990, progress in the transportation sector has been rather limited. The proportion of emissions originating from transportation has climbed from approximately 13% in 1990 to 19.4% in 2021. This increase is primarily attributed to the continued expansion of road freight transport and motorized individual transport [1]. In the year 2021, the transportation sector was almost completely dependent on fossil fuels, accounting for approximately 98.1% of the total energy consumption, with electricity contributing a mere 1.9%. Even though the government has been promoting electrified cars for years, it is clear that fossil fuels will remain indispensable for the foreseeable future. This implies that greenhouse gas emissions cannot be completely avoided in this sector. Overall, the increasing scarcity of resources and rising environmental impacts highlight the importance of economic and ecological aspects in the provision of energy. Particularly important is the improvement of the combustion processes, especially in terms of thermal efficiency.

Recent efforts to enhance the efficiency of gasoline engines have primarily focused on reducing charge cycle losses, especially in the partial load range. Various concepts have been proposed and investigated for this purpose including lean-burn, stratified spark-ignition (SI) combustion processes as well as homogeneous and partially homogeneous compression-ignition processes. Lean combustion is still the most effective method for increasing efficiency and also offers advantages in terms of particle emissions. However, these concepts are not yet suitable for global use due to the fuel quality requirements of the exhaust gas aftertreatment system. The combination of direct injection (DI) and downsizing, along with turbocharging, has established itself as a globally applicable technology in a large number of engines [2–4]. An optimally controlled combustion is important for all these processes, but this is limited by various factors.

A significant challenge is ensuring the stability of combustion. Especially gasoline engines suffer from cycle-to-cycle variations (CCV) during operation. The term combustion CVV initially refers to the change in easily measurable operating parameters such as maximum cylinder pressure or indicated mean effective pressure (IMEP). In extreme cases, these variations can lead to misfires or knocking combustion. For the conventional SI engine with homogeneous gasoline-air mixture, strategies exist to avoid such extreme cases and ensure stable engine operation. However, these strategies often come with a reduction in efficiency.

With the development of downsized engines, the unresolved question of the root causes of CCV persists. These variations, particularly in highly optimized operating points, can adversely affect the combustion process. A detailed understanding of the causes of cyclic variations could empower engine manufacturers to either counteract instabilities and conduct more targeted optimization. In general, the challenge lies in operating engines as close as possible to the

stability limit to enable optimization for efficiency and pollutant emissions. However, phenomena that negatively impact engine operation, such as knocking, incomplete combustion, or misfires, must be avoided.

Despite the importance of CCV, the fundamental reasons for its occurrence have not yet been fully clarified or predictably described. It is important to understand the underlying phenomena and to integrate this knowledge into numerical models in such a way that both the probability and the thermodynamic effects of CCV can be predicted by numerical simulations. This is not yet possible, but would enable an improvement in efficiency and pollutant emissions during the development process.

Since there are only a few well-described benchmark experiments for internal combustion engines in the literature, there is a considerable need for reliable data to validate mathematical models in the context of numerical simulations. Validation data in the engine or in engine-like geometries with sufficient data accuracy and precise characterization of boundary conditions are rare, mainly available for highly simplified, non-reacting cases. For understanding and predicting CCV in the engine, a combined experimental-numerical analysis is indispensable. High-quality, engine-relevant experimental data provide detailed insights into in-cylinder processes, a prerequisite for causal chain analysis. Furthermore, they are essential for simulations of both DI and port fuel injection (PFI) gasoline engines, allowing the development and validation of improved physical models. It is important to test the models with experimental data for different geometries, operating conditions, and combustion strategies that are representative of highly optimized engine concepts.

Thesis Objectives

In this work experimental research on combustion CCV in direct-injection spark-ignition (DISI) engines was conducted, utilizing advanced optical diagnostic techniques. The primary goal of the investigations was to improve the fundamental understanding of what causes CCV while also supplying a reference for validating numerical modeling efforts. The peculiarity of the investigated phenomena is the strong impact of the flow field, mixture distribution and ignition on CCV, along with the extensive cause-and-effect relationships among them. This project focused on the impact of DI in SI engines and it was part of the Research Unit FOR 2687: “Zyklische Schwankungen in hochoptimierten Ottomotoren: Experiment und Simulation einer Multiskalen-Wirkungskette” funded by the Deutsche Forschungsgemeinschaft (DFG). The aim of the research unit was the systematic analysis of CCV as a prerequisite for the further optimization of modern SI engine combustion processes.

The first half of this thesis focuses on the influence of flow field and fuel/air mixing on the combustion speed in an optically accessible light-duty single-cylinder SI engine using iso-octane as a fuel. The testbench is located at the University of Duisburg-Essen. High-speed particle image velocimetry (PIV) and laser-induced fluorescence (LIF) were used to visualize the flow field and mixture distribution, respectively. The early flame propagation was captured by high-speed line-of-sight integrated imaging of the natural chemiluminescence of the flame.

Conditional averages were used to investigate the differences between fast and slow burning cycles for homogeneous and inhomogeneous operating conditions. A two-dimensional correlation analysis aimed to understand that part of the cyclic variabilities' causal chain that comprises injection – mixing – ignition – inflammation on a single-cycle basis. The application of independent component analysis (ICA) on the conducted flow fields revealed underlying “typical” flow patterns that are linked to the combustion speed.

The second half focuses on hydrogen (H_2) as a fuel and its impact on CCV. These experiments were performed in an optical heavy-duty engine located at Sandia National Laboratories and include similar optical diagnostic techniques as they were used in the first half of the thesis. By measuring the mixture distribution in different planes and at different crank angles via LIF, the influence of injection pressure and injection timing on the variability of mixture homogeneity and the associated NO_x emissions was investigated in motored operation. Complemented measurements of the natural luminosity of the chemically excited hydroxyl (OH^*) radicals in fired operation aimed to investigate the causal chain between the mixture distribution and the flame propagation that leads to a fast or slow combustion.

2 Cyclic variability and optical diagnostics in SI engines

2.1 Four-stroke engine cycle

The operation of a four-stroke SI engine is based on a cyclic process that is illustrated in Figure 1. This cycle, often referred to as the Otto cycle after its inventor Nikolaus Otto, consists of four distinct strokes: intake, compression, expansion, and exhaust. In total, these four strokes complete one engine cycle, and the crankshaft turns 720°CA (two full revolutions) for a four-stroke engine to complete a full cycle. These strokes work together to use the chemical energy stored in the fuel and convert it into mechanical work:

1) *Intake stroke* ($-360^{\circ}\text{CA} - -180^{\circ}\text{CA}$):

In the intake stroke the piston starts at top dead center (TDC) moving towards bottom dead center (BDC). The intake valve's opening occurs slightly prior to the piston reaching TDC and valve closing shortly after BDC. As the opening of the intake valve is synchronized with the downward movement of the piston, the air is drawn into the cylinder. If the engine is operated with PFI, the fuel is already injected into the intake manifold so that the engine draws in a mixture of air and fuel. With DI, only air is drawn in and the fuel is injected directly into the combustion chamber, either during the intake stroke or during the compression stroke [5].

2) *Compression stroke* ($-180^{\circ}\text{CA} - 0^{\circ}\text{CA}$):

The piston begins its upward movement, compressing the initial volume. This leads to an increase of the in-cylinder pressure and temperature. If the engine is operated with a late DI, the mixing of fuel and air takes place in compression stroke. The compression stroke lasts until TDC.

3) *Expansion stroke* ($0^{\circ}\text{CA} - 180^{\circ}\text{CA}$):

The expansion stroke begins at TDC. Ignition takes place before TDC and the resulting combustion of the fuel-air mixture releases heat. The expansion of the mixture pushes the piston downwards in the expansion stroke and the mechanical movement is transmitted to the wheels through a gearbox.

4) *Exhaust stroke* ($180^{\circ}\text{CA} - 360^{\circ}\text{CA}$):

The exhaust stroke begins at BDC. The exhaust valves open and the upward movement of the piston pushes the burnt gas out of the cylinder.

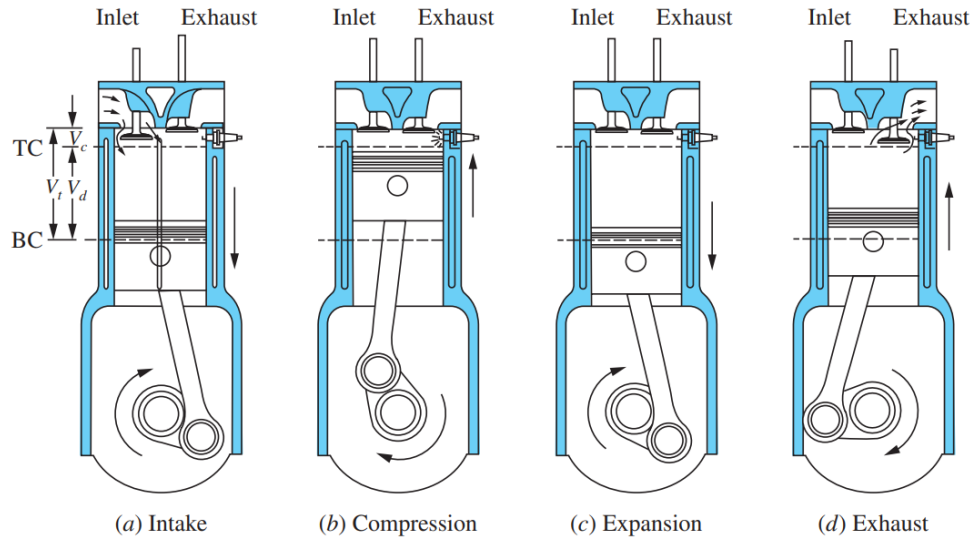


Figure 1. The four strokes of a SI engine. Taken from [5].

Figure 2 shows the four-stroke engine cycle in a p - V diagram, as it can be obtained by measuring the in-cylinder pressure as a function of the displacement volume V_h . Areas representing a gain in work are marked with \oplus , and areas causing an expenditure of work are marked with \ominus . The indicated work W performed per cycle and cylinder is obtained by the integral over the enclosed areas of the p - V diagram [6]. The indicated work W is defined as

$$W = \oint p dV \quad (1)$$

and the IMEP is described by

$$IMEP = \frac{W}{V_h}. \quad (2)$$

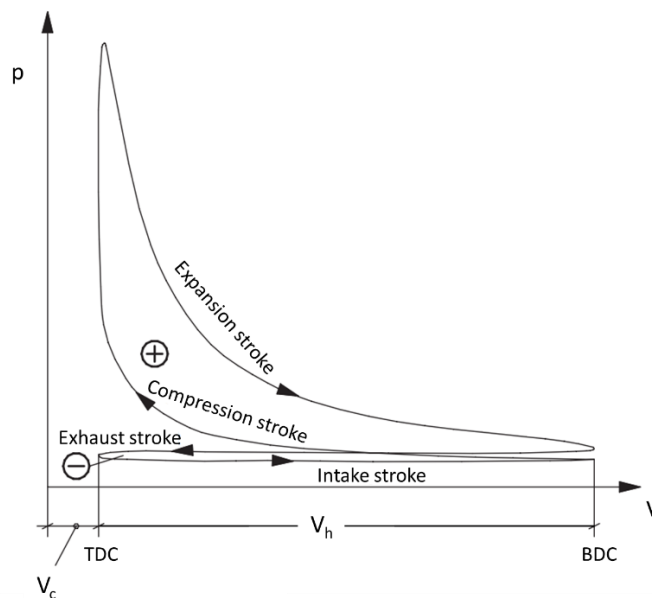


Figure 2. p - V diagram of the four-stroke combustion cycle (adapted from [6]).

2.2 Fuel injection

In modern engines, fuel injection is achieved through two primary methods: PFI and DI. The air/fuel ratio, denoted as λ , can be expressed as:

$$\lambda = \frac{m_{air}}{m_{air,stoich}} = \frac{1}{\phi}. \quad (3)$$

Here, m_a represents the actual air mass present in the combustion chamber, and $m_{a,stoich}$ corresponds to the stoichiometric air mass. The reciprocal of λ is the fuel/air ratio, denoted as ϕ . The stoichiometric air mass depends on the type of fuel and specifies the precise quantity of air required to completely oxidize the fuel. When the actual air mass equals the stoichiometric air mass, $\lambda = 1$. Lean mixtures contain excess air, resulting in $\lambda > 1$, while rich mixtures lack sufficient oxygen for complete fuel oxidation, leading to $\lambda < 1$. To ignite a mixture, the fuel-air ratio must be within the ignition limits. The flammability limits are, for example, for gasoline $0.4 < \lambda < 1.4$ [7] and for H_2 $0.13 < \lambda < 10$ [7]. A deviation from this range towards leaner mixtures can lead to unstable combustion and a higher risk of misfiring, while deviations towards richer mixtures lead to increased soot formation.

In the case of PFI, the injector is positioned upstream within the intake providing a homogeneous air/fuel mixture. In contrast, DI involves mounting the injector in the cylinder head, enabling the direct injection of fuel into the combustion chamber. This approach enhances operational flexibility because it allows adjusting the timing of injection. Achieving a nearly homogeneous mixture is feasible by injecting fuel early during the intake stroke, allowing sufficient time for thorough mixing before ignition. Injecting fuel later during the compression stroke results in a stratified and inhomogeneous mixture. However, the distribution of fuel at the moment of ignition is essential, as the air-fuel ratio must fall within the range of the flammability limit in the vicinity of the spark plug to ensure an ignition of the mixture. Creating an ignitable mixture around the spark plug at ignition timing becomes progressively challenging with later injections. However, DI offers the possibility of increasing efficiency in the partial load by means of charge dilution through lean operation. In particular, stratified lean combustion remains the most effective single measure for reducing consumption at part load. of the more energy-efficient combustion process [2–5].

2.3 Cyclic variations in SI engines

The term CCV refers to the variations of easily measurable variables like the maximum in-cylinder pressure or the IMEP from cycle to cycle. Ideally, each engine cycle should be nearly identical in terms of pressure and temperature rise to ensure smooth and efficient engine operation. However, due to various factors, such as variations in charge movement and air-fuel mixture distribution, there occur variations in the performance of individual engine cycles. Engine manufacturers commonly employ the term CCV to primarily denote variations in IMEP. Correspondingly, the coefficient of variation (COV) in IMEP has been established as a metric for assessing CCV and is expressed in percent:

$$COV = \frac{\sigma_{IMEP}}{\overline{IMEP}} \cdot 100. \quad (4)$$

It is the standard deviation in IMEP σ_{IMEP} divided by the mean IMEP (\overline{IMEP}). The engines drivability is negatively affected when COV exceeds about 10%. Typical values are in the range of 3% to 5% [5].

In extreme cases, CCV can lead to misfires or knocking combustion. For the conventional SI engine with a homogeneous fuel-air mixture, strategies exist to avoid such extreme cases and ensure stable engine operation. However, these strategies often come with a decrease in efficiency. With the development of downsizing engines, the unanswered question regarding the true causes of CCV persists, especially in highly optimized operating points that can adversely affect the combustion process. A detailed understanding of the causes of CCV could enable engine manufacturers to either counteract instabilities or carry out more targeted optimizations. In general, the challenge is to operate engines as close to the stability limit as possible to enable the optimum in terms of efficiency and pollutant emissions. However, phenomena that impair engine operation, such as knocking, incomplete combustion, or misfires, must be strictly avoided [5].

Figure 3 illustrates typical pressure traces for SI engines. Even though the COV of IMEP at this particular operating point is low ($COV_{IMEP} = 1\%$), there are significant differences among the pressure traces.

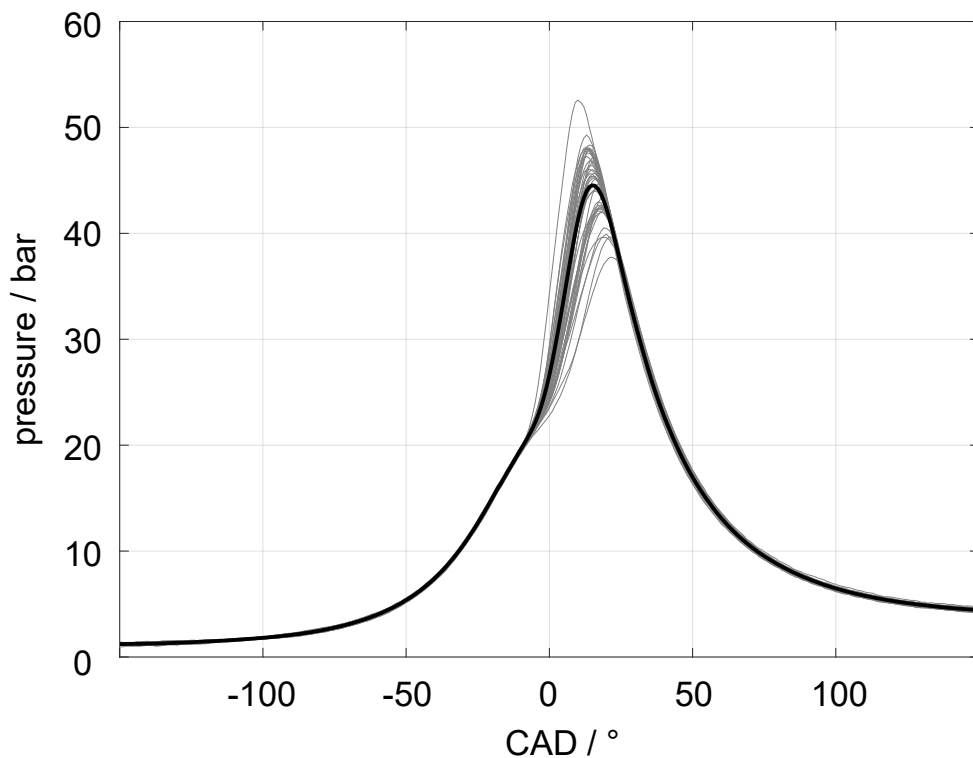
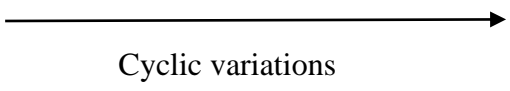


Figure 3. Measured in-cylinder pressure of single cycles (grey) and their mean (black) vs. crank angle degree. The single-cylinder SI engine was operated with port fuel injection at 1500 rpm, $\phi = 0.8$ and ignition timing 20°CA before TDC.

Some important causes of CCV and their possible effects are shown in Table 1. In this context, a macroscopic chain of effects is understood to be the connection of primarily causes, external causes, intrinsic causes, and the effects on CCV. Examples of important possible causes include variations in intake flow, injection, mixture formation, and ignition. The interactions of these individual components are decisive for the overall process. For instance, the intake flow determines the tumble intensity as well as the turbulence degree in the cylinder, and turbulence influences almost all subsequent processes. Such interactions are important and are not shown here for the sake of clarity. The actual causes of CCV and the importance of individual phenomena still depend on the engine geometry and operating point. However, the effects cannot be fully predicted at present because the understanding of the relationships between cause and effect is insufficient. The governing physical-chemical processes occur on different time and length scales, resulting in a multi-scale causal chain, the understanding and analysis of which constitute the central challenge in the study of CCV [5].

Table 1. Possible causes and effects of CCV in SI engines.

Primary cause	External cause	Intrinsic cause	Effects on
Intake flow	Intake pressure variations	Periodic effects, instability of the intake valves, turbulence	→ Momentum, flow movement, cylinder charge, residual gas
Injection / mixture formation	Variations of pressure ratio p_{inj}/p_{cyl}	Turbulent jet, cavitation, jet-flow interactions	→ Fuel mass, mixture distribution
Spark ignition	Spark energy, spark location, conditions near spark	Variations in the plasma	→ Ignition behavior, misfires, combustion duration
Σ External impacts	Integral effect  Cyclic variations		Maximum pressure, knocking, thermal efficiency, pollutant emissions

2.3.1 Recent work on CCV

CCV in DISI engines are typically determined by the early combustion phase [8,9] and the interaction of fuel injection, flow, and ignition has been identified as a significant part of a causal chain leading to CCV [10,11]. The unsteady fuel injection plays a determinative role, influencing the structure of the injection sprays and, consequently, the evolution of subsequent

processes. The complexity of the interconnected mechanisms and their effects on the resulting spray breakup and the link between evaporation – mixture formation – ignition has been barely investigated so far [12–14].

The complex three-dimensional motion of the flow in an engine is strategically induced during the intake stroke, facilitating the conservation of the bulk flow's kinetic energy throughout the compression stroke. As the piston approaches TDC, the formerly stable tumble flow undergoes a transition into an unstable state, leading to the conversion of its energy into smaller-scale turbulent eddies. These perturbations in flow dynamics bear the potential to trigger undesirable consequences, including partial combustion and complete misfires, with such impacts becoming especially prominent in SI engines with late DI. Several studies, conducted by Buschbeck et al. [15], Zeng et al. [16,17], Bode et al. [18,19] and Dreher et al. [20], have explored the connection between these tumble movements and the velocity of combustion reactions.

Buschbeck et al. [15] focused on investigating the in-cylinder flow patterns and their impact on combustion dynamics. Their research revealed that under stoichiometric conditions, the primary factor contributing to CCV is variations in kinetic energy. In contrast, when operating with lean mixtures, the predominant driver of CCV becomes the movement of the flame, influenced by the large-scale flow structures.

Zeng et al. [16] shed light on the fact that even in a seemingly stable and homogenous operating scenario with a COV as low as 0.9%, the influence of large-scale flow on flame behavior persists from the initial flame kernel to the conclusion of the combustion process. In a separate investigation [17], they employed a DISI engine with an inhomogeneous mixture and demonstrated that, in this context, the interplay between the flow and the spray is pivotal for achieving rapid early ignition.

Bode et al. identified a specific region within the flow field before ignition that exhibits a strong correlation with IMEP. Subsequently [19], they probed the interaction between the flow patterns and the spark plug. Figure 4, extracted from [19], illustrates the relationship between the spark plug's location and the velocity magnitude of the flow field. As anticipated, the flow surrounding the spark plug, particularly within the central plane, exerts the most significant influence on the actual spark location. A high velocity in flow region F1 and a low velocity in F2 result in the spark occurring closer to the $x = 0$ axis, as depicted in the scatter plot in Figure 4. Furthermore, they established a positive correlation between the spark's position and the crank angle at which 5% of the mass fraction is burned (CA05). Specifically, a flow pattern forces the spark to remain in close proximity to the spark plug resulted in faster engine cycles.

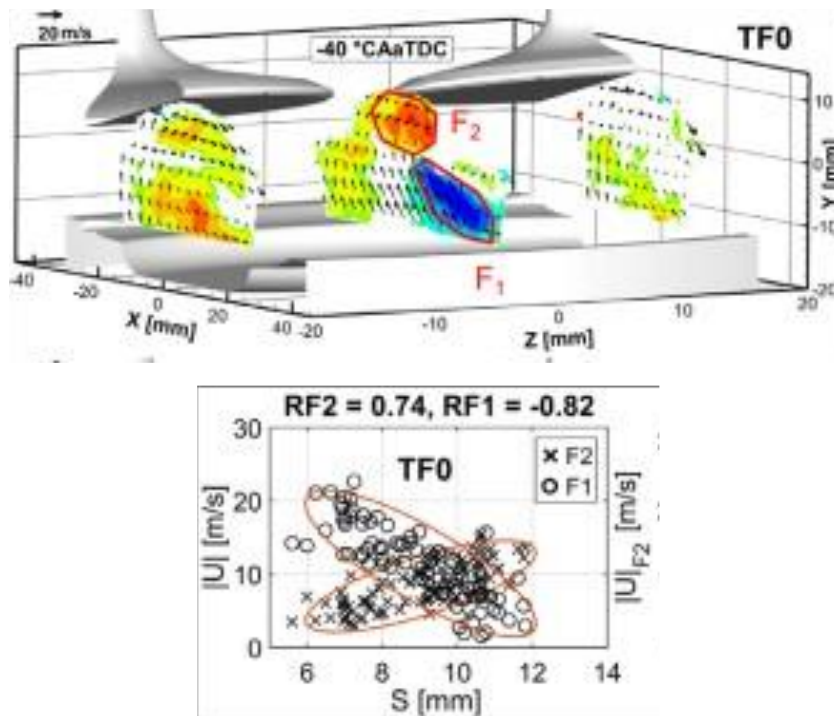


Figure 4. (Top) two-dimensional correlation between the x -position of the spark and the velocity magnitude of the flow field before ignition and (bottom) scatter plot of the spatial averaged velocity magnitude of the marked areas and the spark position. Adapted from [19].

Between injection and the ignitable mixture, processes such as spray breakup, evaporation, and mixture formation occur. These processes and their interaction with turbulence are scarcely explored in DI engines concerning resulting CCV. In real engines with DI, a strong inhomogeneity of the mixture is observed, both as large-scale stratification in the case of late injection and as small-scale mixture fluctuation with injection during the intake stroke. This inhomogeneity significantly affects ignition, flame propagation speed, pollutant formation, and knocking tendency [21]. The effects of these inhomogeneities in the fuel field have been rarely investigated so far and considered only in a few simulation studies [22,23] for the available experiments [24,25].

The optimum combustion efficiency in an engine is achieved by creating a stratified mixture. To prevent issues like incomplete combustion or misfires, it is important to maintain a fuel-air mixture within the ignitable range near the spark plug. Early research efforts using optical diagnostics were primarily centered around examining the fuel/air ratio in the vicinity of the spark plug [26–30]. Despite variations in the equivalence ratio within a wide range that could potentially prevent ignition, no significant correlation was found between fuel concentration and combustion stability [26,29].

For instance, Gandhi and Bracco [26] conducted a study on combustion behavior in a two-stroke engine. They observed that, in a substantial number of cycles, the measured equivalence ratio fell well below the ignitable limit, yet these cycles ignited and burned effectively. This phenomenon was attributed to the movement of the mixture during the spark event. Back then, measurements of local equivalence ratios were rare, and the spark was considered a nearly

instantaneous energy source. As technology advanced, subsequent studies revealed a strong interaction between DI and spark ignition, resulting in shorter spark durations and greater spark stretch [31,32]. Consequently, the focus shifted from the mixture distribution itself to the interaction between the mixture and the spark. This required higher temporal and spatial resolution for analysis.

Peterson et al. [33] investigated rare partial burn cycles and misfires in an optical DISI engine. Figure 5 presents an excerpt of their research findings. They condensed information about the velocity field, equivalence ratio, and flame development for well-burned cycles, partially burned cycles, and misfired cycles into image sequences after spark ignition (occurring 30°CA before TDC). Through a visual analysis of the flame and examination of electric spark discharge parameters, they determined that a flame kernel consistently formed, even in misfired cycles. However, as the crank angle progressed, the flame failed to expand as rapidly as it did in well-burned cycles or extinguished entirely, ultimately resulting in a misfire. The precision and the spatial-temporal resolution of the fuel concentration measurements were limited by the low single-shot energy of the high-repetition-rate laser used. In particular, the recordings were therefore confined to a small field of view near the spark plug. Nevertheless, this work is outstanding in terms of both methodology and results.

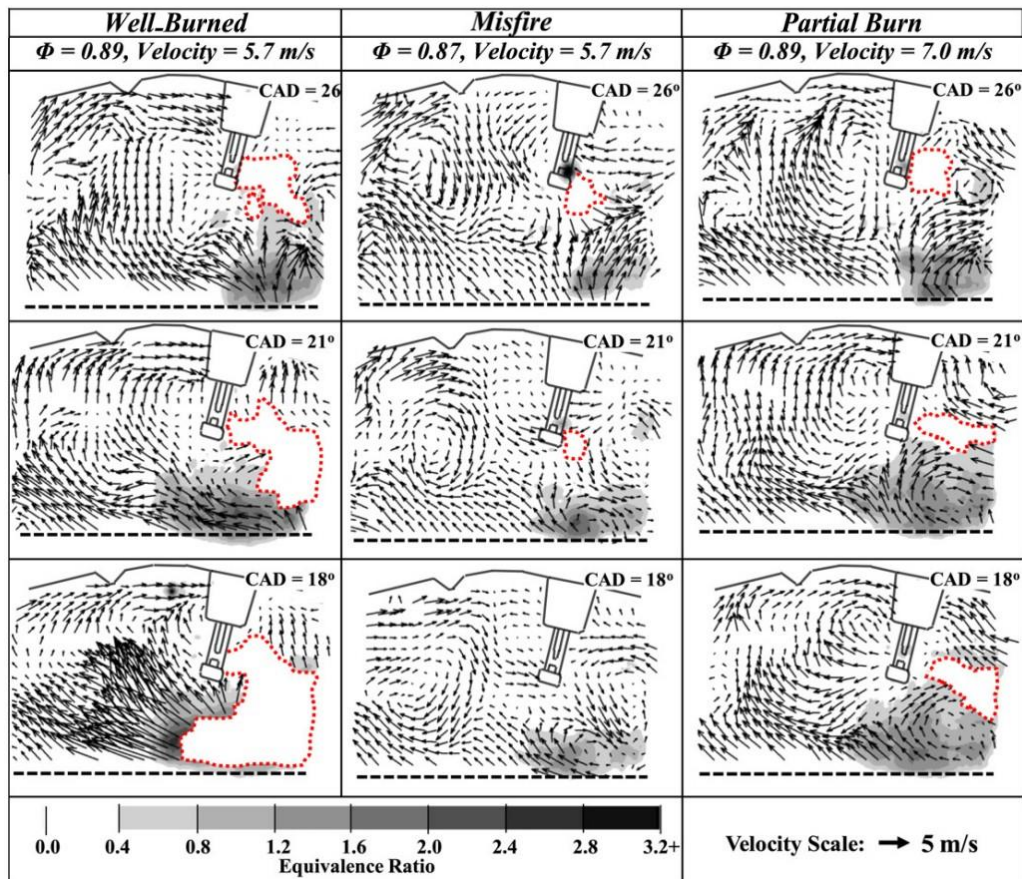


Figure 5. Time-resolved images of the velocity field, equivalence ratio and the flame kernel obtained from a two-dimensional plane for a (first column) well-burned, (second column) misfired and (third column) partially burned cycle. Adapted from [33].

The focus of this work was exclusively on the spray-guided combustion processes, in which injection and ignition are close together in terms of space and time. This combustion process has great potential for improving efficiency, but on the other hand is subject to extreme variability, including cycles where no combustion takes place. However, it is also of great practical and fundamental interest to understand how the inhomogeneity of the mixture affects the CCV even in less extreme cases.

When it comes to engine simulation, the Reynolds average Navier-Stokes (RANS) technique is often used [34,35]. However, RANS only yields mean phase-averaged quantities and, therefore, cannot be utilized for the analysis of CCV. Large-eddy simulation (LES), to the contrary, has the potential to address various phenomena by directly resolving large-scale structures and modeling small-scale structures of instantaneous flows. Consequently, LES has often been used to model turbulent and reactive flows in spark ignition engines [36,37].

Fontanesi et al. [38] investigated different orientations and positions of the spark electrode, as well as the impact of the flow field around the spark plug, and their impact on CCV. The simulation was done in gasoline DI engine under high speed, fully loaded conditions. As a result, they demonstrated that the orientation of the spark electrode has only a minor impact on CCV, while the velocity of the flow and the fuel distribution around the spark plug were identified as significantly influential factors.

Truffin et al. [39] investigated the source of CCV in a propane-fueled SI engine under stable and unstable operating conditions. The comparison between the fast and slow cycles revealed that variations in early flame kernel growth are attributed to the local velocity fields around the spark plug. Consequently, the velocity field around the spark plug influences the overall flame propagation.

Wadekar et al. [40] performed simulations for 12 engine cycles and compared the results with experimental data. They investigated the correlation between the time at which 10% of the fuel mass is burned (CA10) and the early growth of the early flame kernel growth and analyzed the results of flame propagation at two cross-sections (in the swirl and tumble plane) in the combustion chamber. The analysis of the fast and slow cycles showed differences in the instantaneous flame structures and propagation characteristics. The results indicate that the instantaneous velocity and the variations of the flows near the spark influence the growth of the early flame core and contribute to the variability of the combustion cycles.

2.4 Optical diagnostics for internal combustion engines

Optical diagnostics have become essential tools in characterizing physical quantities, visualizing the complicated processes within the engine. In the following some of the fundamental principles are outlined.

2.4.1 Diagnostic techniques in optical engines

With sufficient optical access, it is possible to determine a wide range of physical properties, such as fluid velocity, fuel concentration, gas temperature, flame evolution, soot concentration,

and more. Table 2 provides a summary of the most commonly employed diagnostic techniques for studying CCV.

Table 2. Commonly used diagnostic techniques applied in optical engines.

Physical property measured	Diagnostic technique	Principle	References
Fluid velocity	Particle image velocimetry	Small particles are seeded to the fluid and with a known time interval an image pair is taken. The particle shift yields flow velocity.	[19,32,41,42]
	Particle tracking velocimetry (PTV)	Similar to PIV, but with lower particle density. To calculate the fluid velocity each particle is tracked individual.	[43–45]
	Optical flow	Correlating the brightness pattern between two frames yields fluid velocity	[46–48]
Mixture distribution	Laser-induced fluorescence	A molecule absorbs the energy of a laser-photon and enters an excited state. By spontaneous transition into a lower energy state fluorescence is emitted at a wavelength longer than the excitation wavelength.	[32,49–52]
	Raman scattering	Non-elastic scattering of molecules. The scattered light is subject to a frequency shift in two directions (red- and blue-shifted). By spectral integration the concentration of a species can be measured.	[53]
	Raleigh scattering	Elastic scattering of molecules with diameters much smaller than the wavelength of the incident light. The signal represents the concentration.	[54,55]
Flame front	Chemiluminescence	Combustion is a natural light source. The emitted light is either directly from the reaction energy or indirectly by producing electronically excited species that emit spontaneously while returning into the ground state.	[56,57]
	OH-LIF	Combustion intermediate species are excited by a laser and the fluorescence can be used to measure the flame front.	[56–59]

In this work, PIV is employed to assess the in-cylinder flow field, LIF to measure the equivalence ratio, and chemiluminescence imaging to analyze the flame propagation. Detailed descriptions of these diagnostic techniques are provided in the subsequent subsections.

2.4.2 Particle Image Velocimetry

PIV is a non-intrusive optical measurement technique used in fluid mechanics and engineering to visualize and quantify the velocity field of a fluid flow. A typical experiment is shown in Figure 6.

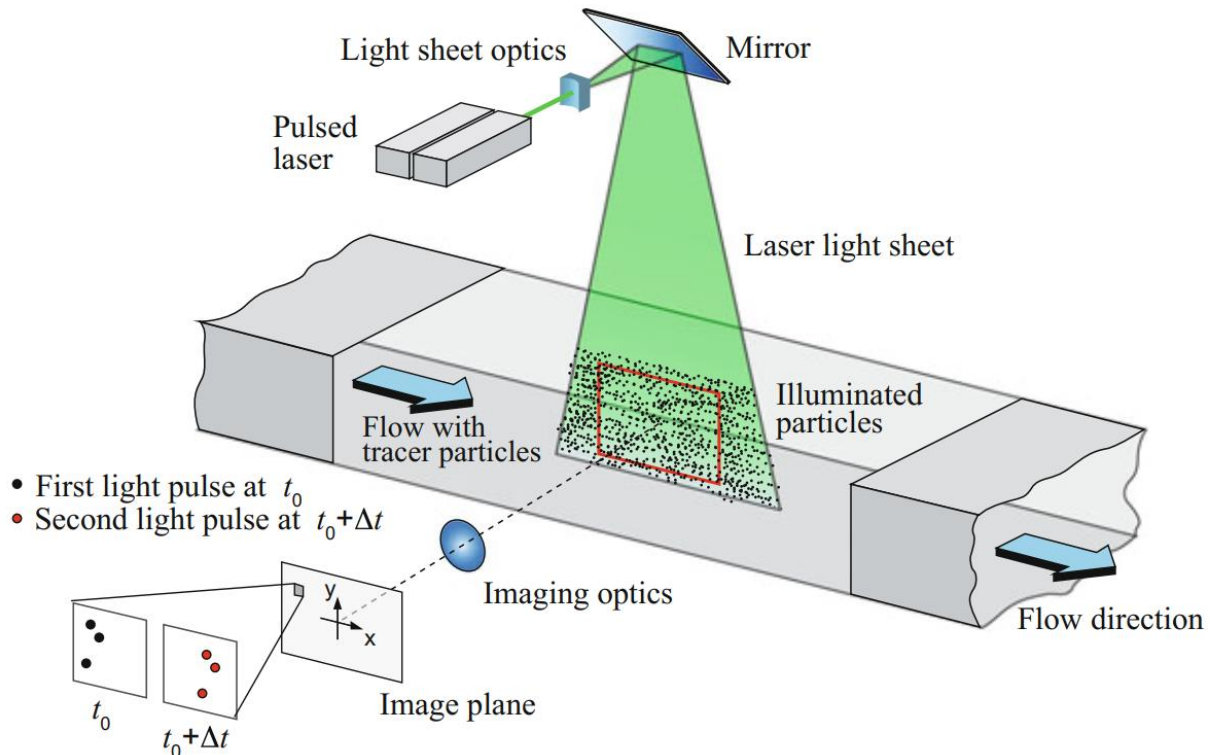


Figure 6. Basic experimental arrangement for a planar PIV measurement [60].

First, tracer particles are introduced into the fluid of interest. These particles serve as markers that follow the fluid's motion. Ideally, the particles should match the density of the fluid as closely as possible. If the particles have a significantly different density from the fluid, they should be sufficiently small in order to follow the fluids motion. In an air flow usually particles with a diameter of approximately $1 \mu\text{m}$ are used [60].

To illuminate a narrow cross-sectional slice within the fluid a laser sheet is created. When the laser sheet interacts with the tracer particles, it causes them to scatter the incident laser light. The high-speed camera is synchronized with the laser system and captures the scattered light of the particles in two images with a known time delay Δt .

To extract velocity information and determine the fluid's velocity field, these images are subsequently analyzed using specialized software (e.g., DaVis from LaVision). In the image analysis step, the PIV software conducts correlation analysis on the image pairs. This involves

dividing the images into smaller regions known as "interrogation windows". Within each interrogation window, the software tracks the movement of the tracer particles between the two frames. This tracking enables the calculation of displacement vectors for the particles. Finally, to obtain velocity information, each displacement vector is divided by the known time interval Δt between the two laser pulses. This yields a velocity vector for each interrogation window. These velocity vectors collectively form a velocity field that represents the flow within the illuminated plane [60].

PIV measurements are subject to a variety of challenges that can introduce errors at different stages of the measurement process. These errors are a composite of several factors, starting from the setup and recording phase and extending to the methods of evaluation. To obtain accurate results in PIV, it is essential to recognize and mitigate these sources of error.

First, issues related to installation and alignment are critical to address. When the light sheet plane is not precisely aligned with the intended flow direction, it captures the projection of the velocity vector within the measurement plane rather than the actual flow components of interest. Additionally, if a significant flow component runs perpendicular to the light sheet, substantial perspective errors may emerge, and these errors become more pronounced as the distance from the optical axes of the lens increases. To minimize these errors, one can reduce the observation angle, which can be achieved by increasing the working distance, selecting a lens with a longer focal length, or cropping PIV images. For comprehensive error reduction, stereoscopic recording approaches are often necessary [60].

Another source of error arises during the calibration process. If the measurement plane does not precisely coincide with the plane selected for calibration, errors can occur. Errors can also arise if the calibration target is inaccurately manufactured, leading to a wrong scaling factor for pixel-to-meter conversion [60].

In addition to installation and calibration issues, errors can be introduced by various system components. Optical elements situated between the particles and the sensor, such as glass windows, filters, or beam splitter cubes, can introduce optical aberrations, affecting the accuracy of peak detection if particle images deviate from Gaussian characteristics. Image distortions can also occur due to imaging optics when dealing with large fields of view and short observation distances, under non-Gaussian imaging conditions [60].

Furthermore, errors related to the flow itself must be considered. Large flow gradients and strong velocity fluctuations in turbulent flows can introduce errors due to particle slip. Density gradients caused by shocks or intense vibrations in the flow can also result in measurement errors [60].

2.4.3 *Tracer laser-induced fluorescence*

Tracer LIF is a specialized technique to study and analyze the behavior of fluids or gases within a medium. A tracer is necessary to help visualize and quantify the characteristics of the medium being studied. By introducing a known concentration of tracer into, e.g., fuel, the concentration

and distribution of the fuel can be measured based on the intensity of the emitted fluorescence. This allows for quantitative measurements of parameters such as concentration gradients and mixing rates [61].

Tracer LIF relies on the interaction between incident laser light and a sample, which can be a gas or liquid, leading to the emission of fluorescence radiation. The electronic states of a typical organic molecules can be categorized into singlet states and triplet states as illustrated in Figure 7. When these molecules are exposed to light of the appropriate wavelength, they are excited, often residing in vibrational levels of an excited singlet state. The probability of occupying a specific excited singlet state, S_n , is influenced by transition probabilities and the excitation wavelength.

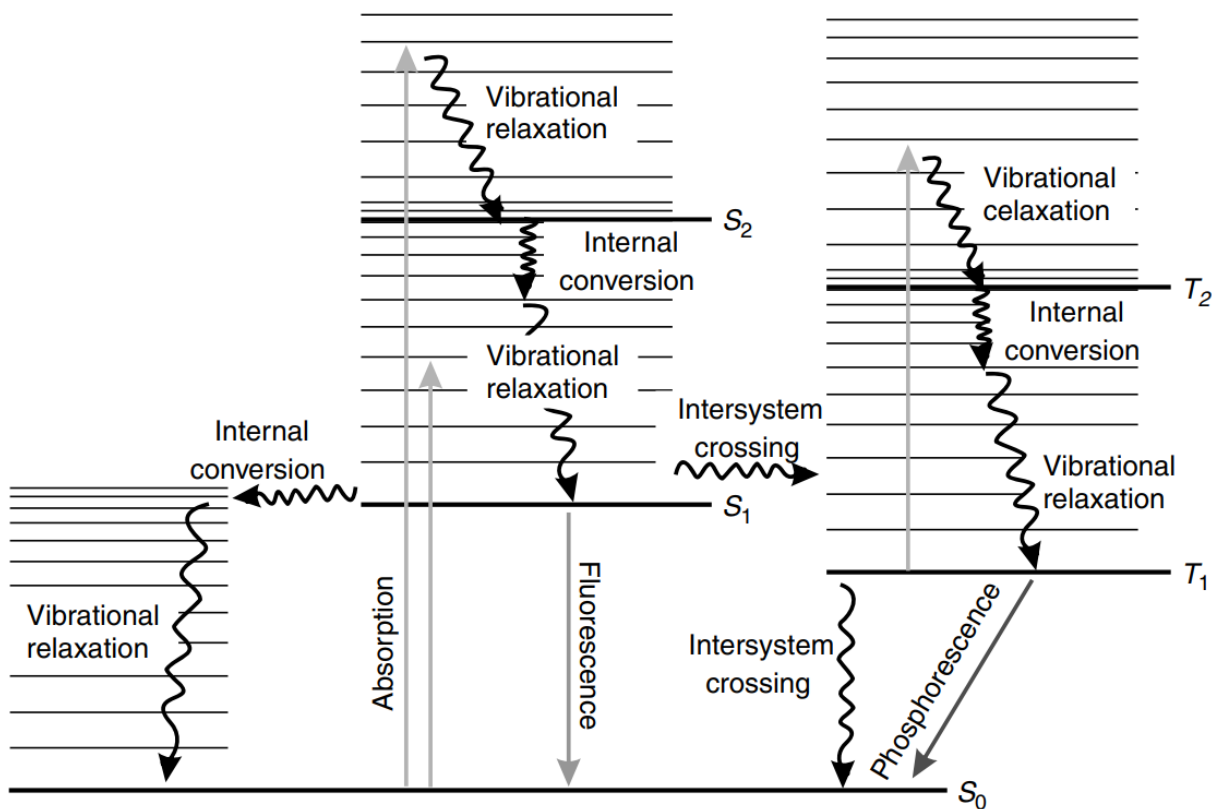


Figure 7. Jablonski diagram illustrating the electronic energy levels found in typical organic molecules, along with potential interchanges between various singlet and triplet states [61].

The higher energy states are unstable and will eventually revert to their lower-energy ground state. This deexcitation can occur through several mechanisms:

Vibrational relaxation is a non-radiative process in which the molecule loses energy through collisions with other molecules. This process brings the molecule to a lower vibrational level within the same electronic state, preparing it for subsequent radiative transitions or other non-radiative processes. With elevated temperatures, vibrational relaxation is intensified. This means that at higher temperatures, there is a greater propensity for excited molecules to lose energy through collisions with other molecules and transition to lower vibrational levels within the excited state. This process affects the subsequent fluorescence emission [61].

Fluorescence emission is a radiative transition and the primary deexcitation process in LIF. After excitation, the molecule or atom relaxes to a lower vibrational level through vibrational relaxation. From this state, it can return to the ground state (S_0) by emitting a fluorescence photon. This occurs with the emission of a photon, producing the fluorescence signal. Temperature can influence the shape and characteristics of the fluorescence spectrum. As temperature rises, the distribution of vibrational levels within an excited electronic state change, affecting the relative intensities of spectral peaks. This can result in shifts in the fluorescence spectrum, changes in peak intensities, and broadening of spectral lines [61].

Another non-radiative process is *internal conversion*. Here, the molecule undergoes a transition from a higher electronic state (e.g., S_1) to a lower electronic state (e.g., S_0) within the same spin multiplicity. This process typically occurs very rapidly, on the order of femtoseconds to picoseconds. It competes with fluorescence emission and reduce the overall fluorescence intensity [61].

A different process to relax to the ground state is *intersystem crossing*. It is a non-radiative transition in which the molecule undergoes a change in spin multiplicity, usually from a singlet state (e.g., S_1) to a triplet state (e.g., T_1). Triplet states have longer lifetimes and can be involved in phosphorescence or other photophysical processes. In some cases, after intersystem crossing to a triplet state, molecules can undergo radiative deexcitation by emitting a *phosphorescence* photon when returning to a singlet state. Phosphorescence is relatively slow compared to fluorescence and can mostly be observed at lower temperatures [61].

In many applications the main competing deexcitation mechanism to fluorescence is *collisional quenching*. Molecules in the excited state can lose their energy through collisions with other molecules. Especially at higher temperatures, molecules have greater thermal energy and move more rapidly, leading to a higher collision frequency. As a result, collisional quenching becomes more prominent as the temperature increases. A detailed description of this photophysical mechanism can be found in [61–63].

Conducting tracer LIF measurements within an engine environment presents several challenges. Firstly, the choice of a suitable tracer is critical, with preference given to tracers exhibiting a high quantum yield. Acetone, toluene, and anisole are common choices, though the selection hinges on the specific engine and its operational conditions. The total fluorescence of the chosen tracer decreases as the temperature rises or increases as the pressure rises. This variance can introduce complexities in obtaining precise measurements. Furthermore, the fluorescence quantum yield exhibits a strong temperature dependence, which can fluctuate significantly within the temperature range encountered during the engine's compression stroke. These factors further complicate the accuracy of tracer LIF measurements [64].

Fuel/air ratio LIF

Reboux et al. [51] presented a way of using fluorescence for direct quantitative measurements of the fuel/air ratio in engines. Fuel/air ratio LIF (FARLIF) is a non-intrusive method that takes

advantage of the quenching phenomenon of LIF, though it can only be used under specific assumptions [51].

The detected intensity of the LIF signal at a given wavelength can be expressed by

$$I = I_L \Phi_{fl}(p, T, n_i) n_{tr}(p, T) V \sigma_{abs}(T) \eta \Pi, \quad (5)$$

where I_L is the incident laser light intensity, Φ_{fl} is the fluorescence quantum yield, n_{tr} is the tracer number density, V is the probe volume, σ_{abs} is the absorption cross section and η as well as Π are the detection and collection efficiencies of the detection system, respectively. The tracer number density n_{tr} is proportional to the fuel number density and is often the desired quantity. However, the signal is not only influenced by the tracer itself, but also by the pressure p , temperature T , number density of the bath gas composition n_i . While the pressure can easily be measured in an engine, the temperature and bath gas composition are unknown [51]. Temperature-dependent variables can either be corrected by separate temperature measurements or must be taken into account in some other way, e.g. by reference measurements at (globally) the same temperatures.

FARLIF takes advantage of the deexcitation process collisional quenching. For most aromatic tracers the important bath gas species is oxygen. Oxygen quenching significantly reduces the LIF signal, as considered in the fluorescence quantum yield Φ_{fl}

$$\Phi_{fl} = \frac{k_{fl}}{k_{tot} + \tilde{k}_q^{O_2} n_{oxy}}, \quad (6)$$

where k_{fl} is the rate of spontaneous fluorescence, $\tilde{k}_q^{O_2}$ is the bimolecular quenching rate coefficient of oxygen, n_{oxy} is the oxygen number density and k_{tot} summarizes the rates of all other deexcitation mechanisms. As long as the rate of oxygen quenching dominates the deexcitation mechanisms ($k_q \gg k_{tot}$), k_{tot} can be neglected. The LIF signal then becomes proportional to the fuel/air ratio ϕ :

$$I \sim \frac{n_{tr}}{n_{oxy}} = \phi. \quad (7)$$

Koban et al. [65] investigated the FARLIF approach with toluene as a tracer and revealed some limits of this approach. In order to determine the FAR directly from the LIF measurements not only elevated pressures (> 2 bar) are necessary, but also little or no residuals. Only then it is possible to quantify the FAR for a wide range ($0 > \phi > 6$) (see Fig. 2a in [65]).

2.4.4 Chemiluminescence

Chemiluminescence occurs when a flame emits visible light as a result of chemical reactions taking place within it. The light stems from excited states of atoms and molecules. The colors of the flames and the specific wavelengths of light emitted depend on the atoms or molecules involved in the combustion process. This phenomenon can be imaged by high-speed cameras, enabling a relatively simple and cheap analysis of the flame propagation compared to laser-based diagnostics [66]. Each species emits light with a characteristic wavelength or wavelength band. The primary source of emissions includes OH^* , CH^* , C_2^* , CO_2^* and to lesser extent

HCO*, CO*, and CH₂O*. Figure 8 shows the chemiluminescence spectrum between 270-540 nm.

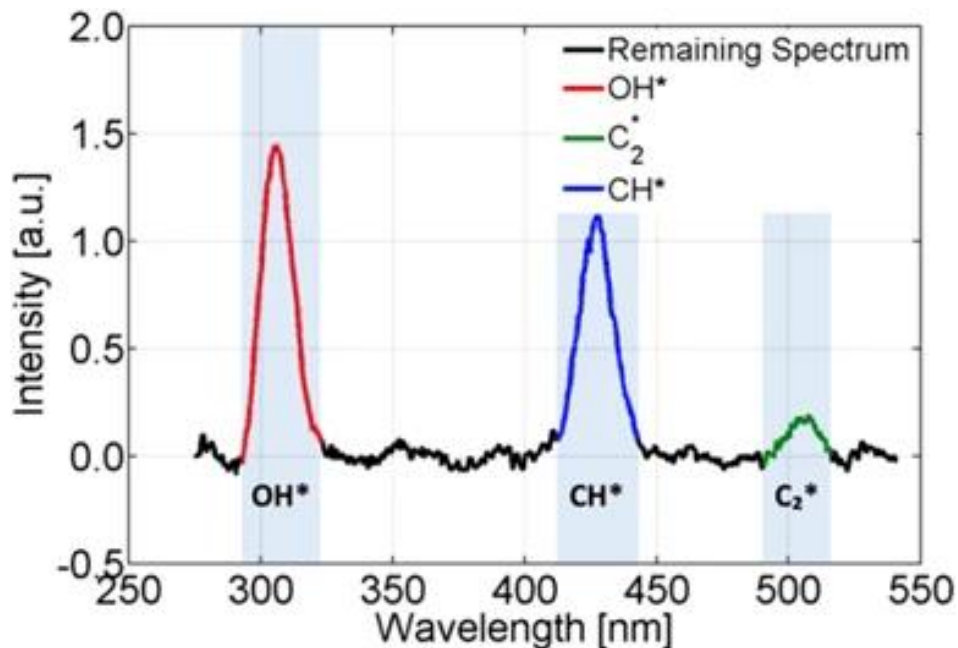


Figure 8. Typical spectrum after subtraction of broadband chemiluminescence and thermal radiation [67].

Non-sooting flames often appear in blue, since most of the species (OH* and CH*) emit blue or even UV light. Sooting flames, on the other hand, appear yellow or orange due to the incandescence of hot soot. A typical flame marker is OH* since it is present in the high-temperature reaction zone of the flame. It emits light with a wavelength band of 306-315 nm and is often used to visualize the flame [57,68].

2.5 Optically accessible engine

Optical engines share similar geometric dimensions and in-cylinder flow patterns with traditional metal engines. However, there are two key distinctions in optical engines: First, the upper optical section of the piston can operate without the need for lubricants, ensuring a cleaner combustion chamber during operation. Secondly, it provides optical access from below through a transparent piston window, through a window in the cylinder, or a combination of both. Figure 9 provides a schematic representation of an optical engine featuring a Bowditch piston, while a comprehensive overview of the development of optical engines can be found in reference [69].

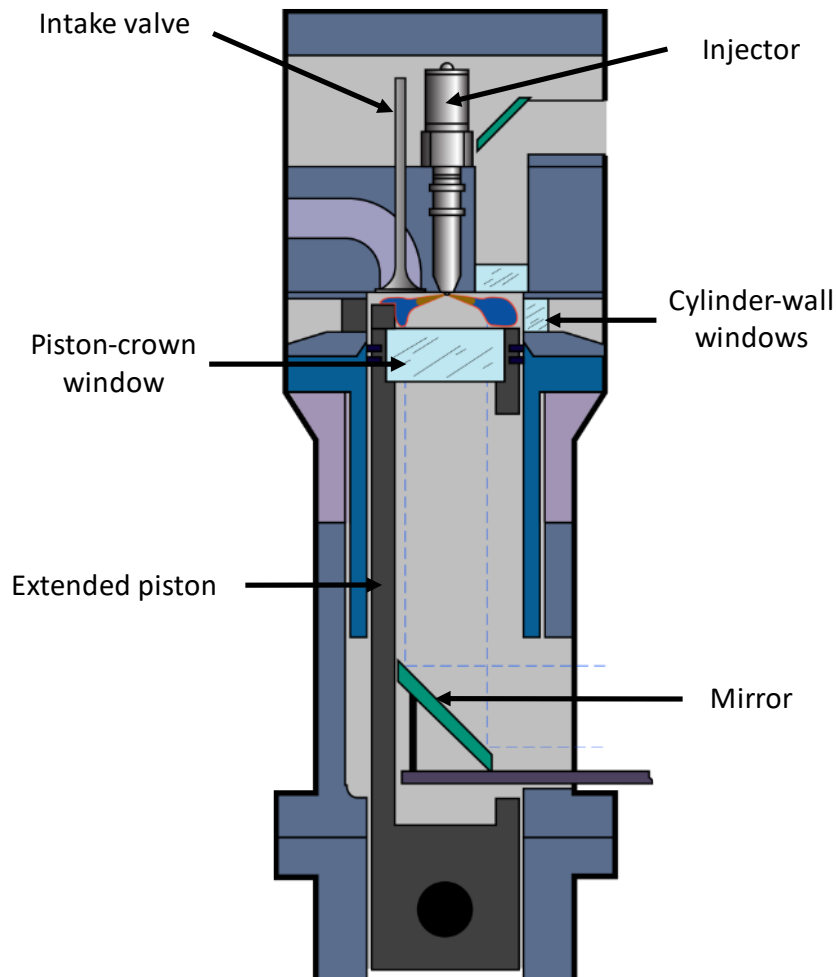


Figure 9. Schematic of an optically accessible DI research engine.

In order to facilitate optical access from the side, the combustion chamber wall in optical engines is partially constructed using materials such as fused silica or sapphire. Fused silica exhibits lower thermal conductivity compared to metal, leading to elevated temperatures on the inner surface and consequent differences in heat transfer. To mitigate the thermal stress experienced by optical engines, a strategy known as "skip-firing" is employed. This approach involves firing one or a few combustion cycles followed by at least one motored cycle. However, even when operating in skip-fired mode, the maximum operating duration for optical engines remains significantly shorter than that of their metal counterparts. Furthermore, due to the skip-firing mode, the use of exhaust gas recirculation (EGR) systems and emission measurement devices is not feasible in optical engine test facilities as it would be with metal engines. The lubricant-free, "optical" segment of the Bowditch piston allows for nearly oil-free combustion but necessitates the use of piston rings made from polymers or Teflon-bronze. This results in increased blow-by, especially when the engine is cold, as compared to piston rings used in metal engines.

2.6 Light sources and detectors

In Table 2, it is apparent that the majority of optical diagnostics require an extra light source. The subsequent sections describe the light sources and detectors utilized in this research.

Laser

The term "laser" is an acronym representing "light amplification by stimulated emission of radiation," which refers to its fundamental operational principle. Unlike many other light sources, a laser beam is predominantly monochromatic, nearly collimated, and coherent in both phase and time [70]. In its most basic configuration, a laser comprises three fundamental components: an active medium, an excitation source, and a set of mirrors, as illustrated in Figure 10.

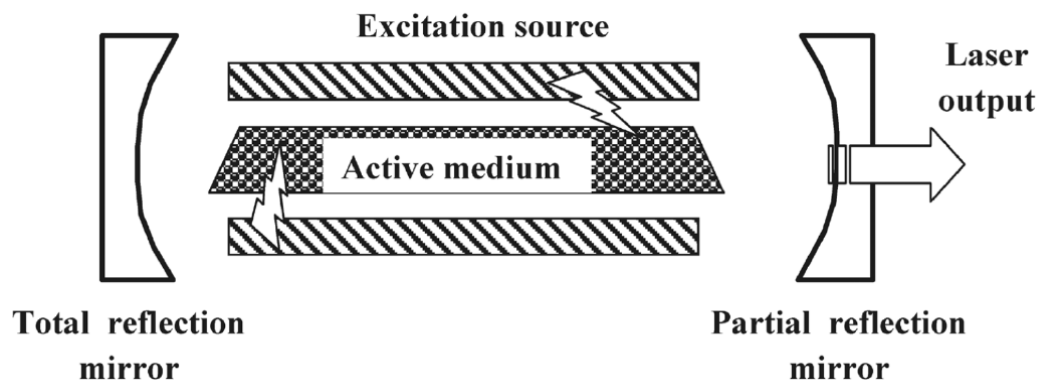


Figure 10. Schematic principle of a laser [70].

Typical excitation sources for lasers encompass options such as flash lamps, electrical circuits, or even other lasers. The active medium, exemplified by materials like neodymium-doped yttrium aluminum garnet (Nd:YAG) or neodymium-doped yttrium orthovanadate (Nd:YVO₄), absorbs photon energy, causing its electrons to transition from the ground state to an excited state. With sufficient duration in the excited state, a population inversion between the ground and excited states occurs. Population inversion means that more electrons are in a higher-energy state than in a lower-energy state.

At some point, one electron will transition to a lower energy state, releasing a photon in the process. When this emitted photon's energy precisely matches the energy difference between the current state and a lower-energy level, it can stimulate another excited electron. This electron, in turn, will transition to a lower-energy state, emitting another photon identical in energy, wavelength, direction, polarization, and phase as the incident photon. This unique property, known as coherence, essentially makes the newly generated photon a copy of the original photon. This type of emission, where a photon is not emitted spontaneously but is triggered by another photon, is called stimulated emission [71].

In the laser cavity, the active medium is surrounded by two mirrors: one for total reflection and the other for partial reflection. These mirrors serve to amplify the total number of photons

within the cavity. Certain laser diagnostics, such as LIF, necessitate short yet intense laser pulses. To achieve this, opto-electronic quality switches, known as Q-switches, are incorporated within the laser cavity. The Q-switch temporarily blocks the partial reflection mirror until the maximum population inversion is reached. Upon activation, the Q-switch permits a brief laser pulse, approximately 10 nanoseconds in duration, characterized by high power, to exit the cavity [72]. Typically, Nd:YAG lasers operate at repetition rates of around 10 Hz. However, there are lasers with significantly higher repetition rates, reaching into the kHz range. These high-repetition-rate lasers tend to have lower pulse energy [70].

Intensified CCD camera

Intensified relay optics (IRO), also known as image intensifiers, amplify incoming light and the basic working principle is shown in Figure 11.

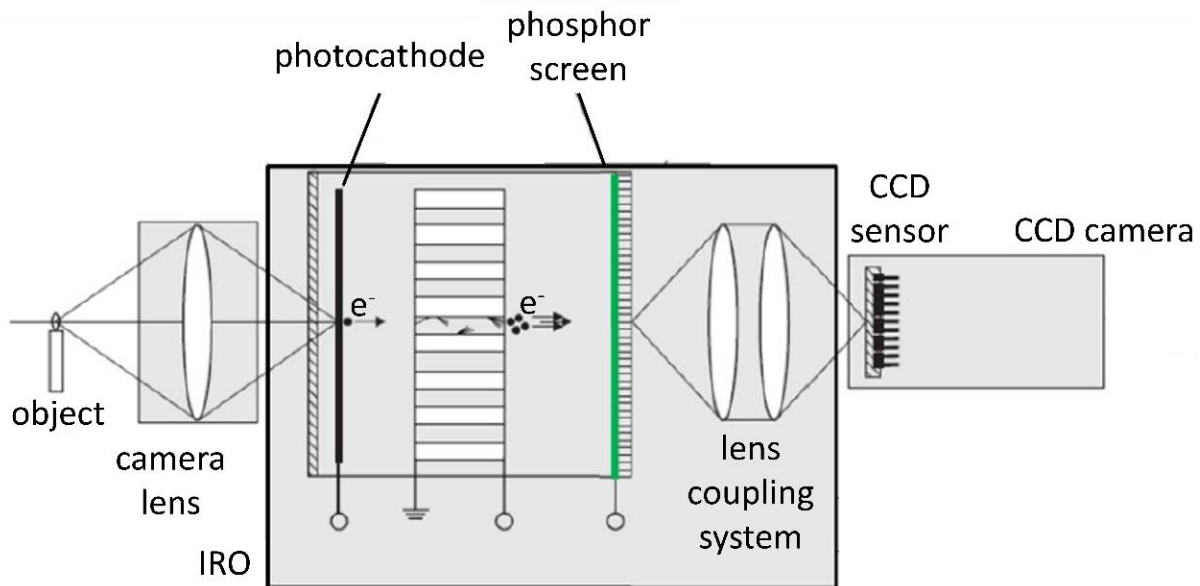


Figure 11. Common arrangement of a camera lens, image sensor, and camera. Adapted from [73].

Light from the object enters the camera through a lens and strikes a photocathode. The photocathode converts incoming photons into electrons through a process called photoemission. The emitted electrons are accelerated towards a microchannel plate (MCP), which is essentially an array of tiny channels with a phosphor coating. These channels multiply the number of electrons as they pass through. The electrons hit a phosphor screen at the output of the MCP. This screen emits photons when struck by the electrons, creating a visible image that is intensified compared to the original scene. Intensified light from the phosphor screen is then transmitted through a series of lenses and mirrors, known as relay optics. These components focus and magnify the intensified image for capture by the charge-coupled device (CCD) sensor [73].

CCDs convert incoming photons into electrical charge. The CCD then reads out the electrical charges to create an image [70]. Since each pixel must be read out one after another, the frame

rate of CCD cameras is low compared to complementary metal-oxide semiconductor (CMOS) cameras, which are explained in more details in the next paragraph.

The quantum efficiency of CCD sensors depends on the bandgap of the semiconductor material and varies with different wavelengths. For capturing light in the visible spectrum (300-700 nm), silicon is commonly employed as the semiconductor material.

High-speed CMOS camera

High-speed CMOS cameras are a specific type of image sensor technology that have their read-out circuit within each pixel, allowing for a significantly faster read-out process than in CCDs. Additionally, the frame rate can be increased by selectively reading out smaller sub-windows instead of the entire sensor area. The high frame rate allows for the detailed analysis of ultra-fast events [60].

3 Effects of different injections strategies on CCV in an isooctane-fueled SI engine

This chapter starts with a further overview of the literature and introduces the methods to quantify the flow field, mixture distribution, and flame propagation in an optical engine fueled with liquid iso-octane. The influence of the measured parameters on each other and on combustion CCV are investigated. Most of the work has been published in Laichter et al. [74].

3.1 State of the art

The stability of the cycle is particularly affected by the early phase of combustion, which is strongly correlated with the initial growth of the flame kernel [8,75,76]. Previous experimental investigations have therefore focused on investigating the region near the spark plug during ignition and early flame propagation [8,9,77]. In the work of Aleiferis et al. [8] the early flame kernel was investigated a strong correlation between CA10 and the equivalent flame radius was identified. They also investigated the connection between flame growth and convection. They found that the flame grows faster when the convection velocity in the swirl and tumble planes is higher during the first crank angles after ignition, corresponding to 0.1-1% mass fraction burned. Another example of connecting the early flame with more global pressure-based metrics Hanushkin et al. [78], who applied machine learning methods to predict the cycles with high maximum in-cylinder peak pressure based on optical cross-sections of the flame shortly after ignition timing.

The rotating movement of the in-cylinder charge, the tumble flow, influences the early flame kernel growth and is known to be one origin of CCV [18,33], [5](p. 450-453). This tumble flow becomes unstable towards firing TDC, and the kinetic energy of large scales of the flow is transferred into small-scale turbulence. DI adds significant momentum to the flow, and if that injection is scheduled late, large velocity gradients may still be present at ignition. A key technique for gaining insight into the pre-ignition flow is high-speed PIV, which provides crank-angle resolved flow fields in a two-dimensional plane [32,41,79]. Measurements with high-speed PIV in an optically accessible DISI engine found the center position of large-scale tumble vortex varied substantially in the horizontal direction, while the vertical direction was mainly determined by the piston movement [41]. Another PIV study [15] with lean operation revealed that the variation of the kinetic energy has a relatively small influence on CCV compared to the dominant large-scale flow structures.

With late injection, significant mixture inhomogeneity (so-called “stratification”) can be expected at ignition timing. The spatial distribution of the fuel is usually assessed from laser-induced fluorescence imaging of a “tracer” added to the non-fluorescing surrogate fuel [80]. Combining LIF and PIV, Peterson et al. [33,77] conducted a multiparameter analysis simultaneously capturing the flow field, mixture field, and early flame development for stratified combustion, with a focus on one of the extremes of CCV – misfires. A key finding was as stated in chapter 2.3.1 that misfires did not result from failure to ignite, but from failure to enflame. The spark always developed into an early flame kernel, but for unfavorable

combinations of flow and fuel concentration fields it extinguished soon after and was not able to enflame the entire charge. While misfires are a particular problem in spray-guided operating strategies, where the injection is in close spatio-temporal proximity to the spark, they are much less of an issue when the injection is earlier, as it is more commonly implemented in commercial engines. Nevertheless, also in such less extreme cases it is of general practical and fundamental interest to understand how flow and mixing influence CCV and what methods can be used to track these influences back in time towards their sources. To this end, here the pressure-trace analysis is combined with combustion luminosity, LIF, and PIV imaging. From a base case with PFI, a case with DI was examined using two main tools, conditional averaging of slow and fast-burning cycles, and field-wide correlation analysis. The latter technique had been applied to flow-spray interaction in a DISI engine [81] and is expanded here track the influence of flow and mixing from ignition back in time.

3.2 Experimental setup

The experiments were performed in an optically accessible four-stroke single-cylinder DISI engine. Figure 12 shows an illustration of engine and optics, and Table 3 summarizes the operating conditions. The engine was operated at 1500 rounds per minute (rpm), and two different injection strategies were applied. The first operating point (OP) with PFI (titled as PFI) serves as a homogenous reference case. For the second OP (titled as DI) a double injection was implemented using the centrally located 8-hole “Spray G” injector of the international research collaboration “Engine Combustion Network” (ECN). 70% of the fuel are injected at -330°CA and the remaining 30% of the fuel are injected 56°CA before compression TDC. The second injection was at approximately at “Spray G standard” conditions (here, the core gas temperature and density were 238°C and 3.5 kg/m^3 , respectively). To reach this condition, the intake pressure was increased to 1.1 bar, which slightly influences the pressure traces during the compression stroke and results in a higher intake air mass flow but is not expected to influence the flow field. The latter is considered by also increasing the injected fuel mass, so that the global air-fuel ratio remained the same. With $\phi = 0.91$, the mixture was relatively lean, resulting in a COV of IMEP of 1 and 4% for PFI and DI, respectively. Note that the DI strategy was not optimized towards a “useful” cycle outcome, like low COV or high IMEP, but designed to have higher COV than with PFI while still never misfiring.

To minimize the thermal load and the potential influence of residual gas on CCV, each fired cycle was followed by two motored cycles. With DI, fuel was injected only in the fired cycles, while with PFI, every cycle was fueled. For this reason, the global equivalence ratio of the operating point with DI is corrected by the residual gas fraction, which is estimated here to be 10% based on the compression ratio.

The high-speed imaging of flow field and flame and the “low-speed” (crank-angle locked) imaging of the equivalence ratio ϕ were conducted in separate experiments. Flow field and flame propagation were captured simultaneously. Because of the limited image storage capacity of the camera, three measurement series were performed at the same operating condition with

short interruptions in between. These three-image series from 71 fired cycles were combined into a data set of 213 cycles for each OP. In separate experiments the equivalence ratio ϕ for DI was imaged at three selected crank angles (-60, -35 and -20°CA). Here, two series of 100 fired cycles were combined to a set of 200 for each crank angle. A piezoelectric pressure sensor measured the in-cylinder pressure, and the pressure traces were used to calculate the heat release rate, the IMEP, and its COV in both experiments.

Table 3. Engine and operating conditions.

	PFI	DI
Bore x stroke	84 mm x 90 mm	
Compression ratio	9:1	
Engine speed	1500 rpm	
Fuel	98 % iso-octane + 2% anisole	
Spark timing	-20°CA	
Equivalence ratio ϕ	0.91	
Intake temperature	55°C	
Intake pressure	1 bar	1.1 bar
Injection timing	-	-330°CA / -56°CA
Injected fuel mass	24 mg	21.6 mg / 10 mg
IMEP	7.7 bar	7.8 bar
COV of IMEP	1%	4%

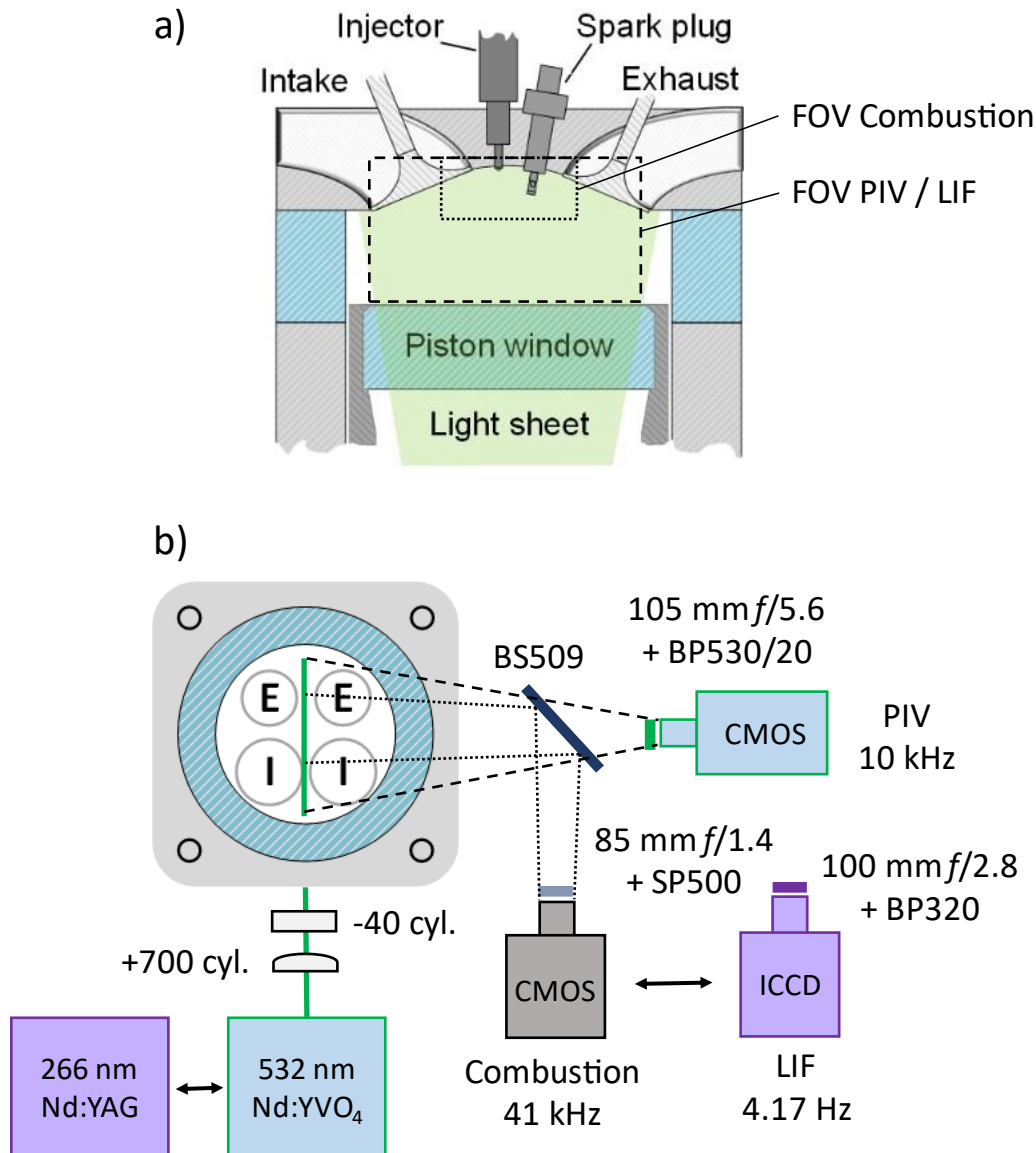


Figure 12. Sketches of (a) optical engine with the fields-of-view of the two measurements and (b) imaging optics.

3.2.1 Optical diagnostics

Optical access is given by a fused-silica cylinder liner and a flat piston window. For PIV, a frequency-doubled, single-cavity Nd:YVO₄ laser (Edgewave IS335, 532 nm, 1 mJ/pulse) was operated with 20 μ s between the pulses illuminating two related images. In the combustion chamber the vertical 0.6 mm thick laser sheet illuminated the central tumble plane. Silicon oil droplets ($\sim 1 \mu$ m diameter) were seeded 50 cm upstream into the intake. A CMOS camera (Photron SA-Z) with a 105 mm lens at f/5.6 captured the light scattered by the silicon oil droplets, operating at 20 kHz (i.e., image pairs were acquired at 10 kHz). PIV imaging started at -180°CA and continued to ignition timing. Due to the high intensity of the scattered light from the second injection in DI useful vector fields could not be calculated between -56 and -36°CA . Simultaneously, another CMOS camera (Phantom v7.3) with an

85 mm lens at f/1.4 imaged line-of-sight integrated blue combustion luminosity at a frame rate of 41 kHz. This chemiluminescence imaging started at -29°CA and ended 5°CA after TDC. Images that are taken before the spark event are used for background correction.

For the equivalence ratio ϕ , laser pulses from a frequency-quadrupled Nd:YAG laser at 266 nm were formed to a light sheet and directed into the combustion chamber illuminating the same central tumble plane as in the PIV measurements. The fluorescence signal from 2% anisole (methoxybenzene) dissolved in the iso-octane fuel was captured by an intensified CCD camera (LaVision IRO) with a 100 mm f/2.8 UV lens. 2×2 pixel hardware binning was set. The gate was set to 150 ns, and the gain was 65 (as set in the control software DaVis). One image was acquired at a selected crank angle in each fired cycle. To block scattered laser light and to detect only the part of the anisole fluorescence spectrum with lower temperature sensitivity [50] (Fig. 4) a 40 nm-wide bandpass filter centered at 320 nm (Semrock) was used. The pulse energy was about 20 mJ/pulse. All cameras' approximate fields of view (FOV) are shown in Figure 12.

3.2.2 Data processing

PIV vector calculation was done with LaVision's DaVis 8.4. In pre-processing, to eliminate background such as from laser light reflections, a Butterworth high-pass time filtered image (7 images time window) was subtracted from each raw image. Also, a sliding background subtraction (100×100 pixel) and a local intensity normalization (5×5 pixel) were used. For vector calculation, a multi-pass cross-correlation with the window size decreasing from 64×64 to 32×32 pixels with an overlap of 50 % was applied and vectors with a peak ratio <1.3 were removed. This resulted in a vector spacing of $914 \mu\text{m}$.

To extract spatial information from the chemiluminescence images, a global region of interest was defined by masking out the cylinder roof and the border regions. An average background of 30 dark images in each cycle before the spark event was subtracted from the flame images, and a 5×5 pixel median filter reduced pattern and shot noise. The apparent burnt area of size A_{flame} was extracted using a "predictor-corrector scheme" that segments the image using a dynamically adjusted intensity threshold [82]. From that, the equivalent flame radius calculated as $r_{flame} = (A_{flame}/\pi)^{1/2}$ [9].

For the LIF images \mathbf{I}_{DI} the images \mathbf{I}_{PFI} of the homogenous PFI reference case serve as calibrating "flat fields" while cycles without fuel injection provided background images \mathbf{I}_{BG} . Dividing the background-corrected single shots by the average flat field and multiplying it with the global equivalence ratio of PFI yields the equivalence ratio images $\mathbf{I}_{\phi, DI}$:

$$\mathbf{I}_{\phi, DI} = \frac{\mathbf{I}_{DI} - \langle \mathbf{I}_{BG} \rangle}{(\langle \mathbf{I}_{PFI} \rangle - \langle \mathbf{I}_{BG} \rangle)} \phi_{PFI} \quad (8)$$

where bold font indicates two-dimensional image quantities and $\langle \rangle$ multi-cycle averaging. The global temperature and pressure dependency of anisole fluorescence is taken into account by recording the PFI calibration images under the same conditions and at the same crank-angle as with DI. The influence of local deviations in temperature associated with the local

(inhomogeneous) equivalence ratio is minimized by detecting only the longer-wavelength part of the anisole fluorescence. Experiments with the same filter as used here (Semrock 320/40) showed that with air as the bath gas, the LIF signal detected at 650 K varies only 10% for a variation of 100 K [50].

To identify regions in the flow or mixture field that are correlated with a measure of combustion speed (early flame propagation or CA10), “correlation maps” were created, as suggested by, e.g., [81]. The idea behind correlation maps is to look how well some single-value quantity correlates with a scalar field quantity at any point in a two-dimensional field. Here, the equivalent flame radius 11°CA after ignition timing [$r_{flame}(-9^\circ\text{CA})$] was correlated with the velocity magnitude $|v|$, and CA10 was correlated with the equivalence ratio ϕ . The correlation coefficient $R_{x,y}$ is defined as

$$R_{x,y} = \frac{\sum_{i=1}^n (x_i - \bar{x})(y_i - \bar{y})}{\sqrt{\sum_{i=1}^n (x_i - \bar{x})^2 \sum_{i=1}^n (y_i - \bar{y})^2}} \quad (9)$$

with $x = |v|$ or ϕ , and $y = r_{flame}(-9^\circ\text{CA})$ or CA10. This results in two time series of correlation maps. The correlation coefficient varies between -1 and 1, where $|R_{x,y}| < 0.3$ implies a low degree, $0.3 < |R_{x,y}| < 0.5$ some degree, $0.5 < |R_{x,y}| < 0.7$ a significant degree, and $|R_{x,y}| > 0.7$ a high degree of dependence [83](p. 142-144).

3.3 Results

We first examine the correlation of flame imaging and pressure-trace analysis. A scatterplot of the equivalent flame radius at -9°CA (11°CA after ignition timing (AIT)) versus CA10 is shown in Figure 13. The correlation value for PFI and DI is 0.77, and 0.83 respectively - both indicating a strong correlation. This means that cycles can be classified as ‘slow’ or ‘fast’ based on either the imaging data or the classic pressure-trace metrics, but the former provides an earlier indication of the cycle outcome than the latter, qualitatively confirming one of the central findings of Aleiferis et al. [8,9].

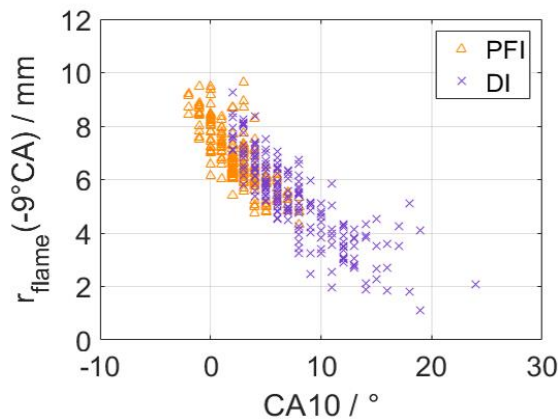


Figure 13. Equivalent flame radius (b) at -9°CA vs. CA10 for all cycles in both OPs.

Figure 14 gives more detailed information on the spatio-temporal characteristics of flame propagation. Here, the probability of finding burnt area in a given pixel is shown as the mean over the 35 fastest and the 35 slowest cycles, based on their CA10. The figure also shows the centroid position of the burnt area in each cycle. For both OPs in fast cycles the flame spreads randomly around the spark plug, yielding a round to oval area of high probability without a clear outer edge. In slow PFI cycles the apparent burnt area remains near the spark plug and slightly moves towards the intake valve. In contrast, for slow DI cycles the flame spreads towards the exhaust side. The fast PFI cycles are faster than the fast ones with DI, and the same is true for each OP's slow subset. In slow PFI cycles the flame has a circular shape, while in slow DI cycles it is more an oval. Comparing the fast and the slow PFI cycles across crank angles with approximately equal flame extent, for example fast at -13° vs. slow at -8.8° CA, it can be seen that the flame centroids are further apart for the fast cycles, consistent with the more random spread of the flame diagnosed above. To see what might cause all these differences, next the in-cylinder flow preceding combustion is examined.

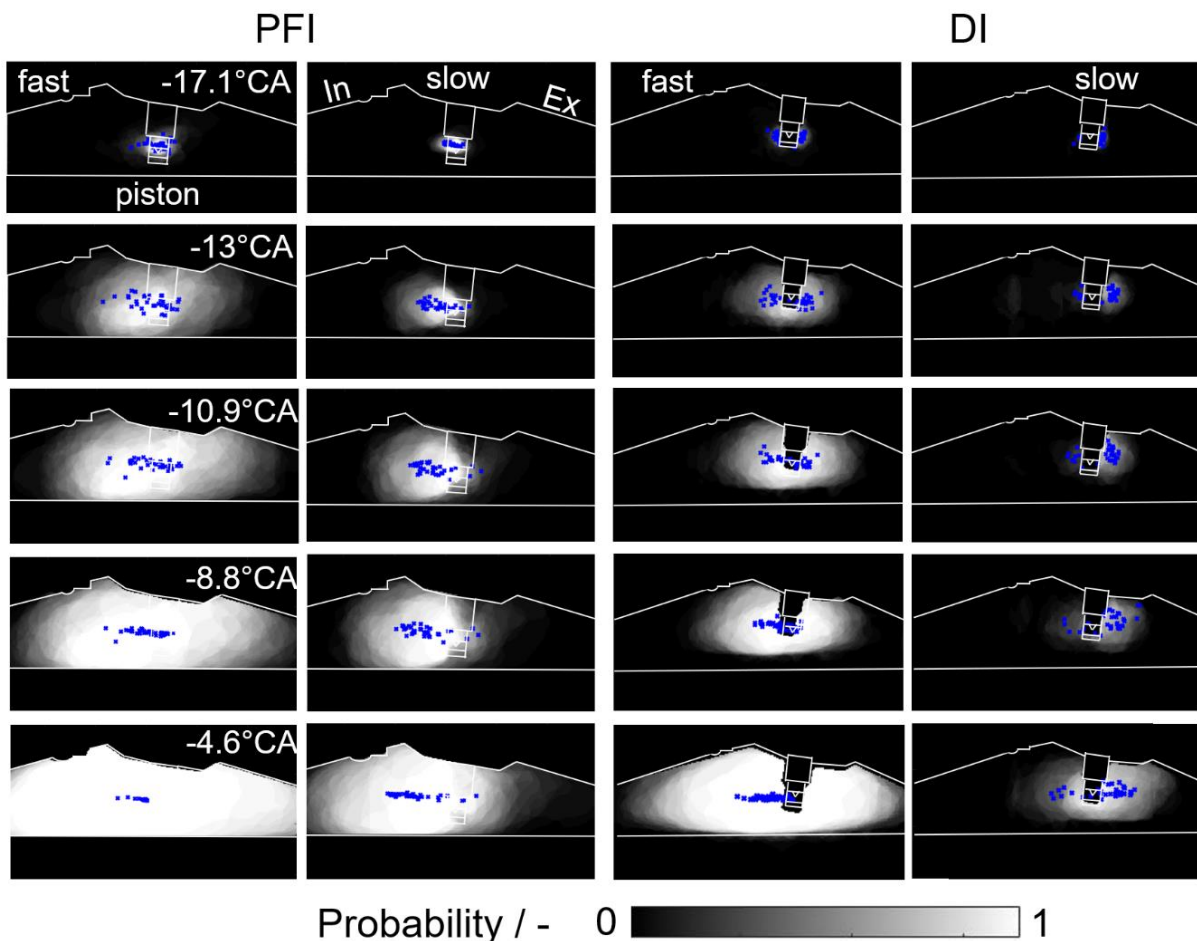


Figure 14. Mean probability of finding burnt area at a given location for the 35 fastest ('fast') and 35 slowest ('slow') cycles (by CA10) during early flame propagation. The blue markers indicate the centroid position of each cycle's burnt area.

In Figure 15 the velocity fields conditionally averaged over the fast cycles and slow cycles are shown. For PFI throughout most of the FOV, the flow at -90° CA is faster in the slow cycles

than in the fast ones. From -45°CA on, the inverse is true – now for PFI the fast burning cycles also have the faster mean flow. This is consistent with the notion that it is the kinetic energy late in the cycle, towards combustion, that matters for turbulent flame propagation. There is a marked difference for slow vs. fast cycles developing in the location of the tumble vortex. The vortex center in slow cycles moves towards the exhaust side but remains in the center in fast ones. In general, towards TDC the round shape of the tumble vortex is not compliant with the increasingly vertically constrained geometry of the combustion chamber. This vertical compression creates shear and breaks up the vortex [84]. Since the pent-roof has most headroom in the center, a vortex localized there can keep its momentum longer, transferring its large-scale energy later into turbulence. Another flow feature in the PFI case that is visible after -45°CA is a region of strong “sweeping” flow above the piston, directed upward and towards the intake. Here, the velocity is higher for fast cycles than slow cycles. This flow feature appears to arise from the combination of the centrally located vortex and the upward movement of the piston. The standard deviation at -19.8°CA is low in this region between spark plug and piston top, which means that the flow is quite stable here. In comparison to that, in both fast and slow cycles the region where the vortex center is located has a higher standard deviation, indicating that small deviations in the vortex location cause high variations near its center, but less farther away from it.

At -90°CA , i.e., before the second injection, DI is very similar to PFI, indicating that the first injection that occurred at -330°CA during the intake stroke had little influence on the in-cylinder flow during compression. (Note that in DI the small region with near-zero velocities below the intake valve and that on the right side of the spark plug are due to reflections in the background and should be ignored.) But in DI at -36°CA the second injection has taken place shortly before, and it has a significant impact on the flow field. It adds additional turbulence and makes the flow more three-dimensional, which cannot be captured completely in only one imaging plane. However, a vortex is still visible on the intake side next to the spark plug. The orientation of the vectors is almost identical in fast and slow cycles, but almost everywhere, fast cycles have slightly higher velocity magnitudes. As in PFI, the vortex in DI is squeezed by the piston movement during compression. At -24.3°CA the vortex center is less pronounced in DI than in PFI, which can have two reasons. Either the two-dimensional plane does not capture the vortex anymore or the vortex starts to dissipate earlier. The standard deviation at ignition (-20°CA) is higher for fast cycles than for slow cycles, is overall higher for DI than for PFI, and reaches its peak on the intake side next to the spark plug. A visual inspection of the single-cycle flow fields (not shown here) reveals that with DI the vortex has mostly dissipated, while with PFI a more coherent flow remains. The direction of the vectors in DI at -20°CA is still the same for fast and slow cycles. However, the slow cycles have higher velocities on the intake side of the spark plug, directed towards the exhaust side, while in fast cycles there is a local counter-flow with similar velocity magnitudes on both sides.

The flow behavior at ignition timing is linked with subsequent flame propagation (Figure 14). As noted above, with PFI at -19.8°CA the vortex center is associated with a region of elevated

standard deviation in velocity magnitude, but in fast cycles, this region is exactly around the spark plug. The associated cycle-to-cycle variation in the vortex center's location exposes the spark to different flow directions. For example, if the vortex center is located on the intake side and below the spark plug, the spark is carried to the intake side, while the opposite is the case when the center is located on the exhaust side. The varying location of the vortex center for fast cycles is therefore very likely to be the reason for the variation in the location of the burnt area. Conversely, if the vortex center is always on the same side of the spark plug, like in the slow cycles of PFI, the flow always convects the flame to the same side, even when the location of the vortex slightly varies.

In DI, at ignition (-20°CA) the flow in slow cycles has a higher velocity magnitude on the intake side of the spark plug than the counter-flow on the opposite side of the spark plug. This flow behavior results in a movement of the flame to the exhaust. In contrast, the velocity magnitude in fast cycles is approximately the same on both sides of the spark plug, which may lead to the observed spreading in the flame probability.

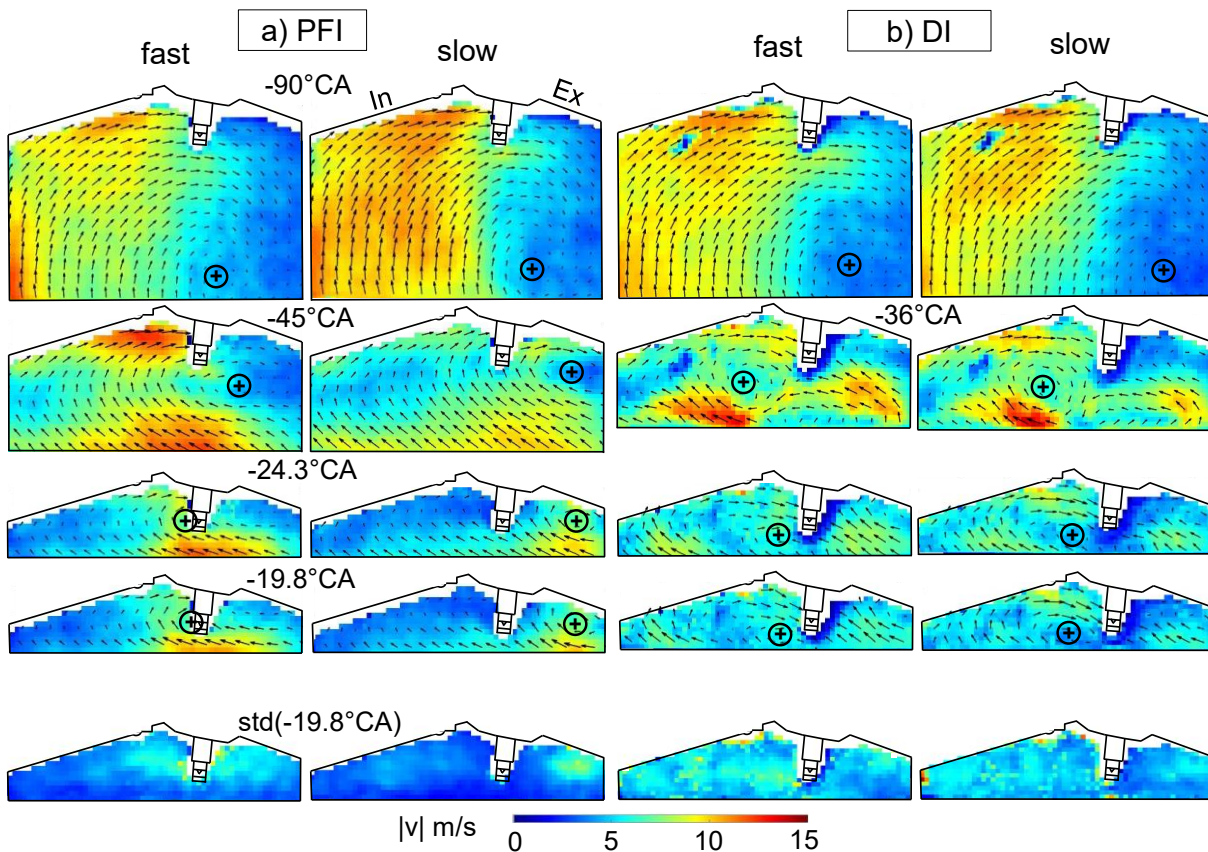


Figure 15. Selected mean velocity fields for the 35 fastest and 35 slowest cycles (by CA10) for (a) PFI and (b) DI. For DI, due to the spray of the second injection the vectors fields at -45°CA are highly inaccurate, and the first reliable flow field after the injection (at -36°CA) is shown instead. The black + marker indicates the visually determined center of the tumble vortex. The last row shows the standard deviation of the velocity magnitude across each data sub-set at -19.8°CA .

To better link the flame and flow data, correlation maps were created (based on all 217 cycles for each OP). Figure 16 shows the correlation of the vector magnitude $|v|$ with the equivalent flame radius at -9°CA . Any correlation can now be traced back in time, and in fact Figure 16 has been arranged in reverse temporal order to facilitate that narration.

In the base case with PFI a patch of strong correlation around the spark plug can be seen at ignition timing (-20°CA). Looking back in time, this region is expanding until -40°CA without decrease in the correlation coefficient. Interestingly, the vortex center is surrounded by a ring of high correlation coefficients where the gradient between near-zero mean flow at the vortex center and the faster flow around it is located. Also, from ignition back to -50°CA the sweeping flow above the piston and below the spark plug shows a high correlation. This region may disappear with the piston top from the field of view at earlier CAD. Peterson et. al. [59] also found a correlation between the upward-sweeping flow in this region and combustion. At -50°CA the patch of high correlation near the spark plug and around the vortex center slightly decreases and start to split up into several smaller regions. Going now backwards in time the region of higher correlation below the inlet slowly decreases towards -90°CA until it is not visible anymore. However, the region immediately to the left of the tumble vortex center increases in spatial extent and magnitude. Again, it is not at the vortex center that the highest correlation is found, but next to it. Comparing the correlation maps at -40 (or -50) and -90°CA with the conditional averages in Figure 15 it can be seen that these high-correlation areas are exactly where the differences in flow magnitude between slow and fast cycles are found.

Compared to PFI, DI almost always has much lower correlation coefficients. From -20 to -36°CA several higher-correlation patches are located roughly around the vortex center. This is consistent with the lack of cylinder-wide coherent flow that is in turn ascribed to the second injection at -56°CA , but also with the fact that with DI a second parameter of influence appears, namely mixture inhomogeneity, which will be assessed in the next section. However, at -60 and -75°CA (before the second injection) there is a relatively large region in the center of the FOV where higher correlation coefficients occur. This is somewhat surprising but may be due to the three dimensional nature of the flow that is captured only partially by the current planar PIV measurement or due to a causal chain between flow-spray-flame, i.e, the pre-injection flow influences the spray and thereby the mixture formation and finally the flame [81]. At -90°CA the correlation value has decreased below 0.2.

These correlation maps illuminate the causal chain between flame and large-scale flow as they are able to identify regions that are likely to influence the early flame kernel growth with PFI. However, with DI the second injection suddenly inserts smaller-scale turbulence, and moreover it may stratify the mixture to an extent where the flow is not the dominating influence on the flame propagation anymore. Therefore, for the DI case the focus lies now on the local equivalence ratio ϕ .

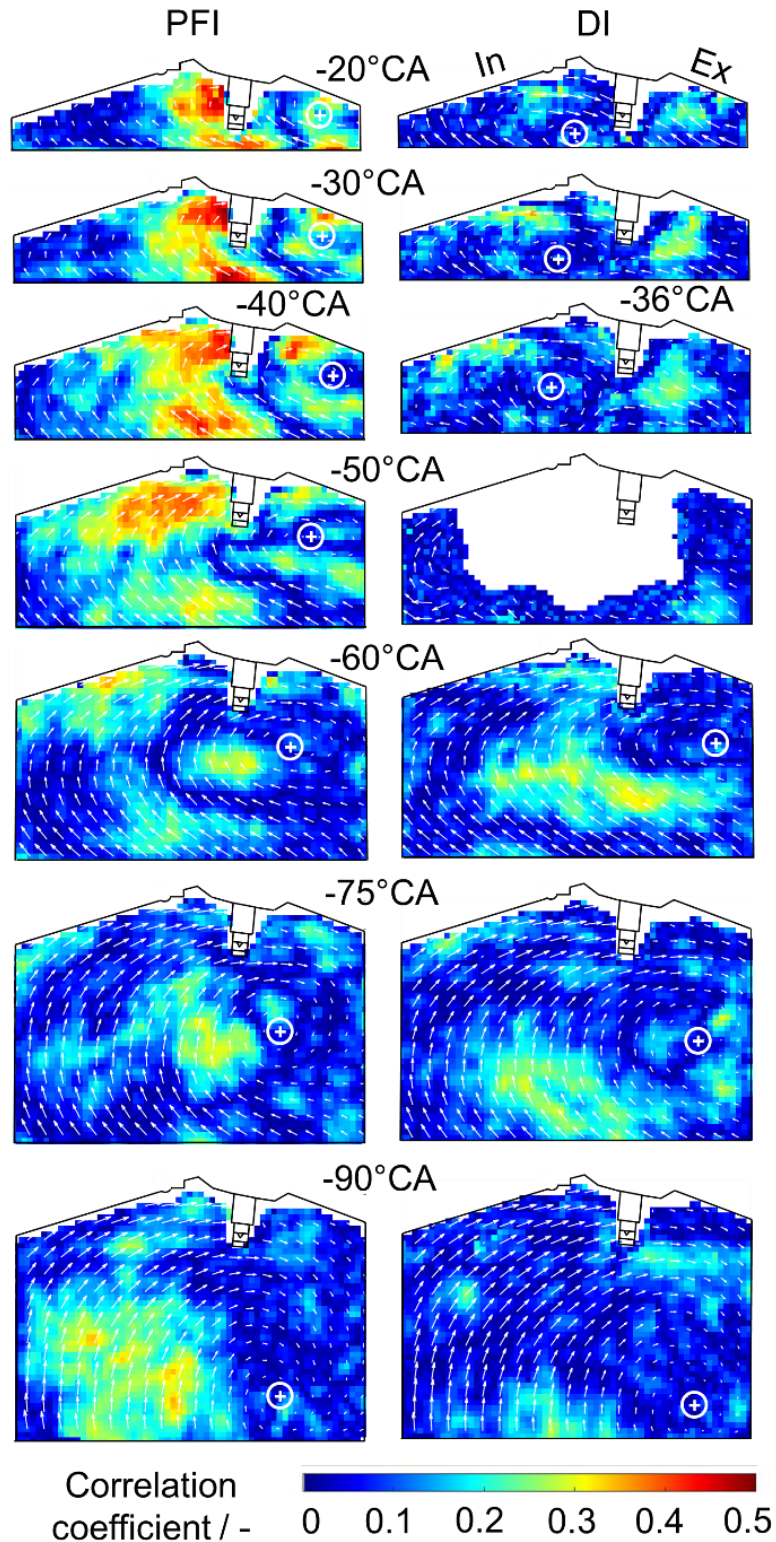


Figure 16. Correlation maps of the velocity magnitude with the equivalent flame radius at -9°CA .

For the DI case, Figure 17a shows conditional ‘fast’ and ‘slow’ 35-cycle averages of the equivalence ratio and typical corresponding single shots. The near vertical “stripes” in the images stem from shot-to-shot fluctuations in the transverse laser beam profile. They have a modulation of about 6% (one standard deviation) which should not preclude reaching

qualitatively meaningful conclusions. The images at -60°CA show that, as intended, the first injection at -330°CA generates an almost homogenous, globally lean mixture. However, there is a leaner region above the piston, slightly more so for fast cycles than for slow ones. The single shots show the corresponding gradients better. It seems that in this mixture before the second injection, a typical fast cycle has more stratification than a slow cycle.

The second injection introduces much stronger mixture inhomogeneity. At -35°CA most of the fuel is still close to the piston top for both fast and slow cycles. At ignition timing (-20°CA) in slow cycles the fuel is concentrated more at the intake side and a leaner region is found around the spark plug. Fast cycles also have more fuel on the intake side, but the richer region it is horizontally extended and the equivalence ratio around the spark plug is approximately 1. This would lead to better conditions for the early flame kernel. The flame imaging summarized in Figure 14 showed that slow cycles burn towards the right, and the flow fields in Figure 15 indicated that this is partly because in slow cycles the generally right-ward flow near the spark plug is stronger. Additionally, it can be seen that for fast cycles the immediate vicinity of the spark has better mixture conditions to the left of the spark plug, which may make it easier for the flame to propagate left against convection.

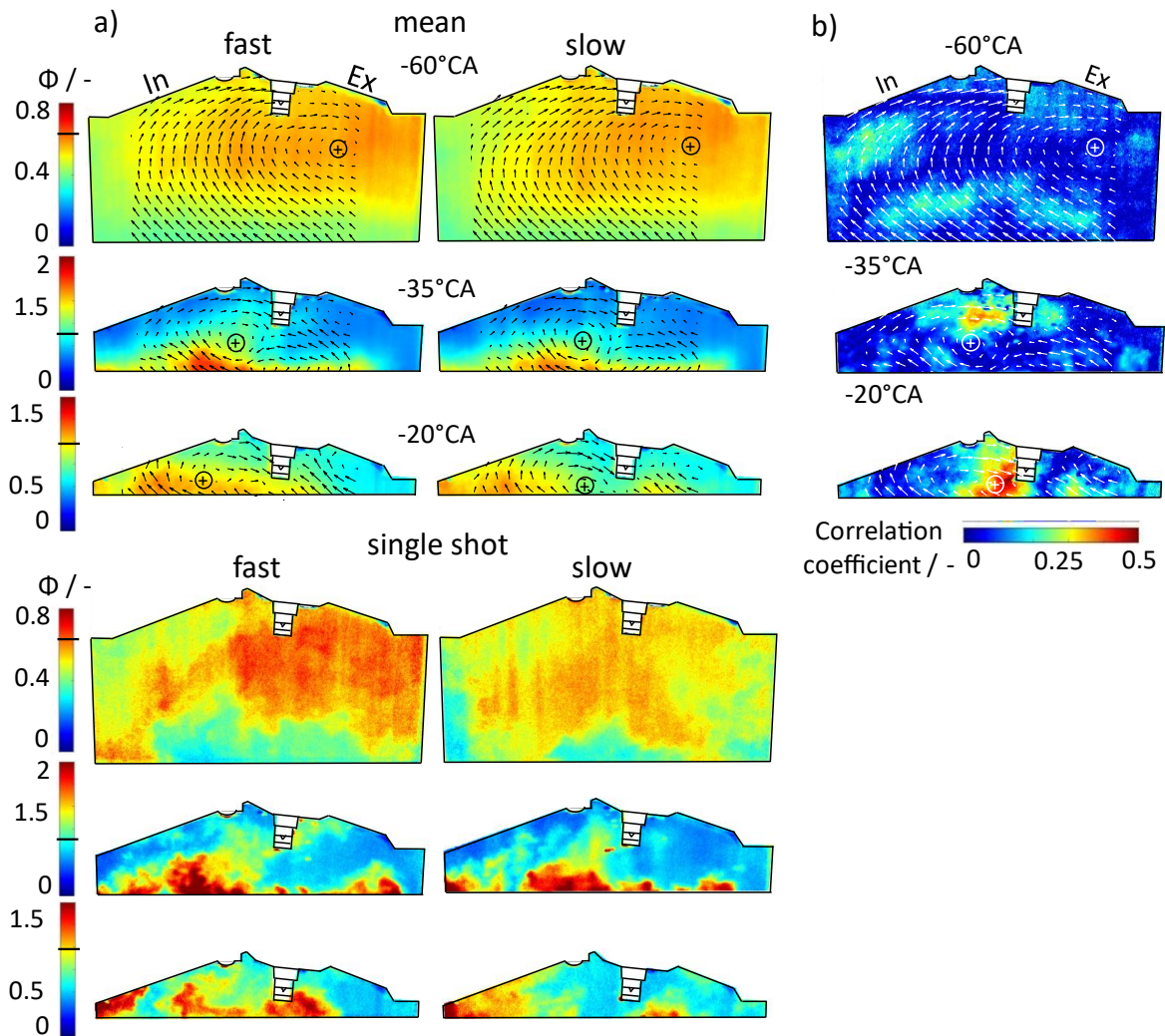


Figure 17. (a) Equivalence ratio at selected crank angles. First and second column: Conditional average over the 35 fastest and 35 slowest cycles superimposed by the averaged flow fields from Figure 15. Third and fourth column: corresponding typical single shots selected from each 35-image subset. (b) correlation maps of the equivalence ratio and CA10 superimposed with the average flow field from Figure 15

In Figure 17b the correlation between the equivalence ratio in each pixel and CA10 is shown. As expected, at ignition timing there is a strong correlation around the spark plug. In particular the region on the intake (left) side has more influence on CA10 than on the exhaust side, where the correlation coefficient is almost zero. This is consistent with the earlier conclusion that fast cycles occur when the early kernel can expand against the flow to the left. Earlier in time at -35°CA the region of stronger correlation remains but decreases in value. The small spots of low correlation stem from liquid fuel droplets that saturate the camera sensor. At -60°CA , before the second injection, the correlation coefficient is much lower. However, what little correlation exists is found in the regions where significant gradients are seen in the equivalence ratio in Figure 17a.

3.4 Chapter conclusions

This work used several optical imaging techniques to investigate CCV in the early flame for gasoline PFI and central DI with moderate fuel inhomogeneity at ignition. The latter used a split injection that delivered about one-third of the fuel late at -56°CA . Two main tools were used in the analysis, averaging of the image data conditional on cycles being among the 35 fastest or slowest burning ones, and correlation maps that quantify how well a single-value quantity correlates with a scalar field quantity at any point in a two-dimensional field. Both were found to yield useful and complementary insight.

In flame luminosity imaging, for PFI slow cycles are more likely to burn towards the intake side of the spark plug, but for DI, to the exhaust side. For both PFI and DI in fast cycles the location of the flame varies much more, but on average is more centered around the spark plug.

In flow fields from PIV, with PFI the vortex center in slow cycles moves horizontally towards the exhaust side of the combustion chamber, whereas the vortex center in fast cycles remains more in the center, which appears to help maintain higher bulk flow velocities until closer to TDC. The second injection in DI changes the flow field completely. Afterwards, for both fast and slow cycles the vortex center is found on the intake side of the spark plug.

Correlation maps of the velocity magnitude with the equivalent flame radius at -9°CA were analyzed. For PFI, the maps reveal large regions that predict the speed of the combustion process, in particular below the center of the pent-roof and an upward “sweeping” flow above the piston. Some of these regions can be traced back in time to about -90°CA . The second injection of DI results in a different location of the relevant region, and with lower correlation coefficient. In all cases regions of high correlation with the early flame do not coincide with the tumble vortex center, but are instead adjacent, sometimes arranged in a loose circular pattern around it. High-correlation areas are where the greatest differences in flow magnitude between slow and fast cycles are found.

For DI, the equivalence ratio was measured with tracer LIF and then correlated with CA10. After the second injection, regions of high correlation are to the immediate left of the spark plug, where in fast cycles a distinct gradient towards a fuel-rich zone is found, but not in slow ones. This is upstream against the local flow, suggesting that the mixture gradient enables the flame to burn against local convection, enlarging the region that is “available” for the early kernel. As a result, the flame is then found (in the combustion images) with more equal likelihood everywhere around the spark plug.

4 Statistical analysis of flow field variations via independent component analysis

This chapter is based on the flow field measured and post-processed in the work presented in chapter 3. It was shown that in homogeneous operation with PFI the combustion speed is strongly linked to the flow field during the compression stroke. Therefore, the flow field is analyzed by a decomposition via ICA. The results were presented at the FOR 2687 workshop “Cyclic variations in highly optimized SI engines” in 2022 and a manuscript has been submitted to Experiments in Fluids in October 2023 [85].

4.1 State of the art

Since the turbulent flow in the cylinder of an IC engine is far from isotropic homogeneous turbulence, but instead is structured on a large scale (e.g., swirl or tumble), it is reasonable to assume that CCV in part is driven by variations of large or intermediate spatio-temporal scales [86]. Therefore, one might look for “typical” flow features, which can be linked to combustion metrics such as peak pressure, combustion phasing, and IMEP), such that ultimately engine design can be informed by this insight. For this, a combination of in-cylinder pressure-based combustion analysis and time-resolved imaging diagnostics is needed. High-speed imaging systems with frame rates that are adequate to resolve the turbulent time scales in combination with large storage can collect time-resolved data to study combustion related events on a statistically significant basis [33,56]. Next, objective and automated processing tools are needed to analyze the large amount of imaging data.

Besides relatively simple methods e.g. conditional averaging [74], proper orthogonal decomposition (POD) has found a range of applications in combustion research, including internal combustion engines [87–89]. POD decomposes data in terms of dominant structures by energy and frequency [90–93]. However, in the resulting decomposition, even the leading-order modes do not necessarily resemble “typical” flow features, i.e., features that one might recognize in a given single cycle [90]. POD is a good tool to compare data sets [94] or to identify subsets of data that have common features [95], but the connection between what is found in the POD mode structures and their coefficients on one hand and physical processes on the other is not a-priori guaranteed or obvious.

It appears that an alternative method, or at least further processing, is required to extract features that can be directly connected with observed flow and combustion behavior. This work explores if ICA of vector fields can extract flow features that are potentially responsible for the difference between late and early burns in lean spark-ignited premixed iso-octane/air combustion in an engine. The example studied here utilizes high-speed PIV to investigate cycle-to-cycle combustion variation in an optically accessible research engine.

Independent component analysis is a statistical tool used in various fields. Like POD, it is also based on single value decomposition [96]. Hyvärinen et al. [97] investigated ICA in terms of

mathematics and statistics and their research group provides an open-source code for MatLab©, FastICA [98].

The classic example for ICA is the so called “cocktail party problem”. Voice signals are randomly mixed, and the task is to extract the individual speakers’ voices. ICA or POD can be used to separate the single source signals. While POD just gives a set of dominant mixtures, ICA is able to extract the independent sound sources. The difference between ICA and POD is that ICA extracts statistically independent and non-Gaussian components from large datasets. This means that underlying statistically independent structures (blind sources) in signal mixtures are separated by ICA, while POD modes are always mixtures of dominant patterns [91]. ICA is used without knowledge of the physically properties of the sources and therefore the number of independent components in a dataset is usually unknown [99,100]. However, in contrast to POD, ICA does not sort dominant structures by level of energy.

The application of ICA in engine research is quite rare. Bizon et al. [99,101,102] showed that ICA with two components applied to images of flame luminosity in a diesel engine could identify two separate combustion events, the main combustion zone along on the central spray axes and the later combustion near the piston bowl. Bizon et al. [101] also studied how ICA could be used to study the evolution of combustion luminosity for individual cycles and cycle sequences. They showed that time-dependent coefficients carry information about the CCV morphology. ICA could extract and separate moving sources from the background using a nonlinear mixing model. This was further elaborated on using artificial examples to show the limitations of applying linear ICA to nonlinear mixtures. A study based on direct numerical simulation (DNS) used ICA is used to analyze the streamwise velocity fluctuations occurring in turbulent channel flows. The results indicate that ICA may be suitable to connect statistical with structural descriptions of turbulence [103].

Since ICA appears to fulfill the intended task of identifying “typical” large-scale structures in scalar images, it should also be applicable to velocity fields, which is explored in this work. It is demonstrated that ICA of vector fields works and provides a plausible physical picture of the processes leading to either early or late burning cycles.

4.2 Experimental set-up and PIV measurements.

4.2.1 Optical engine and operating conditions

Flow imaging was performed by high-speed PIV in an optically accessible four-stroke single-cylinder SI engine with four valves and a pent-roof. Figure 18 illustrates the relevant part of the engine, and Table 4 summarizes the operating conditions. The engine was operated at 1500 rpm, and flow fields were captured from -90 to -20°CA (i.e., for 70 crank angles) in 213 fired cycles. Running the engine in “skip-fired” mode, each fired cycle was followed by two motored cycles, which decreases the thermal load and the potential influence of the residual gas on CCV. The fuel was injected via PFI, which yields a near-homogenous mixture at the timing of ignition. From each cycle’s record of the in-cylinder pressure trace, the heat-release rate

(HRR) was calculated, and CA10 was used as an indication of the speed of the initial phase of combustion.

Table 4. Engine properties and operating conditions.

Engine Type	4-stroke single cylinder
Fuel	Iso-octane
Air-fuel ratio λ	1.1
Bore / stroke	84 / 90 mm
Geometric compression ratio	9:1
Engine speed	1500 rpm
Intake pressure	1 bar
Spark timing	-20°CA
IMEP	7.7 bar
COV of IMEP	1 %

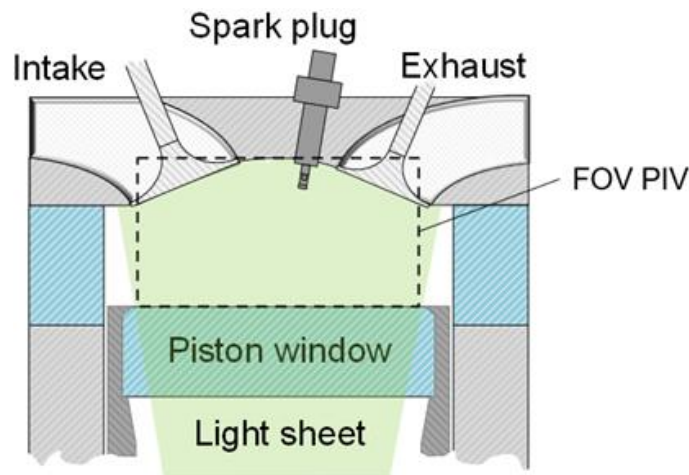


Figure 18. Sketch of the optical engine with the field of view.

4.2.2 Optical diagnostics and image processing

A fused-silica cylinder liner and a flat piston window provided optical access. Silicone-oil droplets were introduced ~50 cm upstream in the intake manifold. Two laser pulses from a frequency-doubled Nd:YVO₄ (Edgewave IS335, 532 nm, 1 mJ/ pulse, 9 ns pulse duration), temporally separated by $\Delta t = 20 \mu\text{s}$ illuminated the tumble plane in a 0.6 mm thick light sheet. The light scattered by the oil droplets was imaged by a CMOS camera, with 10,000 image pairs acquired per second, corresponding to about one image pair per crank angle. From each image pair, velocity vectors were calculated using LaVision's DaVis 8.4. Multi-pass cross-correlation with an interrogation window size decreasing from 64 x 64 pixels to 32 x 32 pixels with 50% overlap resulted in a vector spacing of 914 μm . The moving average of 5 images was calculated

before ICA was applied. A more detailed description of the diagnostics and the image analysis can be found in chapter 3.2.

4.2.3 Pressure-based analysis and PIV measurements

In Figure 19 the pressure traces and the pressure-based quantity CA10 are plotted. With ignition at a -20°CA and a relatively lean mixture of $\lambda = 1.1$, the IMEP at this operating point is 7.7 bar with a COV of 1%, which would be considered perfectly acceptable operating stability in a production engine. Nevertheless, as is typical for spark-ignited engines, the pressure traces show significant variability. A histogram of CA10 is shown in Figure 19b. The distribution is near-Gaussian, slightly skewed to earlier crank angles and with the peak bin centered at 3°CA after combustion TDC. The mean is at 2.4°CA . 74% of the cycles reach CA10 between 0 and 4°CA .

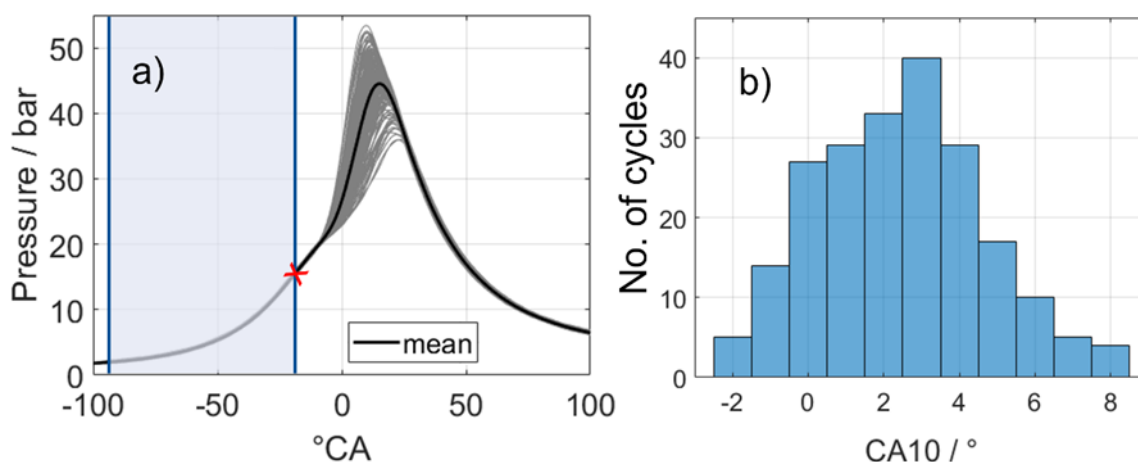


Figure 19. (a) pressure traces for all cycles in grey and their mean value in black. The red x indicates ignition, and the investigated crank-angle (= time) range is marked in light blue. (b) Histogram of CA10.

To give an overview of the flow during compression, Figure 20 shows flow fields for selected crank angles. The first three columns contain flow fields from different single cycles and the last column shows the flow fields averaged over the whole data set. At -90°CA the typical tumble motion can be found in each single cycle and in the average. The tumble vortex center is in a different position for each single cycle, and on average located somewhat to the right of center in the field of view. The peak velocity magnitude also differs from cycle to cycle. At -60°CA the vortex center of the average flow has moved to the exhaust (i.e., right) side of the combustion chamber, and on a single-cycle basis the position of the vortex center still varies. This behavior continues until ignition timing at -20°CA . In Cycle #7 and Cycle #80 a vortex can still be seen close to the spark plug, but in cycle #179 and also the average the tumble vortex is now much less pronounced, reflecting the expected tumble breakdown towards TDC.

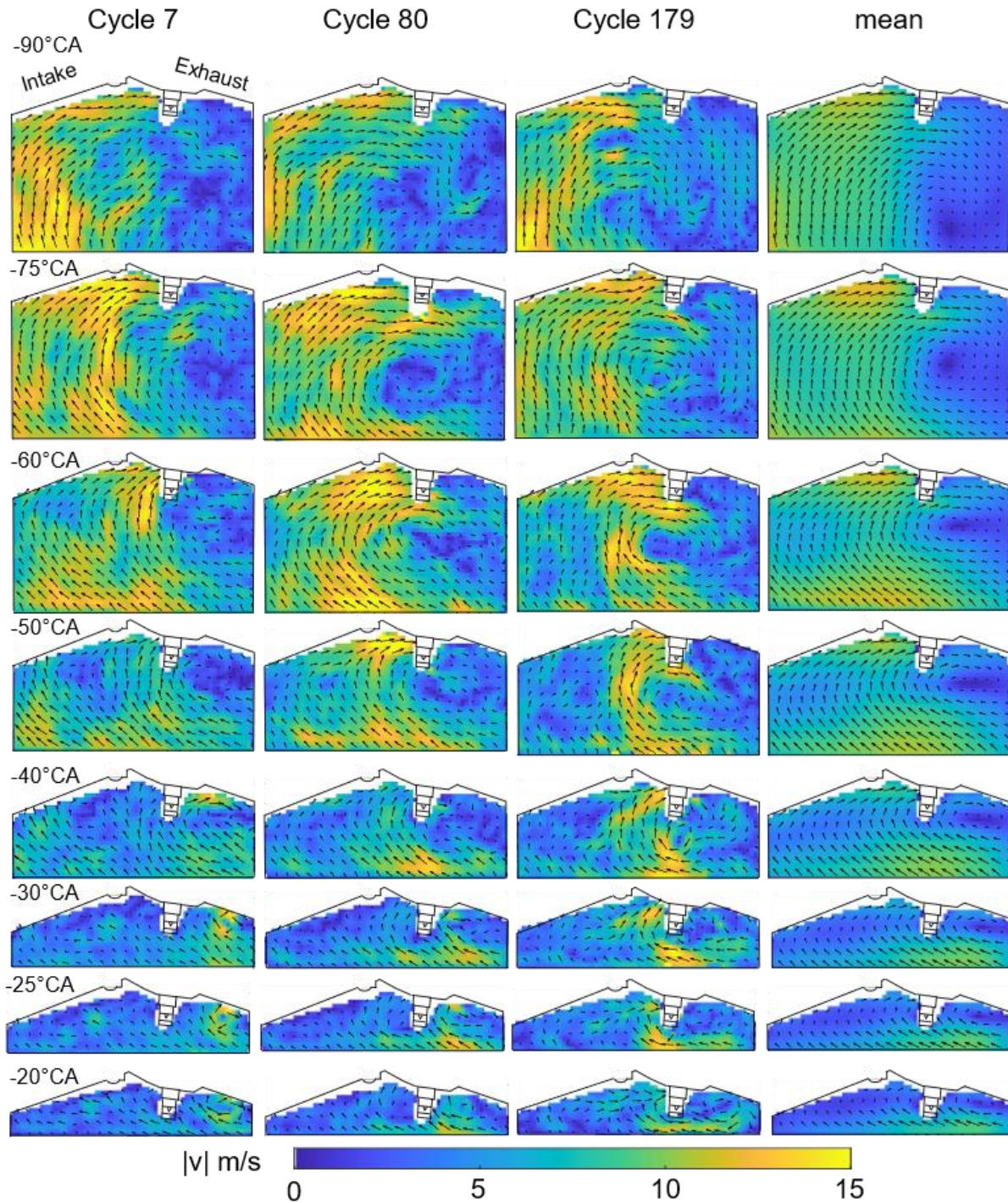


Figure 20. First three columns: flow fields from three cycles at selected crank angles. Fourth column: mean flow at these crank angles. Only every 3rd vector in each dimension is shown.

4.3 Methodology

4.3.1 Snapshot ICA

ICA is a statistical tool for finding underlying independent source flow-structures s_1, s_2, \dots, s_n from a set of flow fields f_1, f_2, \dots, f_m at a given crank angle. Each flow field f contains different proportions of the sources s . To what extent a flow field contains each of these sources is

described in the mixture matrix \mathbf{A} . This mixture matrix provides two pieces of information, the absolute value and the polarity. However, this information is determined through a scaled version of the source signal, thus it is difficult to recover the length and orientation of the vector. The model can be written as

$$\mathbf{f} = \mathbf{A}\mathbf{s} \leftrightarrow \mathbf{s} = \mathbf{W}\mathbf{f}, \quad (10)$$

with $\mathbf{W} = \mathbf{A}^{-1}$. While \mathbf{f} is known from the measurements (here the flow fields), \mathbf{A} and \mathbf{s} are unknown and must be determined iteratively, resulting in the best estimate $\mathbf{y} = \mathbf{W}\mathbf{s}$ that maximizes the statistical independence of these estimated components \mathbf{y} [99]. By assuming that the sources \mathbf{s} are statistically independent, where each source is characterized by a non-Gaussian distribution, the maximization of the statistical independence of the estimate \mathbf{y} solves the basic ICA problem from Eq. (10) [100].

As the number n of the independent sources \mathbf{s} is often unknown and much smaller than the number m of the flow fields \mathbf{f} , the plain application of the ICA model would result in a $m \times n$ mixing matrix \mathbf{A} . Thus, the rank of the data needs to be decreased. This is usually done by preprocessing based on principal component analysis (PCA), for example by POD, so that only a few eigenvalues and vectors remain as input to ICA [96,102].

4.3.2 Synthetic example

To obtain a first understanding what applying ICA to flow fields does, a synthetic example was exercised, as summarized in Figure 21a. Three sources are randomly mixed to create 500 mixture samples. Each mixture contains all three sources, but to a different extent. POD creates as many modes as mixture sample are given to the algorithm. Here, only the first three are shown. The first POD mode φ_1 represents the mean value of all mixture samples. The remaining POD modes are sorted by energy in descending order. None of them resembles any original source. In comparison to that, ICA only provides as many ICs as demanded from the algorithm in the first place. In this case, it is known that exactly three sources exist, and the results show very similar flow fields compared to the original sources. Only the polarity and the absolute value are different, as expected.

More realistically, the number of relevant ICs is not known a priori. A parameter study of the number of ICs is shown in Figure 21b. It can be seen that if the number ICs is smaller than the number of sources, ICA only finds one or two out of three sources, but not a mixture of the three. Repeating the calculation may yield one or two different ICs, but each is always a scaled version of one of the original sources. When the FastICA [98] algorithm searches for more than three ICs (here, 4), it simply returns only three matrices as a result.

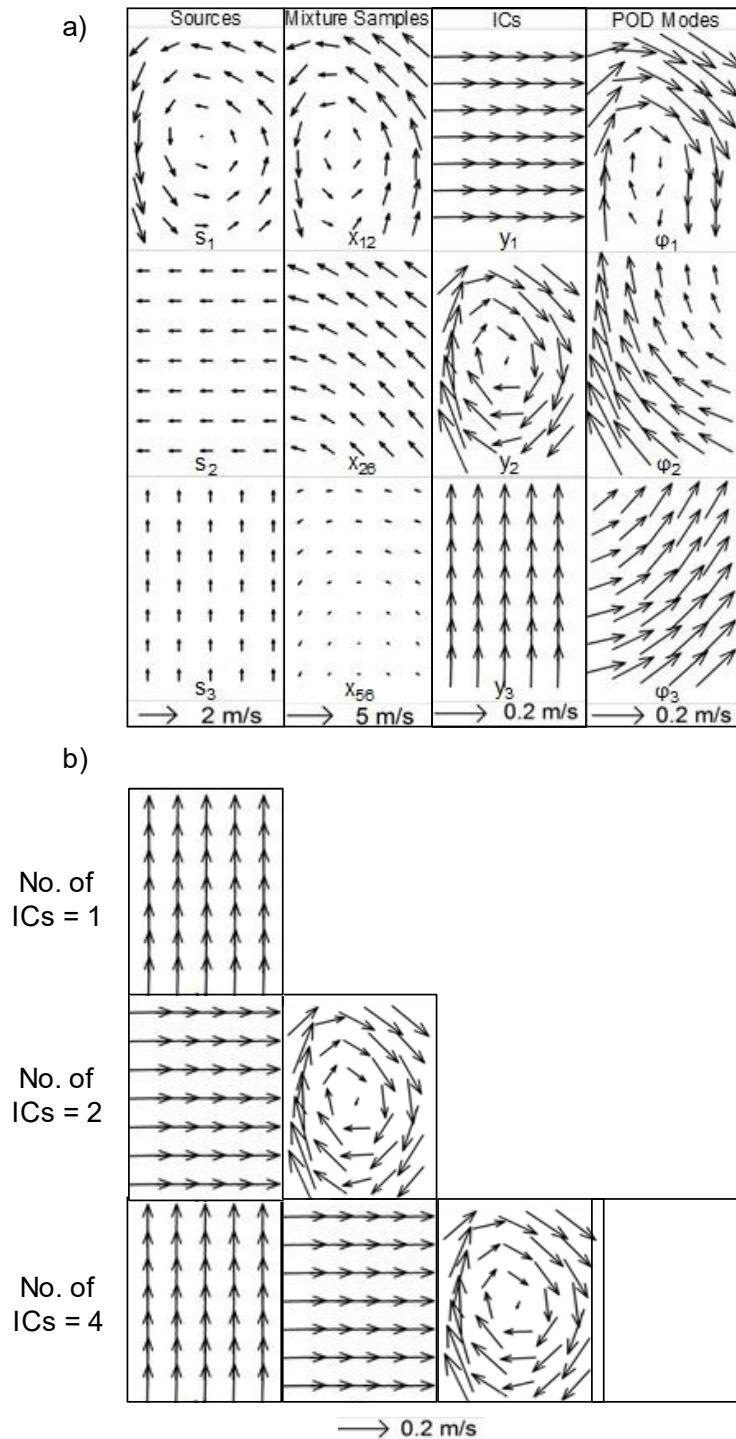


Figure 21. (a) ICA and POD applied to synthetic flow fields with the number of ICs set to the known number of sources (three), (b) the ICs found with different numbers of requested ICs.

4.3.3 Determination of the number of ICs

The synthetic example presented in Figure 21 showed that ICA works in principle on flow fields and that the algorithm is able to extract flow fields that are very similar to the original sources. However, in real engine data two inter-connected challenges exist: first, it is not known *a priori* how many sources exist, and second, the data contains noise. The latter is minimized – at the cost of some temporal resolution – by calculating the moving average of 5 images for each

single cycle before ICA is applied and by only using the lower-order POD modes. The former – not knowing the “relevant” number of ICs – is addressed here by varying the number of ICs (1, 2, 3, 5, 8, 10, and 20) and comparing the results. For completeness, Table 5 shows the portion of the total energy within the POD modes used for the ICA with various numbers of ICs.

Table 5. Cumulative energy contained in POD modes for different numbers of ICs.

Number of ICs	% of energy in POD modes
2	78.8
3	85.1
5	91.6
8	95.3
10	96.3
20	98.7

Figure 22 shows some of the results of this parameter study. Because it is not possible to compare the absolute values of the ICs, the background color represents not the magnitude but the orientation of each vector. This simplifies an initial visual inspection, which was used to manually sort the ICs for the purposes of this figure. For example, the first column of the first row (2 ICs requested) shows a flow directed to the intake side. The three ICs in the second column are arranged such that the first one shows a similar flow pattern, etc. With 8 calculated ICs the pattern is similar, but some smaller-scale structures appear. In this row, the flow in each field is predominantly directed towards the intake side. The ICs in the second row feature a large central vortex. As previously noted, the sign (polarity) of the ICs is arbitrary. Reviewing the second row provides a clear illustration of this. While in the first column (2 ICs) the vortex rotates clockwise, in the second column (3 ICs) it is counter-clockwise.

If 8 (10 or 20, not shown) ICs are calculated, some of the ICs show relatively small flow patterns. One reason might be turbulence. The ICA algorithm first filters the data set through a POD, and if the number of ICs is set to e.g., 10, in a next step only the first 10 POD modes are used to approximate the original sources. The more POD modes are used for the ICA the more turbulence is contained by these higher-order POD modes. Furthermore, the repeatability of the ICA becomes less robust. Calculating 8, 10, or 20 ICs several times results in more variations between runs than returned for a lower requested number of ICs. By calculating 5 or less ICs larger flow patterns are visible. Some of the ICs are visually similar to ICs found with 8 requested ICs, which is taken to be an indication of convergence. Requesting 3 ICs yields close to a subset of the 5 ICs below, and 2 yields a subset of 3. Since the interest lies in large-scale patterns and the goal is to gather as much information as possible, the number of ICs is set to 5, noting that this choice remains somewhat arbitrary.

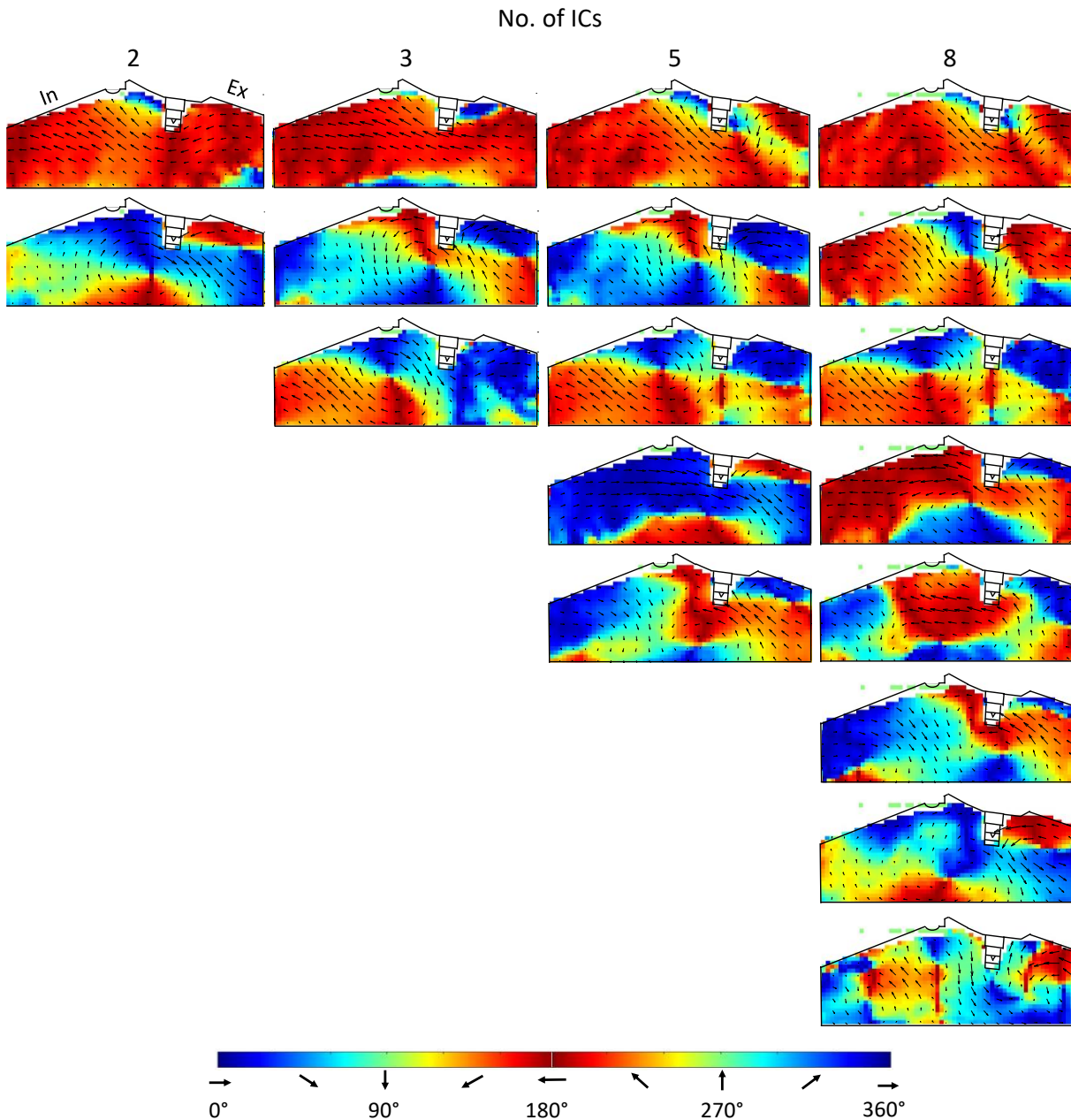


Figure 22. Parameter study with different numbers of ICs at -45°CA .

Applying ICA at a specific crank angle for the decreased data set of 5 POD modes from all 213 recorded cycles results in 70 sets (from the 70 crank angles) of 5 independent components (IC) each. As FastICA requires a scalar input, the two-dimensional velocity field was rearranged. Each u- and v-component of the velocity field with its 49×64 subregions was transformed into a 1×3136 vector. These two vectors were then combined into a single 1×6272 vector which was used for ICA. Reversing the re-arrangement, the output ICs were then separated to obtain the two velocity components, resulting in two matrixes with the original dimensions of 49×64 subregions, i.e., two-component vector fields.

4.3.4 Post-processing

This snapshot ICA finds a set (here, 5) of independent components that are “typical” for the ensemble of flow fields at a given crank angle. Since the ICs are neither connected in time, nor sorted like for example, modes of a POD, further post-processing is indispensable. In this study, two different methods are applied to the resulting data set: a persistence analysis and an analysis of correlation with combustion. The flow chart in Figure 23 illustrates the post-processing. The basic idea behind sorting the ICs is to presume temporal coherence or persistence. That is, for a flow feature occurring during the compression stroke to be relevant for the later combustion event it must persist for an extended period of time.

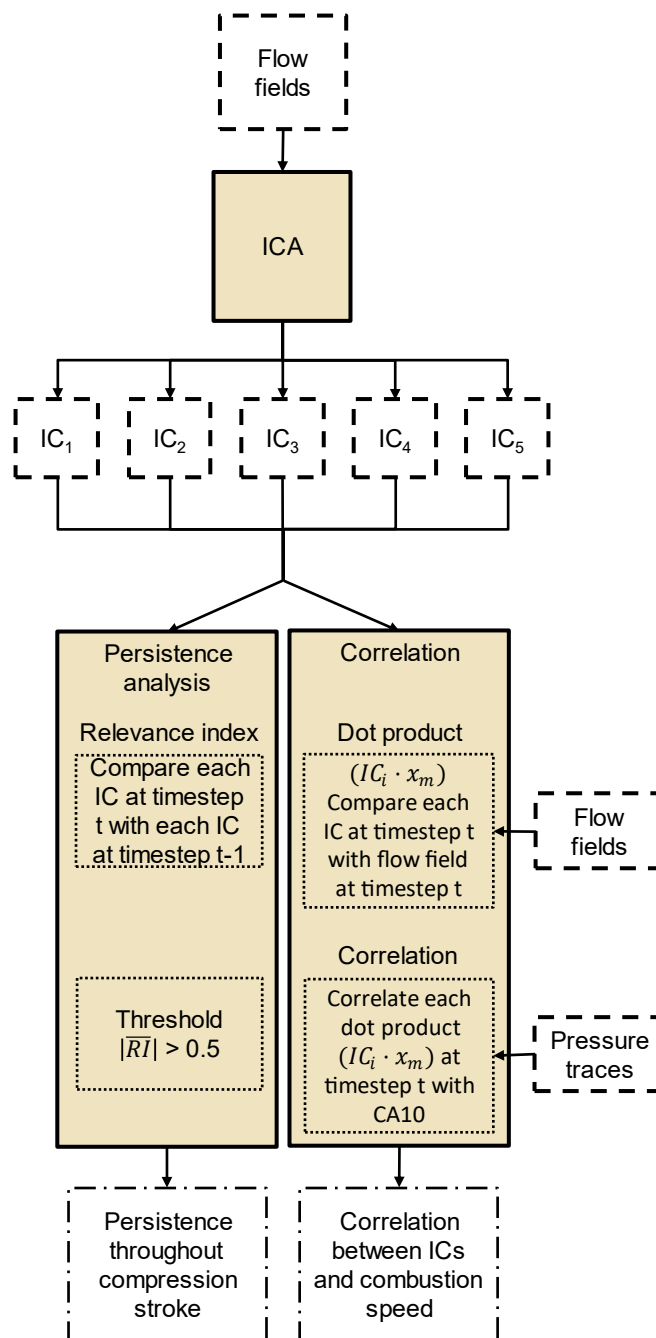


Figure 23. Flow chart of the post-processing of the flow fields.

To identify whether an IC persists throughout the compression stroke, the similarity of pairs of flow fields across time is quantified by the relevance index RI . Liu and Haworth [89] presented this metric:

$$RI = \frac{(\mathbf{f}_A \cdot \mathbf{f}_B)}{|\mathbf{f}_A||\mathbf{f}_B|} \quad (11)$$

where at each point in the flow field $(\mathbf{f}_A \cdot \mathbf{f}_B)$ represents the dot product of the two velocity vectors \mathbf{f}_A and \mathbf{f}_B , and $|f|$ is the magnitude of f . The resulting relevance index varies between -1 and 1, with 1 corresponding to perfect alignment and -1 to anti-polar alignment. Starting at ignition timing, each $IC_{i,t}$ at timestep t is compared with each $IC_{i,t-1}$ at timestep $t-1$, the metric for similarity being the spatial average of \overline{RI} . However, since the polarity of each ICs is random, $\overline{RI} = -1$ indicates similarity as much $\overline{RI} = 1$ does. Hence, the absolute value of $|\overline{RI}|$ is used to identify persistence. An example of such a $|\overline{RI}|$ combination matrix is given in Figure 24. As shown in the top-left table in that figure, the two ICs with the highest $|\overline{RI}|$ are first linked. Here, these are IC_3 at -20°CA ($IC_{3,-20^\circ\text{CA}}$) and IC_1 at -21°CA ($IC_{1,-21^\circ\text{CA}}$). These ICs are now marked as already paired when looking for the best correlation among the remaining pairs of ICs. The algorithm continues with descending $|\overline{RI}|$ (grey, large arrows between tables in Figure 24) until every IC_t has either a predecessor or there is no remaining $|\overline{RI}| > 0.5$. Below this threshold the flow fields are considered not similar.

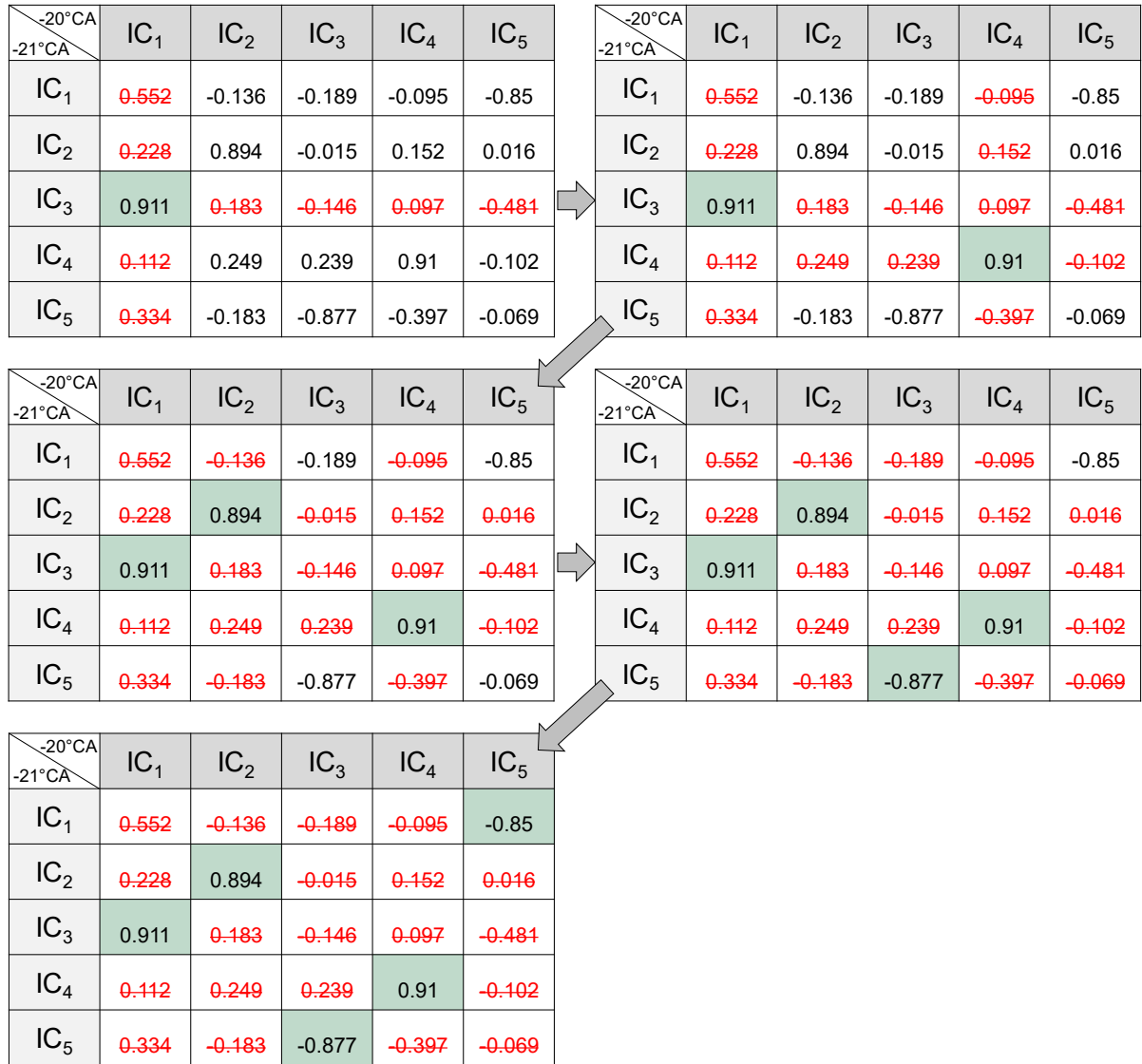


Figure 24. Relevance index for all combinations of ICs at -20°C and -21°C.

The pairing procedure is subsequently executed for the preceding time step (comparing -21°C with -22°C, then -22°C with -23°C, and so on) until no further pairs are detected. This results in five chains of ICs starting at ignition timing back to the crank angle at which no combination of ICs can be found anymore. The table in Figure 25 shows the chain starting back from IC₂ for the first few crank angles. An example is shown at the bottom of the figure.

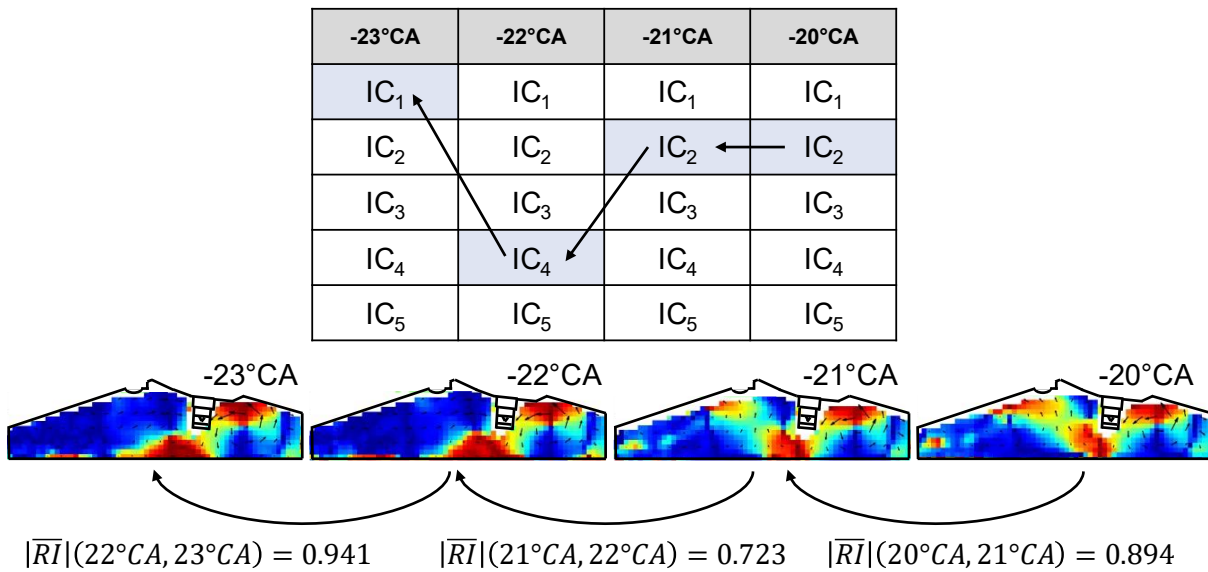


Figure 25. Example of the resulting persistence chain.

Now that the persistent, typical “components” of the flow occurring in the compression stroke are identified, how can it be determined if any of them are “responsible” for a certain outcome of the (cyclically variable) combustion? For that purpose, the link between combustion and flow is analyzed by a correlation between CA10 and the degree to which each flow field contains a specific IC. In the first step, each IC is compared with each flow field for each timestep – by calculating a pair’s dot product ($IC_i \cdot f_m$). Since only one IC is being compared here with a set of flow fields, the magnitude of the respective IC can also be considered. Thereby, regions in the IC with strong flow are given more importance than those with weaker flow. The resulting scalar quantity for each IC and each timestep is then checked for its correlation with CA10. The correlation coefficient R has already been introduced in chapter 3.2.2, equation (9). It is a measure to what extent two parameters are linearly correlated [104]. A potential physical correlation between relevance index (i.e., flow) and CA10 (i.e., combustion) may not necessarily be linear, but later on it will be seen that the scatter in the data does not warrant looking for a higher-order correlation.

4.4 Results

Figure 26 shows the 5 ICs at selected crank angles. Since ICs are inherently unsorted, there is not necessarily (in fact, more likely not) a connection in time between the ICs in a given column. At -90°CA IC₅ shows the tumble vortex with its center on the exhaust side. IC₄ shows a flow field with two vortices, and IC₁ to IC₃ show a flow pattern without dominant vortex. Here, the flow is mostly directed to the piston or the pent-roof. At -60°CA the field of view covers the whole combustion chamber, and in each IC a single vortex is found, but located at different positions. At -40°CA the vortices in each IC remain, but they are decreasing in size due to the compression. Furthermore, the vortex centers are located at different positions. Closer to ignition, at -30°CA , only three ICs contain a vortex. IC₂ contains two flow regions at the spark plug with flow directed against each other, and IC₅ shows a larger-scale flow pattern. At ignition timing at -20°CA , IC₂ to IC₄ have relatively small flow structures and a simple pattern is not

visible. However, IC_1 shows a strong horizontal flow, and IC_5 includes a vortex next to the spark plug.

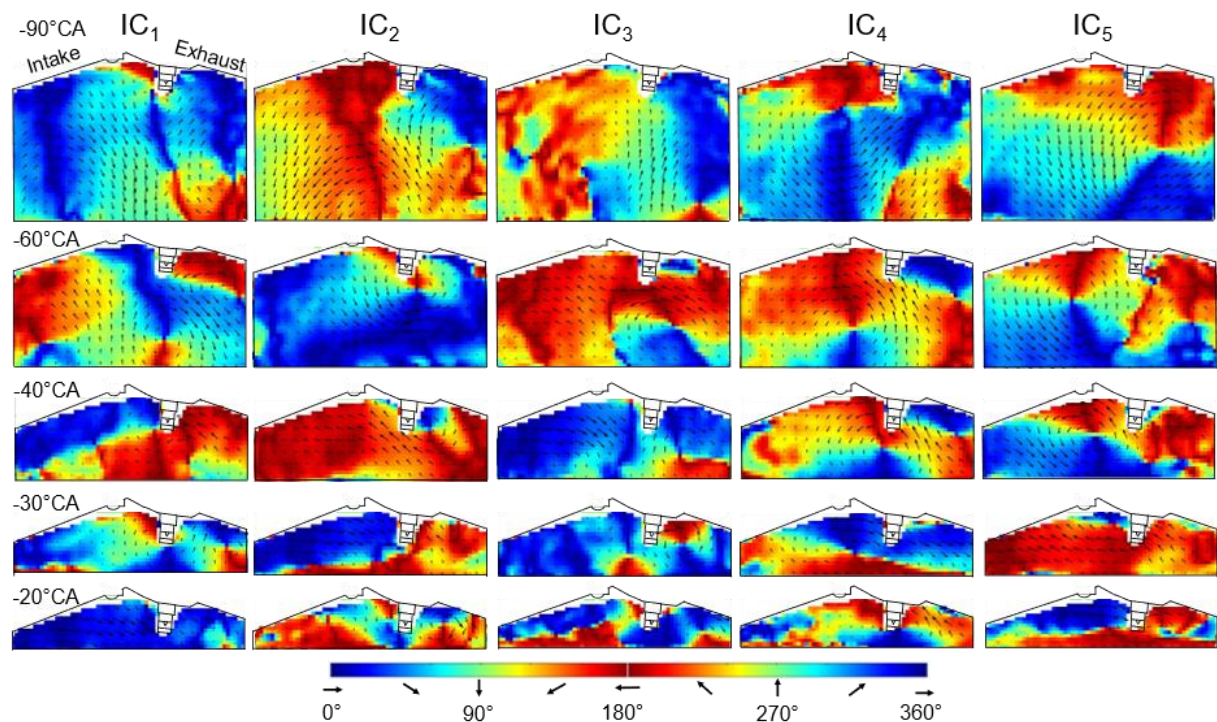


Figure 26. ICs at selected crank angles (not sorted).

To connect the ICs with each other and find flow patterns that persist during the compression stroke, similar flow fields are linked based on their relevance index as described in section 4.3.4. Figure 27 shows the outcome of this persistence analysis, as well as two example ICs. Note that the global polarity of the ICs does not carry any meaning, therefore each temporal sequence is fixed to one polarity. The most persistent IC (IC_1) has high relevance indices not only shortly after ignition and but also between $-40^\circ CA$ and $-55^\circ CA$. However, between $-32^\circ CA$ and $-40^\circ CA$ this IC shows significant changes in its $|\overline{RI}|$. The other ICs only persist from ignition to $-27^\circ CA$ and $-37^\circ CA$. Even though each IC has a different persistence in time, all of the connected ICs show similar drops in their $|\overline{RI}|$, e.g. at $-27^\circ CA$ and $-36^\circ CA$. One reason for these drops may occur due to the formation of new flow patterns. The algorithm compares all ICs from two consecutive time steps and then arranges them based on their highest RI values. If two ICs become more similar over time, for example due to the movement of vortex centers towards the center, and simultaneously new flow patterns occur, only one IC can be associated with the old pattern. The RI will then decrease.

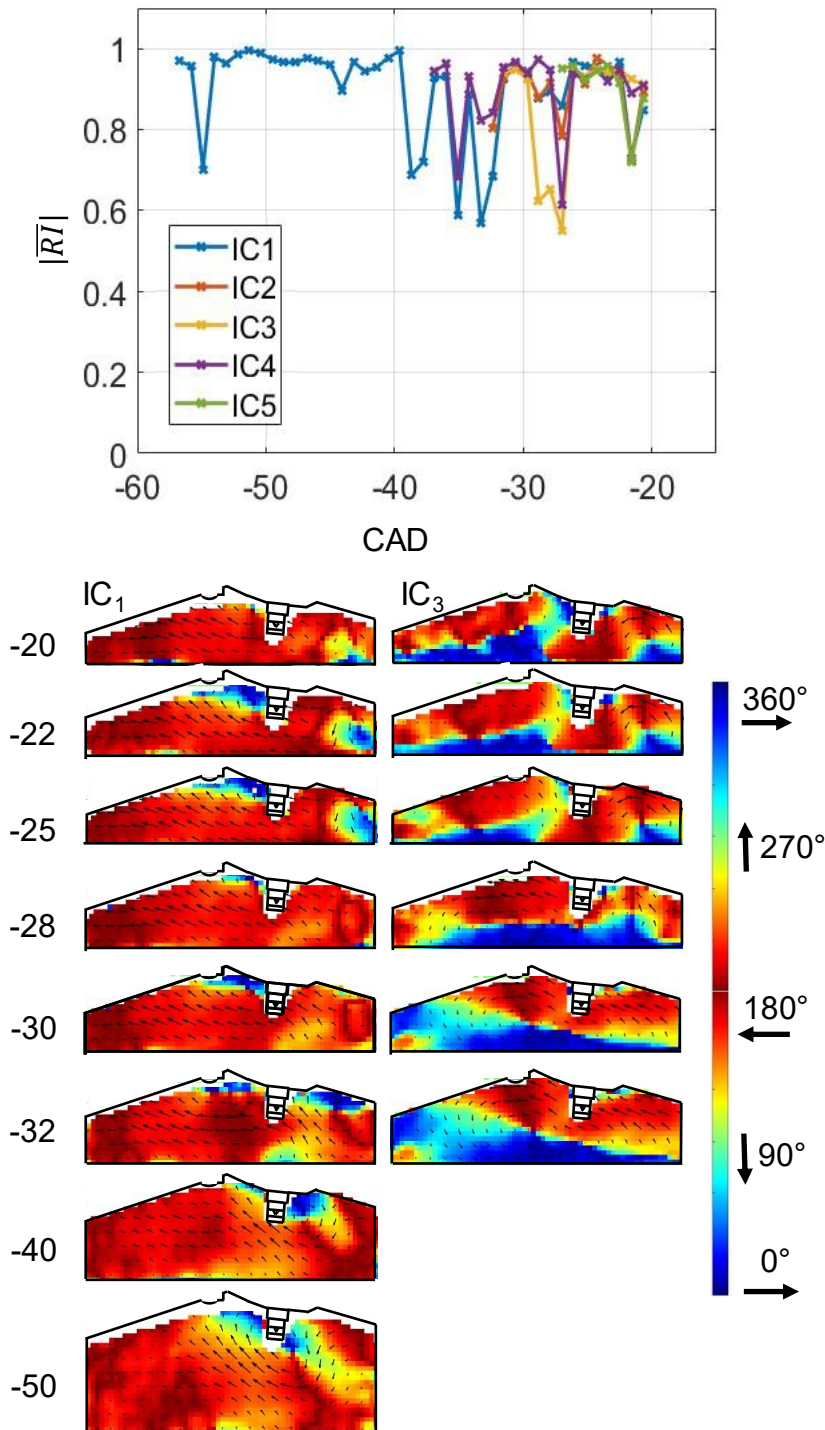


Figure 27. (top) persistence analysis with absolute value of the average RI vs. CAD, (bottom) IC_1 and IC_3 . The sign of the ICs is matched to the initial IC for a better comparison.

The corresponding flow pattern of IC_1 and IC_3 is given on the bottom in Figure 27. The vortex near the spark plug in IC_1 at earlier crank angles gradually disappears and leaves a nearly unidirectional flow from right to left at ignition. The other example IC in Figure 27, IC_3 , is less persistent. At -32°CA it shows a vortex with its center on the intake side next to the spark plug. At -28°CA a second smaller vortex appears on the exhaust side and towards TDC this one becomes more prominent.

Next, to gain information about the relation between the speed of combustion and ICs, each IC is compared to each (moving-average time-filtered) snapshot at the corresponding crank-angle. The resulting dot product indicates how much of an IC is contained within a snapshot. This scalar quantity is then correlated with the pressure-based combustion quantity CA10.

Figure 28a shows examples of the procedure. Since the magnitude is being taken into account by the dot product, color coding and vector length represent that magnitude. The flow field in cycle 7 has a vortex center on the exhaust side close to the pent roof, while the vortex in IC_1 is more centered in the horizontal direction. The dot product of IC_1 and x_7 is only 0.0037, i.e., these two flow fields have very little in common. In cycle 80 the vortex center is more centered horizontally, which better matches the IC with a dot product of -0.1533. However, the faster flow in the IC below the spark plug does not fit with the low velocities in the same region in cycle 80. Among the three example cycles here, the best fit between IC and snapshot has cycle 179. The vortex center is vertically more centered than it is in cycle 80 and that leads to higher velocities below the spark plug. The corresponding dot product is -0.189. Figure 28b shows the correlation of combustion speed and dot product as a scatter plot for the whole data set at -55°CA. In this case, indeed, if much of IC_1 is contained in a snapshot, combustion tends to be faster (earlier CA10) and vice versa. Here, the overall correlation coefficient is 0.438.

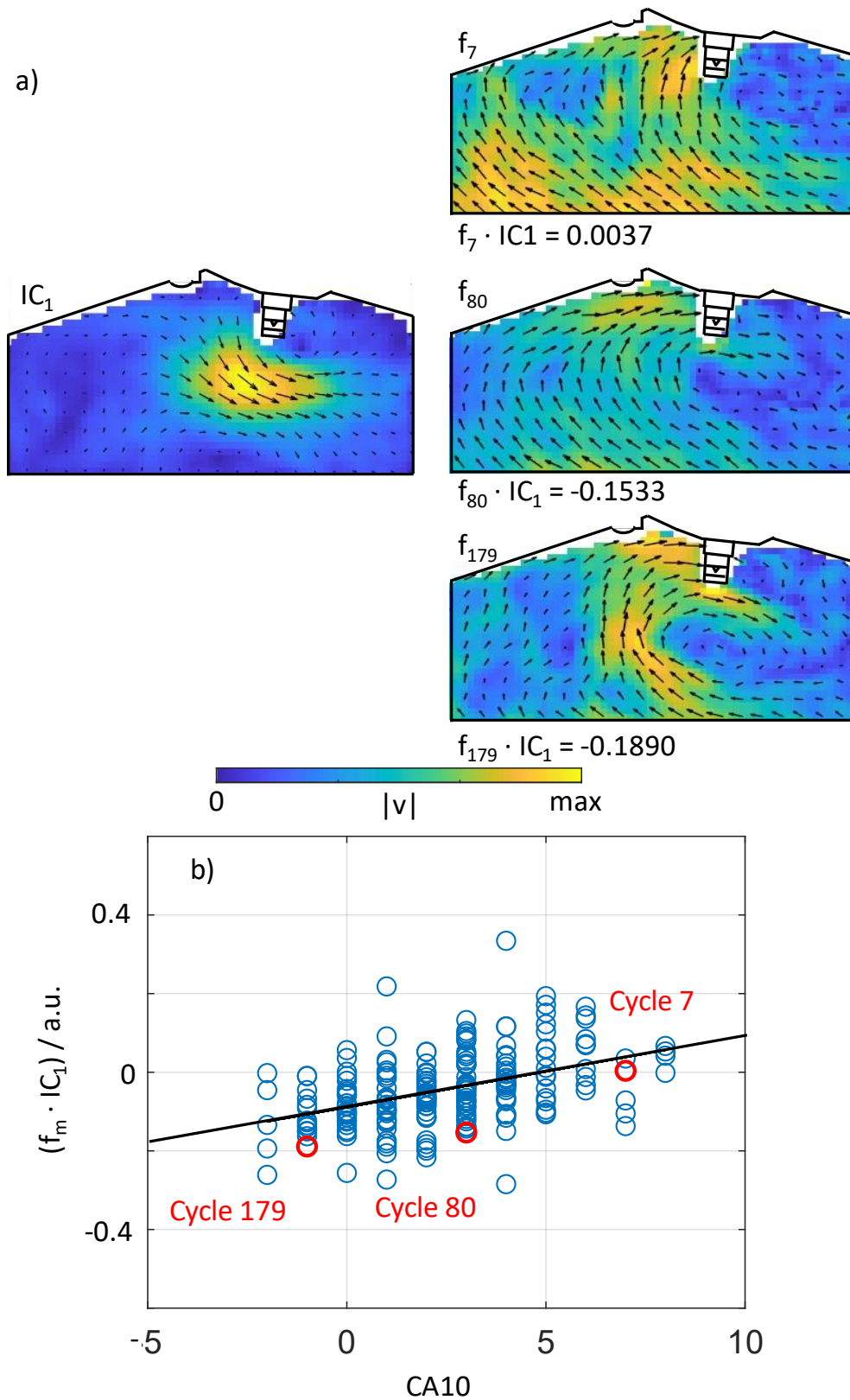


Figure 28. (a) Example of an IC, snapshots, and resulting relevance indexes for selected cycles at -55°CA , (b) corresponding correlation with CA10 over all 213 cycles at -55°CA . The results from the three example snapshots are marked in red.

Figure 29a now combines the persistence analysis from Figure 27 and the correlation analysis from Figure 28. Here, the absolute value of the correlation coefficient $|R|$, representing the degree of correlation between the dot product $(IC_i \cdot f_m)$ and CA10, is plotted vs. CAD. The length of each trace indicates the persistence of an IC while $|R|$ indicates how relevant the IC is for the speed of the subsequent combustion. Tracing the correlation from its individual starting point to ignition, the most persistent IC (IC_1) has a relatively high R -value of 0.48 at -55°CA , slowly decreasing to 0.05 at -30°CA . At ignition (-20°CA) this IC has the second-lowest correlation coefficient. The correlation coefficients of IC_2 and IC_3 are more constant but also low with ~ 0.05 and ~ 0.1 , respectively. IC_5 starts at -28°CA with an R -value of 0.1, increasing to about 0.25 between -25°CA and -22°CA , then decreasing towards ignition to 0.1. IC_4 has the highest R -value and by this metric seems would be an important flow pattern for the combustion speed. This IC is shown in the first column of Figure 29b for different CADs. At -35°CA two vortices dominate and there is just a relatively weak flow on the intake side of the combustion chamber. This flow pattern remains until -27°CA . The vortex center on the exhaust side disappears at -25°CA such that at ignition there is a single vortex around the spark plug with a strong flow towards the piston on the exhaust side.

The prior analysis of the same dataset, which relied on conditional averaging as outlined in chapter 3.3, showed that in the 35 fastest-burning cycles, the pre-combustion flow exhibited a vortex encircling the spark plug, whereas on average a vortex on the exhaust side was linked to slower combustion. The corresponding flow fields are shown in the second (fast) and third (slow) column of Figure 29b. In the present study, IC_4 has the strongest correlation with combustion speed. This IC contains the two vortices, one centered around the spark plug and another on the exhaust side between -35°CA and -27°CA . Towards TDC the IC shows only one vortex centered at the spark plug, which aligns only with the conditional average of the 35 fastest cycles. This suggests that the more important flow pattern influencing combustion involves the vortex center around the spark plug and a strong flow on the exhaust side.

In the first column of Figure 29c the flow pattern of IC_1 at -55°CA , which also correlates well with the combustion speed, is shown. The main feature of IC_1 is a region of strongest lateral flow below the spark plug. In the corresponding conditional averages, the differences between fast and slow cycles are less obvious than in the later stages of flow development. For the slow cycles, the vortex center is on the exhaust side, while for the fast cycles, the vortex center is more horizontally centered. Visually, IC_1 has very little in common with conditional averages or the difference between them. This and the then following steady decline of this ICs correlation with combustion may indicate that IC_1 contains a flow component that is important early on but is then gradually replaced by more than one other component. Some of this energy redistribution may also occur outside of the PIV plane such that it is not detected in the experimental data.

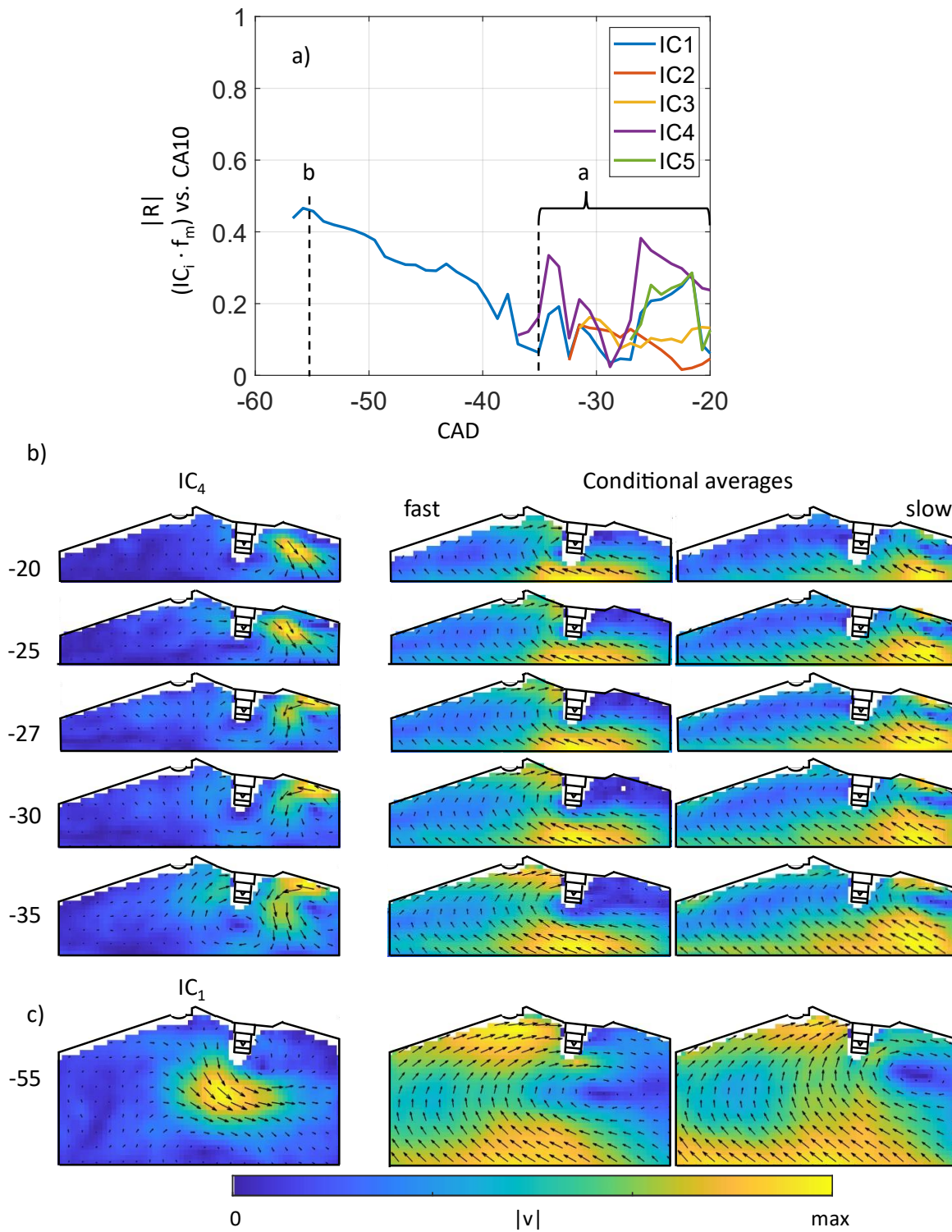


Figure 29. (a) Correlation coefficient of $(IC_i \cdot f_m)$ and CA10 vs. CAD, (b) IC_4 – the IC with the highest correlation coefficient near ignition – and conditionally averaged flow fields at the same crank angles, (c) IC_1 – the most persistent IC – and conditionally averaged flow fields at -55°CA .

4.5 Chapter conclusion

This work focused on identifying links between the flow and the speed of combustion in an optical IC engine operated on a slightly lean homogeneous iso-octane/air mixture. In particular, the goal was to examine if ICA based on vector fields measured with high-speed PIV might provide an objective and quantitative analysis of flow patterns to find such a link. While techniques based on POD had previously been used widely in flow analysis and combustion research, so far ICA had only been applied for a few examples of scalar combustion images [99,101,102]. The expected key difference between POD and ICA was that ICA would produce “source components”, i.e., flow structures that could be linked to other observables, while POD would do this only under exceptional cases, if at all [90].

To test the fundamental procedure, initially ICA is applied to a synthetic example in which the number of underlying sources was known a priori. ICA was then employed to extract flow patterns from high-speed PIV data gathered from 213 engine cycles. In such empirical data, the number of sources is not known. A parameter study suggested that for the current data set five ICs are sufficient. A persistence analysis found that one IC could be traced from -60°CA to ignition at -20°CA , while the other four ICs persisted at the most from -38°CA to ignition. As a metric of the speed of combustion progress, the pressure-based cumulative heat-release, in particular CA10, was utilized. By quantifying the correlation between the similarity of independent components and flow fields and CA10, the relationship between independent components and the speed of combustion is investigated. This examination showed that the combustion relevance of the most persistent IC mostly declines throughout the upper compression stroke, while the IC that correlates best with combustion speed is one of the less persistent ones. The latter also visually more resembles some of the flow features found in conditional averaging of fast-burning vs. slow-burning cycles [74]. The combination of ICA and the current implementation of a persistence analysis does not give a direct indication as to how any presumed underlying re-organization of the flow occurs.

5 Analysis of the mixture distribution in a hydrogen-fueled heavy-duty engine

This chapter is based on LIF measurements carried out at the Combustion Research Facility at Sandia National Laboratories, California. The mixture distribution for different injection strategies under motored operation with H₂ was investigated. The work was mostly published in Laichter et al. [105] and was presented at the SAE World Congress Experience in April 2023.

5.1 State of the art

H₂ is a carbon-free, potentially renewable fuel for ICEs that can supplement fossil fuels in difficult to-electrify applications and in jurisdictions enforcing tail-pipe CO₂ emission legislation. Therefore, H₂-fueled internal combustion engines (H₂-ICEs) are actively being developed by several engine manufacturers with foreseen applications ranging from on-road heavy duty transport, marine propulsion, agriculture, mining, and construction machinery to power generation. In light of short development timeframes, most of these first-generation H₂-ICEs will likely be derivatives of existing diesel or natural-gas fueled engines with fumigation or port-injection of H₂ fuel and a spark-plug or diesel pilot as the ignition source.

The modification of existing engines to DI H₂ fueling is relatively straightforward in terms of hardware modification. However, the low volumetric density of H₂, low minimum ignition energy, and high flame speeds pose a significant challenge in terms of engine power volumetric density, turbocharger matching, pre-ignition, and safety concerns associated with back-fire [106–108]. The advantages of the DI approach are simplicity, low cost, and low NO_x emissions at reasonable efficiency made feasible by the high flame speed of H₂ even at very lean conditions [107,109].

A logical further evolution of the H₂-ICE is direct fuel injection to mitigate power-density, back-fire, and (to a certain extent) pre-ignition [109–111]. The various H₂ direct-injection (H₂-DI) approaches are distinguished primarily by the injector operating pressure: low pressure injectors (typical, 200 bar) feature high operational flexibility and can even enable non-premixed diesel-type H₂ combustion [110,112,113]. However, high injection pressure dictates installation of on-board fuel compressor or requires high residual pressure in empty tank thus reducing the effective capacity of fuel reservoir. The cost, energy expenditure, and technical challenges of high-pressure compressors or cryogenic pumps may hinder adoption of high-pressure H₂-DI in some markets. Therefore, medium-pressure H₂-DI (10-50 bar) may offer a viable compromise in terms of operational flexibility, pre-ignition mitigation, NO_x emission, and complexity of the fuel supply system.

With injection timing during the compression stroke, the combustion in medium-pressure H₂-DI engine concepts typically features flame propagation through a premixed or moderately-stratified charge [49,58,111]. Various ignition concepts are compatible with this operating mode (spark, pre-chamber, diesel pilot). An additional benefit of H₂-DI might be the enhancement of flow and turbulence by the injection induced momentum, thus increasing the

flame speed [58,114]. Some level of fuel stratification may also reduce the engine heat loss [115,116]. However, engine studies featuring H₂-DI typically reported tradeoffs between fuel efficiency, NO_x production, and frequency of pre-ignition [117–120]. Frequently, operating points with rather late injection offered best efficiency but produced excessive amounts of NO (>20 g/kWh NO emission was reported) [118–121]. Therefore, it is useful to understand how various aspects of H₂-DI system design and operation impact the subsequent mixture formation in order to alleviate the above-mentioned trade-offs.

Optical engines and high-pressure vessels are the primary experimental tools available to visualize, characterize, and understand in-cylinder mixing processes. Vessel experiments can show the near nozzle jet structure and evolution [122], as well as the effects of jet-jet interaction on macroscopic evolution of fuel jets. Jet-collapse and jet-wall interactions driven by the Coanda effect affect the trajectory of fuel jets and the global evolution of the mixture [119,123,124]. Multi hole and hollow-cone gas injectors are prone to jet collapse [124,125] which makes jet targeting in engines a challenge and requires large spatial separation between nozzles to avoid collapse when it is undesired. This then may limit the rate of fuel mixing. Research in optical engines has mostly focused on light-duty tumble-supported combustion chambers, including studies of jet evolution, mixture formation, and combustion to understand the impact of mixture and flow on engine performance and emissions. Overall, in most studies the mixture remained stratified with injection during compression stroke [49,52,126,127]. As expected, delayed injection increases the fuel stratification, flow velocities, and turbulence near TDC. The fuel jet strongly interacts with the in-cylinder bulk flow [126]. Fuel stratification, in-cylinder flow, and their repeatability is important for flame evolution, emissions, and CCV [114]. The complexity of these interactions poses a significant challenge for the optimization of injector, combustion chamber geometry and engine operating strategy.

Three-dimensional computational fluid dynamic simulations (CFD) complement experiments and are heavily relied upon for hardware optimization in the industry. The challenges associated with CFD of DI of gaseous fuels originate from fine grid and temporal resolution required to resolve under-expanded jet effects near the nozzle [124,128]. The low density of H₂ results in significant momentum exchange between the jet and surrounding gas even in the under-expanded region near the nozzle [129], therefore, under-resolved simulations and simplified Eulerian-Lagrangian approaches may be inaccurate [130]. Non-ideal gas behavior [131] and lack of established practices and sub models for modelling gaseous-fuel DI and H₂ combustion are also a barrier [128,132]. Sometimes, unconventional model choices/settings and meshing strategies are used to reproduce experimental data from the existing datasets focused on light-duty engines [112,133,134]. While most CFD approaches yield reasonable predictions of H₂ jet penetration and shape during the injection, the long mixing period and associated turbulence dissipation and interaction with in-cylinder flows during the compression stroke pose a particular challenge for accurate prediction of in-cylinder mixture near the TDC [128,133,134]. In particular for large-bore engines, an additional barrier is the lack of suitable validation data acquired with modern injection hardware.

This work addresses two main barriers for further development of large H₂-DI engines: lack of understanding on in-cylinder mixture formation and lack of data for validation of CFD simulations. H₂ mixture formation with a medium-pressure H₂-DI system is studied in a heavy-duty optical engine with a nearly-quiescent low-swirl combustion chamber and a flat cylinder head. Tracer LIF was used to quantify the in-cylinder mixture distribution near the end of compression stroke for a variation of injection timing and injection pressure. Following the description of experimental setup and data processing, first, the early H₂ jet evolution is presented since it is an important process for later mixture formation. Next, the impact of injection timing and injection pressure on single-cycle and ensemble-average in-cylinder mixture distribution around spark-timing is discussed. Finally, a statistical analysis of mixture distribution demonstrates the implications of the tested injection parameters on CCV and NO_x formation.

5.2 Heavy-duty optical engine

The experiments use the Sandia-Cummins single-cylinder heavy-duty optical engine, which is modified from a single-cylinder Cummins N-14 series DI, heavy-duty diesel engine. The optical engine has 139.7 mm bore and 152.4 mm stroke, yielding a displacement of 2.34 L with a base compression ratio of 10.75 in the configuration used here. A schematic layout of the optical engine with the fuel system and the imaging setup is shown in Figure 30; the major specifications of the engine and fuel system are given in Table 6.

The intake port geometry of the production engine, which has a steady-state (i.e., measured on a flow-bench) swirl ratio of 0.5 [135], is preserved in the optical engine. The engine is equipped with a Bowditch piston with an open, right-cylindrical bowl and a flat fused-silica piston-crown window that allows unrestricted optical access to the whole bowl when viewed from below (see schematic in Figure 30). The piston bowl-rim features a 37 mm-wide cut-out of the same depth as the piston bowl to allow optical access into the bowl volume through a cylinder liner window. Additional optical access (not used here) is available through a window replacing an exhaust valve. Further details of this engine can be found elsewhere [136,137].

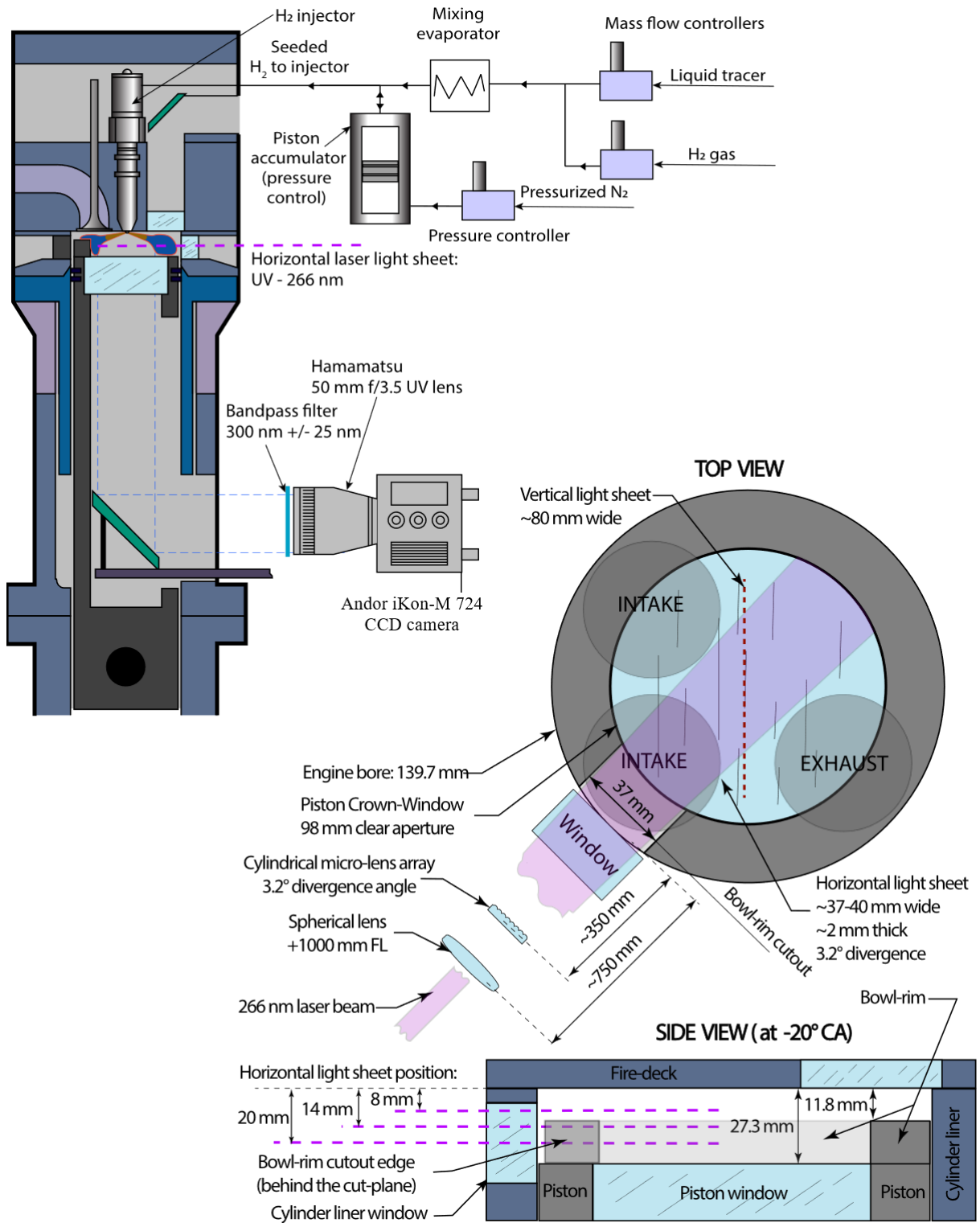


Figure 30. Schematic layout of the optical engine (left) and imaging setup (right).

Table 6. Engine and fuel injector specifications

Engine specifications	
Engine base type	Cummins N-14, DI diesel
Number of cylinders	1
Number of intake valves	2
Number of exhaust valves	1 ¹
Combustion chamber	Quiescent, central direct injection
Swirl ratio	0.5
Bore x stroke [mm]	139.7 x 152.4
Bowl diameter [mm]	97.8
Bowl depth [mm]	15.5
Displacement [liters]	2.34
Connecting rod length [mm]	304.8
Compression ratio	10.75
Direct injector specification	
Injector type	BorgWarner, DI-CHG 10
Maximum flow rate [g/s]	10
Injector design	Solenoid-actuated, outward-opening hollow-cone
Fumigation injector specifications	
Fuel injector type	Solenoid-actuated, Clean Air SP010 PT Gas Injector

5.2.1 Fuel and injection

A Borg-Warner DI-CHG10 medium-pressure outward opening hollow-cone prototype injector was used to inject H₂ directly into the cylinder. A simplified geometry of the flow path in this injector just upstream of the opening is plotted in Figure 31. At an injection pressure of 40 bar, the design steady flow rate for this injector is 10 g/s of H₂. The injected fuel volume was characterized at atmospheric pressure for a range of energizing times and at 40 bar and 20 bar injection pressure – since the pressure-ratio across the needle creates choked flow, the in-cylinder pressure is not expected to impact the injected fuel amount, and the fuel flow-rate is roughly proportional to the injection pressure. The injector is centrally mounted with its major axis aligned with the cylinder axis and the front face flush with the flat cylinder head surface (fire-deck). All injection timings in this work refer to the electronic commands and not the

¹ In this optically accessible diesel engine, one of the two exhaust valves of the production cylinder head is replaced by a window.

physical (“hydraulic”) start of injection, the latter being about 2 to 2.5°CA later, as will be shown in the Results section.

To enable the fluorescence imaging described in the next section, pressurized H₂ gas was seeded with 0.1 volume-% of 1,4-difluoro-benzene (DFB, boiling point 89°C at 1 bar) vapor. The tracer and H₂ streams with precisely controlled flowrates were mixed at a reduced pressure of 5 bar by a Bronkhorst Controlled Evaporator-Mixer system (CEM, model W-303A). This DFB-seeded H₂ stream filled a piston accumulator with 6 L displacement. Once full, the seeded H₂ gas was compressed by pressurized nitrogen in the other cavity of the piston accumulator. A piston with Kalrez seals prevented the two gases from mixing. The nitrogen pressure was controlled by a pressure controller (Tescom ER5000 actuating a dome-loaded regulator) to ensure repeatable injection pressure. Each batch of seeded H₂ was sufficient for about 60 fuel injections.

To ensure a homogenous mixture in the reference images used for correction of brightness variation across the light sheet, camera lens vignetting and other effects impacting the white field, DFB-seeded H₂ was mixed into the intake runner flow about 0.55 m from the cylinder head intake port with a fumigation injection. Therefore, a single-hole 8 bar pressure H₂ injector (Clean Air Power SP-010 PT) supplied seeded H₂ into a perforated annular tube embedded in the intake air stream to create a well-mixed tracer/H₂/air mixture in the intake. This injector was only used for the reference images (white field correction), while the measurements of the mixture formation were performed with DI only.

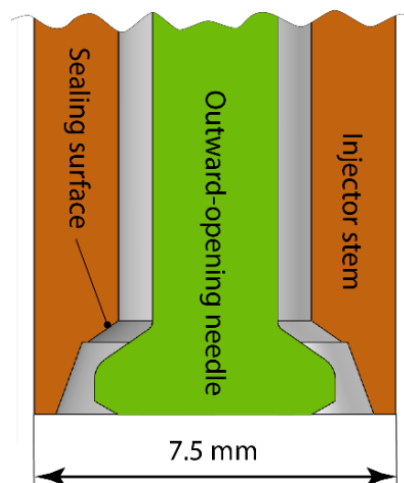


Figure 31. Approximate H₂-DI injector geometry (the exact geometries of needle and injector stem are proprietary).

5.2.2 Tracer LIF imaging

LIF imaging of a “tracer” added to the fuel was used to quantify in-cylinder H₂ mixture formation. Two imaging arrangements were used, one with a horizontal laser sheet (parallel to the cylinder head) and one with a vertical one. Figure 30 presents the imaging configurations and Figure 32 shows the relevant spectral features of the tracer and imaging system. Tracer

fluorescence was excited by an Nd:YAG laser (Spectra Physics GCR-270) with a wavelength of 266 nm. The laser was synchronized phase-locked with the engine. A roughly 2 mm thick light sheet was formed by a spherical lens (+1000 mm focal length) and a cylindrical micro-lens array (Edmunds, #86-844). For horizontal plane imaging, the sheet entered the combustion chamber parallel to the cylinder head through a cylinder-liner window and the 37 mm wide cutout in the bowl-rim. As indicated in Figure 30, the sheet was slightly diverging in the transverse direction. The pulse-energy of the light sheet within the combustion chamber was about 28 mJ/pulse. At this laser fluence of about 40 mJ/cm², the fluorescence intensity is in good approximation linear in laser energy [138,139]. Images were acquired in three horizontal planes, 8, 14, and 20 mm below the fire deck. A fast photo diode (Thorlabs DET10A) connected to a boxcar integrator (SRS SR250) measured the energy of each laser shot.

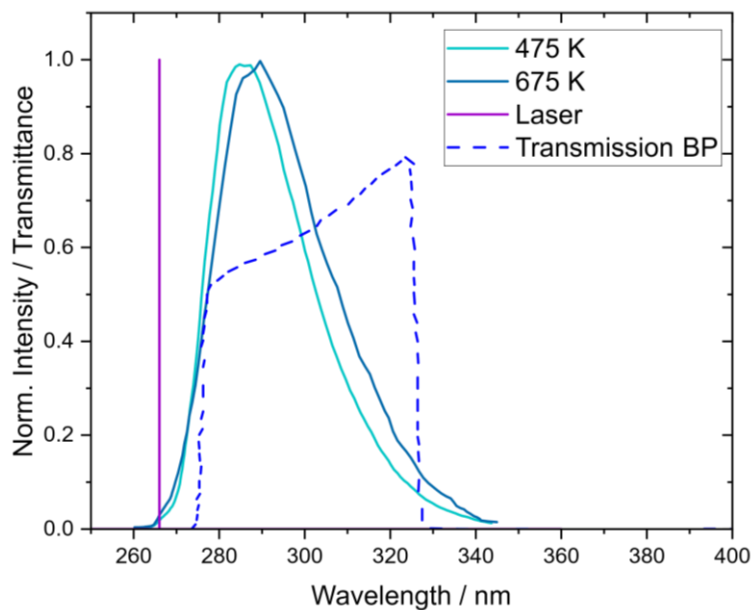


Figure 32. Peak-normalized *p*-DFB fluorescence spectra at 475 K and 675 K in 1 bar N₂ bath extracted from [59], transmittance of the used filter and laser wavelength.

The tracer fluorescence was imaged through the piston-crown window by a non-intensified UV-sensitive CCD camera (Andor Instruments iKon-M 724, sensor BU2) equipped with a Hamamatsu 50 mm f/3.5 UV lens and a 300±25 nm bandpass filter (Edmunds #12-097). The camera was exposed for 20 ms due to the limitation of mechanical shutter and operated with 2x2 binning, resulting in projected pixel size of about 0.2 mm/pixel. A non-intensified CCD camera was preferred over an intensified one for its better linearity, signal-to-noise ratio, and resolution [140]. Despite the long camera exposure time, the effective exposure is determined by the laser pulse duration (~5 - 8 ns) and tracer fluorescence lifetime (1 - 10 ns, temperature dependent, [138]).

The second imaging arrangement featured a vertical light sheet that entered the combustion chamber through the piston-crown window. The light sheet was aligned with the injector axis to dissect the combustion chamber in half. Its orientation is marked in Figure 30 (top-view schematic). The light sheet was formed using the same optical elements as for the horizontal

sheet. Here, a different arrangement of the optical elements resulted in an 80 mm wide and 1 mm thick sheet. The bowl-rim was rotated by 135° counter-clockwise to align with a larger cylinder-liner window (not shown in Figure 30) on the right of the combustion chamber. The same hardware was used to image the fluorescence through this 50 mm wide and 30 mm high cylinder-liner window, resulting in projected pixel size of 0.135 mm/pixel.

5.2.3 Engine operating conditions and measurements

The optical engine was motored at 1200 rpm and operated in a “9:1 skip-fire” mode, meaning that 9 cycles without fuel injection preceded every cycle with fuel injection. The engine was supplied with neat nitrogen heated to 62°C at a flow rate of 22 g/s for an intake pressure of 100 kPa. The engine oil and coolant temperature were maintained at 90°C and the charge temperature at BDC is estimated at about 356 K based on previous experience. Each experimental test run consisted of 60 cycles with fuel injection and one LIF image was acquired per fuel injection for a total of 60 images per run. Also, 60 background images were acquired per engine run in-between the cycles with fuel injection, by firing the laser but not injecting any fuel. For each fixed imaging crank-angle, a set of 60 reference images with well-mixed charge were acquired at the same crank-angle in a separate engine run. The engine encoder has a resolution of 0.25°CA. The experimental conditions are summarized in Table 7, and Figure 33 shows mean pressure and adiabatic temperature traces with some of the relevant events indicated.

The focus of this work was to study the effect of injection timing and injection pressure on in-cylinder mixture formation. Therefore, five injection timings and two injection pressures were probed in terms of in-cylinder mixture distribution at different times in the cycle as shown in Table 7 and visualized in Figure 33 along with the in-cylinder pressure and temperature evolution assuming adiabatic compression and $T_{BDC} = 356$ K. The injection timings were clustered during the early and intermediate compression stroke to cover the operating envelope of medium-pressure H₂-DI engines, with one timing during the intake stroke (-340°CA) serving as reference. The injector was operated with energizing times that kept the injected amount constant at 21.6 mg/cycle for both injection pressures. This injected mass would yield a global equivalence ratio of $\phi = 0.33$ if the engine intake were supplied with air instead of nitrogen. In homogeneous, fired operation (not reported here, but in chapter 6), this yielded about 4 bar IMEP, i.e., a low load. The imaging timings were clustered around the typical spark timings in SI engines (40 to 10°CA). For horizontal-plane imaging, one engine run was performed for each combination of experimental parameters – injection pressure (P_{inj}), start of injection (SOI), and imaging timing. With the vertical light sheet, 6 imaging timings were lumped into a single engine run by staggering the laser and camera timing within a run, yielding 10 LIF images for each parameter combination. Vertical images were taken mostly at the same crank angles as the horizontal ones, i.e., during late compression. Additionally, for each SOI setting, series of images were taken with 0.5°CA increments just after SOI to investigate the jet behavior during early injection.

Table 7. Experimental conditions and test case specifications.

Experimental Conditions						
Intake temperature [°C]	62					
Nitrogen flow rate [g/s]	22					
Engine speed [min^{-1}]	1200					
Intake pressure [kPa]	100					
Injected H ₂ mass [mg/cycle]	21.6					
DI fuel injection parameters						
Start of injection [°CA]	-340	-180	-120	-90	-60	
Fuel pressure - P_{inj} [-]	high			low		
Injection duration [ms / °CA]	2.37 / 17			4.40 / 31.7		
Imaging timing						
Horizontal light sheet [°CA]	-40	-30	-20	-10		
Vertical light sheet [°CA]	-60	-50	-40	-30	-20	-10
Vertical light sheet – imaging of early injection [°CA]	From SOI +2.5 in 0.5°CA increments					

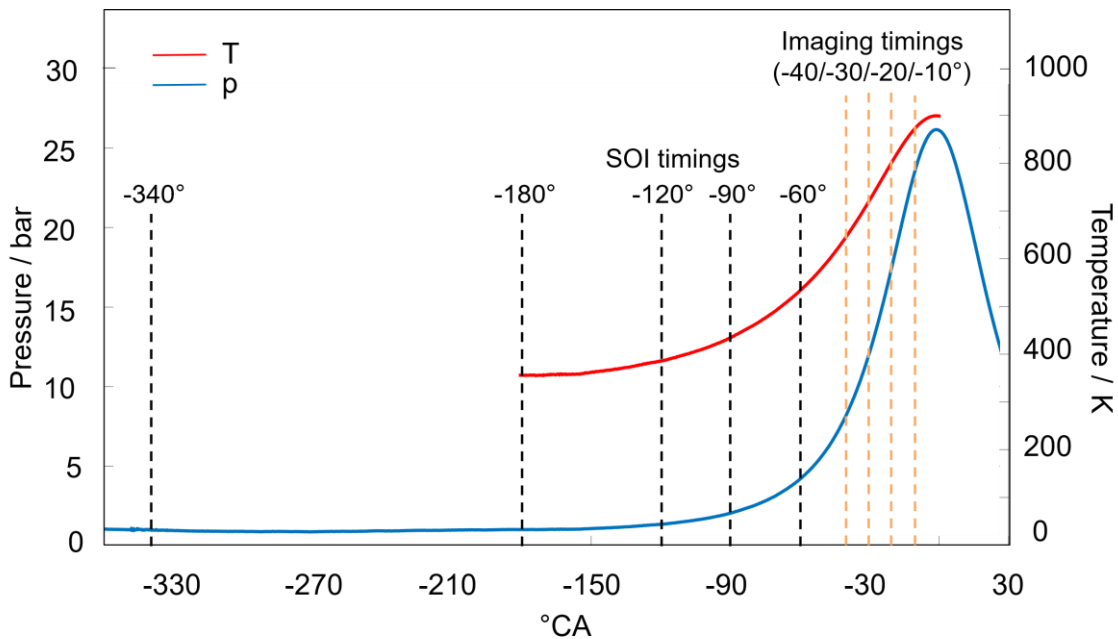


Figure 33. Mean measured pressure trace and calculated adiabatic temperature for the reference case with homogeneous fueling. Also shown are the SOIs and imaging timings.

5.2.4 Data processing and uncertainties

The single-shot laser energy measurement was used to correct the LIF images for shot-to-shot fluctuations. Afterwards, the ensemble-averaged background was subtracted. The micro-lens

array used here provides a globally more homogenous light sheet but creates small-scale transverse structure in the sheet, resulting in fine stripes in the images. To eliminate these, the images were filtered in the frequency domain by applying a mask that suppresses the frequencies corresponding to the stripe pattern. The effect of the Fourier filtering on images is demonstrated in Figure 34.

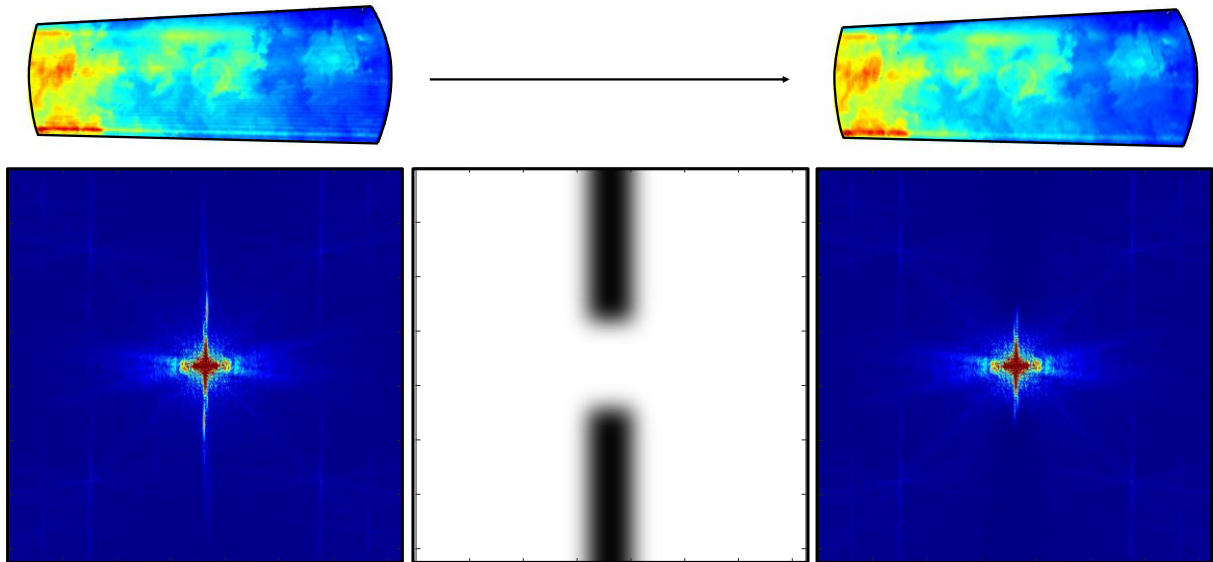


Figure 34. Fourier filtering applied to a sample single-short tracer-LIF image.

The filtered images were divided by the (also filtered) ensemble-averaged homogenous reference images and multiplied by the nominal equivalence ratio ($\phi=0.33$) to yield quantitative images.

Recording the reference images at the same crank angle as the DI images takes into account the global pressure and temperature dependency of the tracer fluorescence. The latter is not as drastic for DFB as it is for example for toluene, but still quite pronounced. Over the entire temperature range encountered in intake and compression stroke – roughly 300 to 900 K – the spectroscopic measurements by Benzler et al. [138] indicate that the signal decreases by a factor of 90 on a per-volume basis, although the concurrent 10-fold increase in density due to compression mitigates this correspondingly. In the current measurements, at -30°CA the adiabatic-compression temperature is about 720 K. At that temperature and 8 bar (a total pressure for which data is available), the LIF signal has a temperature sensitivity of 19 % per 25 K, a span that may be a reasonable estimate for typical mixing-induced temperature inhomogeneity in these measurements at late crank-angles (see discussion in the section Results). Since the field-wide division by the homogeneous reference images does not take temperature inhomogeneity into account, the temperature dependency of the tracer fluorescence results in 19% typical uncertainty in the measured local equivalence ratio. However, for late injection or images during the injection event, much more inhomogeneity and therefore greater uncertainties are encountered.

An additional effect associated with the tracer temperature sensitivity that is not corrected in the present work is associated with the global temperature change due to the direct injection. The DI changes in-cylinder flow and therefore, the heat transfer to the wall. Depending on the injection timing, the gross effect can result in higher charge temperature for injections during the intake stroke (intake air is colder than cylinder walls) or a cooling effect for late injections. Additionally, adding about 9% of volume through H₂ injection after the intake valve closing (IVC) compresses the in-cylinder charge and results in change of global charge temperature – this effect is further amplified by compression. A thermodynamic analysis shows the DI at -180°CA increases the charge temperature at -20°CA from 780 K to 802 K, while in case of injection at -60°CA the charge cools by 12 K. The effect at intermediate injection timings is weaker, while the impact for injection at -340°CA cannot be reliably estimated by comparison to motoring pressure.

Similarly, absorption of the laser within the FOV is only taken into account to first order by acquiring the reference images at the same global equivalence ratio ($\phi = 0.33$) as the DI images. In regions that are “downstream” (in the direction of laser beam travel) of a region with $\phi > 0.33$ the incident laser intensity is lower than in the reference image, yielding an underestimate of the local equivalence ratio, and vice versa. It is difficult to give a typical value for the associated error. Nevertheless, the absorbance in the homogeneous reference images implies that at -20°CA a 10 mm long region of $\phi = 0.66$ attenuates a ray passing through it by 6.5% more than it is attenuated in the reference image at $\phi = 0.33$.

Finally, the reference image set is taken in a different engine run and with different “batch” of fuel/tracer mixture in the piston accumulator. The repeatability uncertainty associated with that is estimated to be 15%.

5.3 Results

5.3.1 Initial jet evolution

To gain insight on the near-nozzle features of the jet, and in particular the jet’s early evolution, Figure 35 shows LIF images of the jet dissected along the injector axis, mostly acquired during the injection event at 40 bar injection pressure. The bottom-row images are taken with 20 bar injection pressure. All images are background, and flat-field corrected, but not FFT filtered nor fully quantified in terms of equivalence ratio. Since the DFB fluorescence signal strongly depends on temperature and pressure, the highly compressible flow and the high local fuel concentrations make quantification inaccurate with the current imaging technique. Instead, each image is normalized near its own maximum “equivalence ratio” so that the relevant features can be discerned in all images. Note that the images in a crank-angle sequence are not from a single cycle.

We first consider the image sequence for SOI = -180°CA. The jet first becomes visible 2.5°CA after nominal, electronic SOI (-177.5°CA), showing a symmetric annular pattern consistent with the outward-opening needle design, without fuel in the center. 0.5°CA later, at -177.0°CA, the jet still resembles a hollow cone, but the next image at -176.5°CA shows the jet collapsed

from about 6 mm downstream of the injector. Based on ensemble-mean images (not shown here), the speed of the tip is estimated to 145 m/s.

The area immediately downstream of the pintle (see injector geometry in Figure 31) is not completely dark but appears to have received some fuel from bluff-body recirculation. Already in this image, but much clearer at -176.0°CA , a pattern of alternating bright-dark areas along the outer edge of the jet (i.e., in the annular high-speed flow) is seen. The dark areas do not necessarily represent lower fuel concentration, since also temperature, and to a lesser extent pressure all significantly influence the LIF signal of DFB [138]. This pattern is interpreted to be the multiple barrel-shock structure of the under-expanded annular jet exiting the nozzle. At early injection timings (-340°CA and -180°CA SOI), the ratio of nominal injection pressure to in-cylinder pressure is 40. About three shock cells can be discerned, each axially and radially growing with time. This is a first indication that the underexpanded flow pattern from hollow-cone injection does not follow the same trends as reported in literature for nozzle flow – at pressure-ratio $p_0/p_{\text{cyl}} > 7$ only a single Mach disk is expected for round nozzles [141].

The entire near-nozzle region appears less bright now than at earlier image timings, and also than the tip of the jet. Again, this probably does not indicate lower equivalence ratio, but is likely due to absorption of the laser beam by the ever increasing amount of tracer-doped fuel below the field of view, from where the laser is incident.

At -176.0°CA the shock structure fades into the onset of turbulent mixing 10 mm below of the nozzle. Downstream of that, the typical scalar structure of a free turbulent jet with its shear-aligned high-gradient regions and the often sharp edges towards the surrounding gas can be seen. The last image in this column is taken much later, at -166°CA , when the injection is expected to be in its quasi-steady phase. It is noisier (i.e., less bright before normalization) than the previous images because of the aforementioned laser absorption below. Nevertheless, this image reveals that in fact at -175.5°CA the near-nozzle region had already nearly reached steady state. However, turbulent mixing now seems to start a bit further upstream than it did at -175.5°CA .

For SOI = -340 the development of the injection jet is very similar to the -180°CA case, as expected from the nearly identical cylinder pressure. The fuel impinges on the piston just after -336.5°CA , which eventually leads to outer recirculation via the walls of the piston bowl (outside of the field of view) and re-entrainment of fuel/air mixture by the jet.

Next, the trends in the phenomena seen in the images are considered with the variation in SOI, whose main effect on the injection jet is the accompanying increase in in-cylinder pressure and gas density, and decrease in nominal total pressure ratio. The jet tip penetration speed in the first one degree crank angle after jet emergence decreases from 145 to 117, 106, and 77 m/s with SOI delayed from -180 to -120 , -90 , and -60°CA . The jet tip becomes somewhat broader, as expected from the increased ambient gas density. In all cases the initially annular jet collapses onto the central injector axis within 1°CA . As expected from the decreasing pressure ratio [19, 40], the shock cells become both shorter and narrower. The number of discernible cells remains

about three (this is hard to see in the figure as reproduced here). However, for $\text{SOI} = -60^\circ\text{CA}$, a shock structure is never established, indicating that the flow is subsonic. Since the nominal total pressure ratio for an in-cylinder pressure of 4.7 bar is 8.5, which should still yield a highly underexpanded jet, this again indicates different trends in formation of shocks compared to round nozzles. Also, the tracer-LIF methodology may not be sensitive enough to reveal weaker diamond shocks if they exist.

Finally, the last row in Figure 5 shows snapshots during the quasi-steady phase for the lower injection pressure, 20 bar. The overall appearance of the jet is very similar for the two injection pressures, including the collapse of the annular jet onto the injector axis just 10 mm downstream of the nozzle exit. At each SOI the images for 20 bar show a smaller shock structure than the corresponding images for 40 bar. This is consistent with the trend in SOI discussed above, because there it was seen that lower pressure ratios yield smaller shock patterns, and the nominal pressure ratio is now half of what it is for 40 bar injection pressure. Also, now already for an $\text{SOI} = -90^\circ\text{CA}$ no shock pattern can be seen. For completeness, crank-angle sequences of the early jet development for 20 bar injection pressure, as in the first 5 rows of Figure 35 for 40 bar, can be found in Figure 51 in the Appendix. The trends there are as expected: slower jet tip penetration than for 40 bar injection pressure, and a further decrease in speed at later injection timings. Figure 51 shows that also for 20 bar injection pressure, the jet collapse is complete 1°CA after the jet emerges from the nozzle.

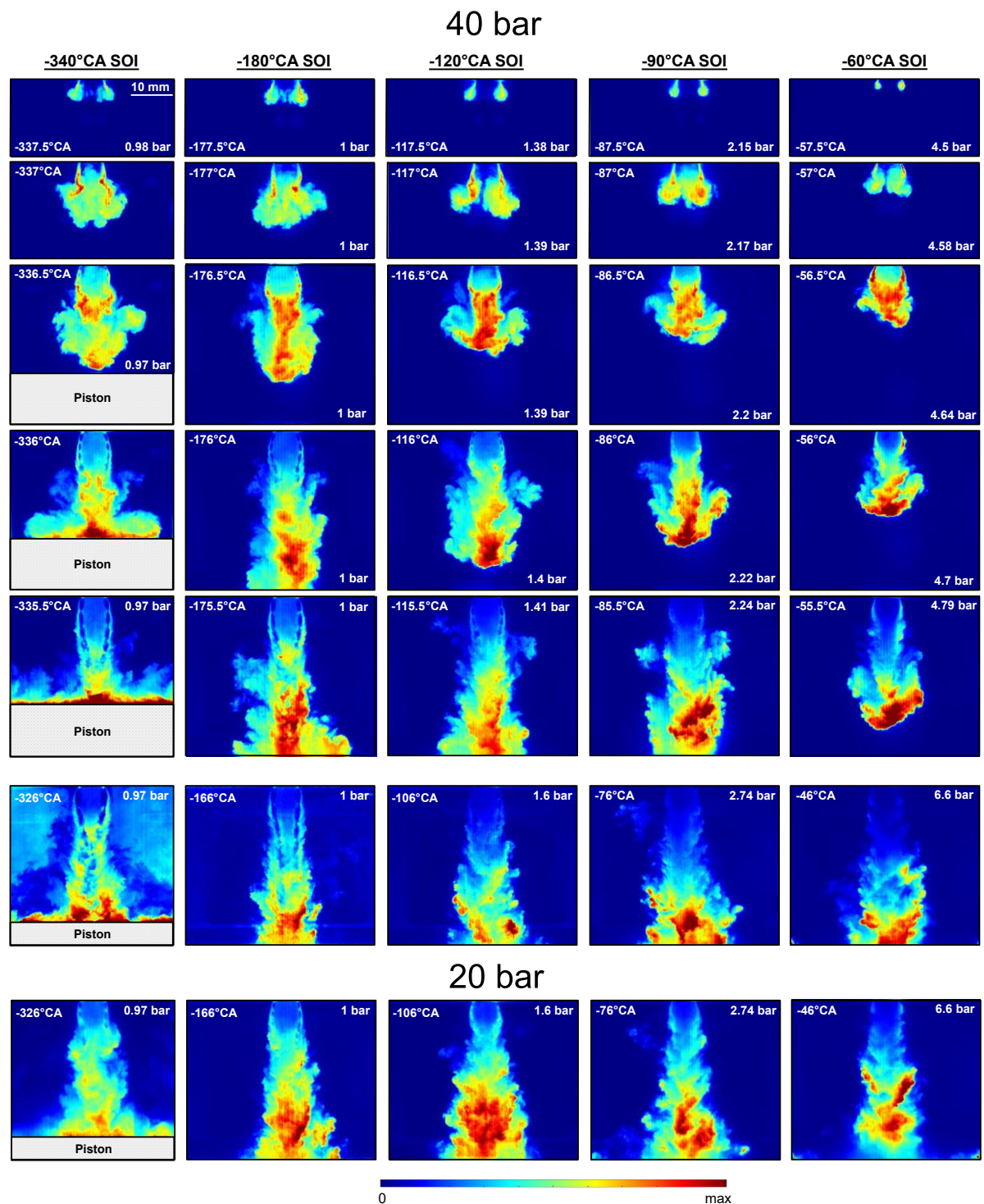


Figure 35. Qualitative single shots of the equivalence ratio in the vertical plane during the injection event for different injection timings with 40 bar (top 6 rows) and 20 bar (bottom row) injection pressure. The top 5 rows show the early injection while the images in the two bottom rows were taken halfway through the injection event in the “quasi-steady” phase. Note that each image is from a different cycle. Each image is normalized at roughly its own maximum intensity value. For each image, crank angle and measured in-cylinder pressure are given.

5.3.2 *In-cylinder mixture distribution*

The early injection timings were studied to gain insights on the mixture homogeneity compared to the homogeneous reference case and to provide an indication of an early enough DI which can be used as a homogeneous reference case in future studies. Figure 36 shows the -340°CA and -180°CA injection timing for 40 bar (top) and 20 bar (bottom) injection pressure. The single shots for -340°CA SOI reveal a fairly homogeneous mixture around the global value of $\phi = 0.33$. The smaller scale variations visible within the imaging plane may be due to the temperature stratification in addition to stratification of mixture [142,143]. In addition, the local equivalence ratio standard deviation from ensemble average is only about 0.02. In the ensemble averaged images, the mixture distribution within each plane is homogeneous. However, there are global differences between the imaging timings and imaging planes, with the mean ϕ on individual planes deviating by up to 10% from global mean. This is likely associated with quantification uncertainty rather than with a physical change of equivalence ratio, especially considering the low standard deviation in each individual plane and at each image timing. Any inconsistency in preparation of tracer- H_2 mixture batches would be reflected in a shift in reported global equivalence ratio, which also applies to the fully homogeneous reference measurements.

For $\text{SOI} = -180^{\circ}\text{CA}$, the single shots (Figure 36, top-right) show increased mixture variability with the local equivalence ratio spanning values from $\phi = 0.15$ to 0.45. While in the individual shots the mixture in the 8 mm plane seems to be randomly distributed, the 20 mm plane shows systematically more fuel on the intake side of FOV (e.g. bottom-left part of individual image panels, see Figure 36). Some of the ensemble mean images, but surprisingly more so at 8 mm than at 20 mm, also show this. With about 0.06, higher near the edges of the bowl, the standard deviation in ϕ is more than twice as high as it is for $\text{SOI} = -340^{\circ}\text{CA}$. This significant CCV in the mixture is relevant from two aspects: higher CCV of combustion and increased NO_x formation are likely, the former will be investigated in chapter 6. Despite the on average homogeneous mixture, using this DI scheme as a homogeneous reference case might introduce systematic experimental errors. The mean ϕ at -180°CA SOI appears leaner than with the earlier injection. This is attributed to the early injection after IVC, which increased the global temperature at imaging timing by about 22 K relative to the homogenous reference case, as discussed in chapter 5.2.4.

Next, the same injection timings are analyzed at the reduced injection pressure of 20 bar (Figure 36, bottom). Since the differences between imaging planes are not significant, only the plane 20 mm below fire deck is shown. With -340°CA SOI, the ensemble mean closely resembles that for 40 bar injection pressure: a homogenous mixture becoming slightly leaner towards TDC, and low standard deviation. With -180°CA SOI, some inhomogeneity with richer mixture near intake is noticeable, similarly to the 8 mm plane with 40 bar injection pressure, but more pronounced. The CCV is higher at lower injection pressure and reaches a standard deviation of 0.1 near the exhaust side of combustion chamber. However, this variability is decreasing at later imaging timing, showing the ongoing mixing process.

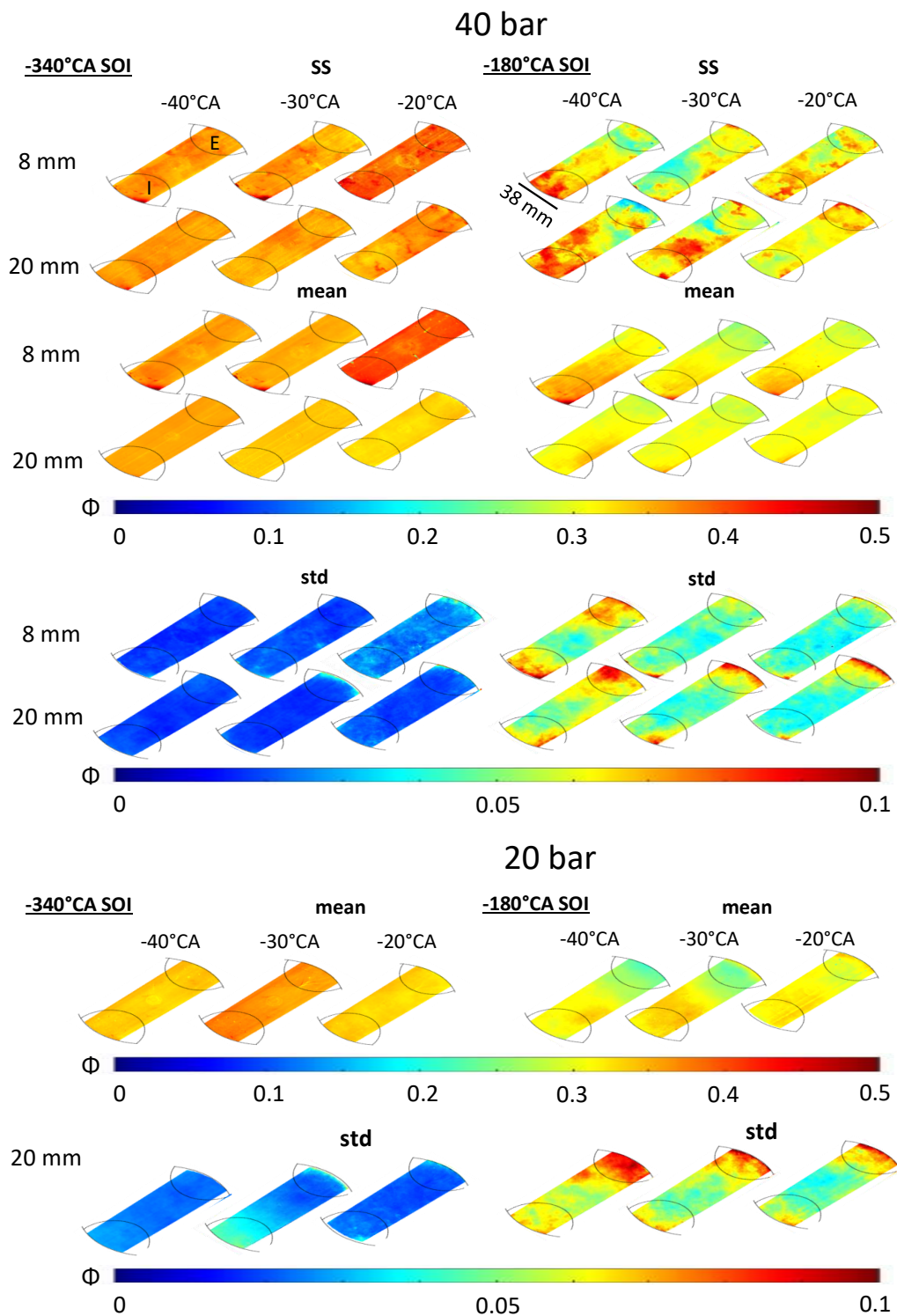


Figure 36. (Top) Single shots, ensemble mean, and standard deviation of the equivalence ratio at two different heights for OPs with -340°CA and -180°CA SOI and 40 bar injection pressure. (Bottom) ensemble-mean equivalence ratio and standard deviation for the corresponding injection timings with 20 bar injection pressure 20 mm below fire deck. Each image panel shows the entire FOV within the 98 mm piston bowl. The light sheet is about 37 mm wide. “I” and “E” indicate the intake and exhaust side of combustion chamber, respectively. Note that different parts of the figure may use different color plotting limits, as indicated on the right.

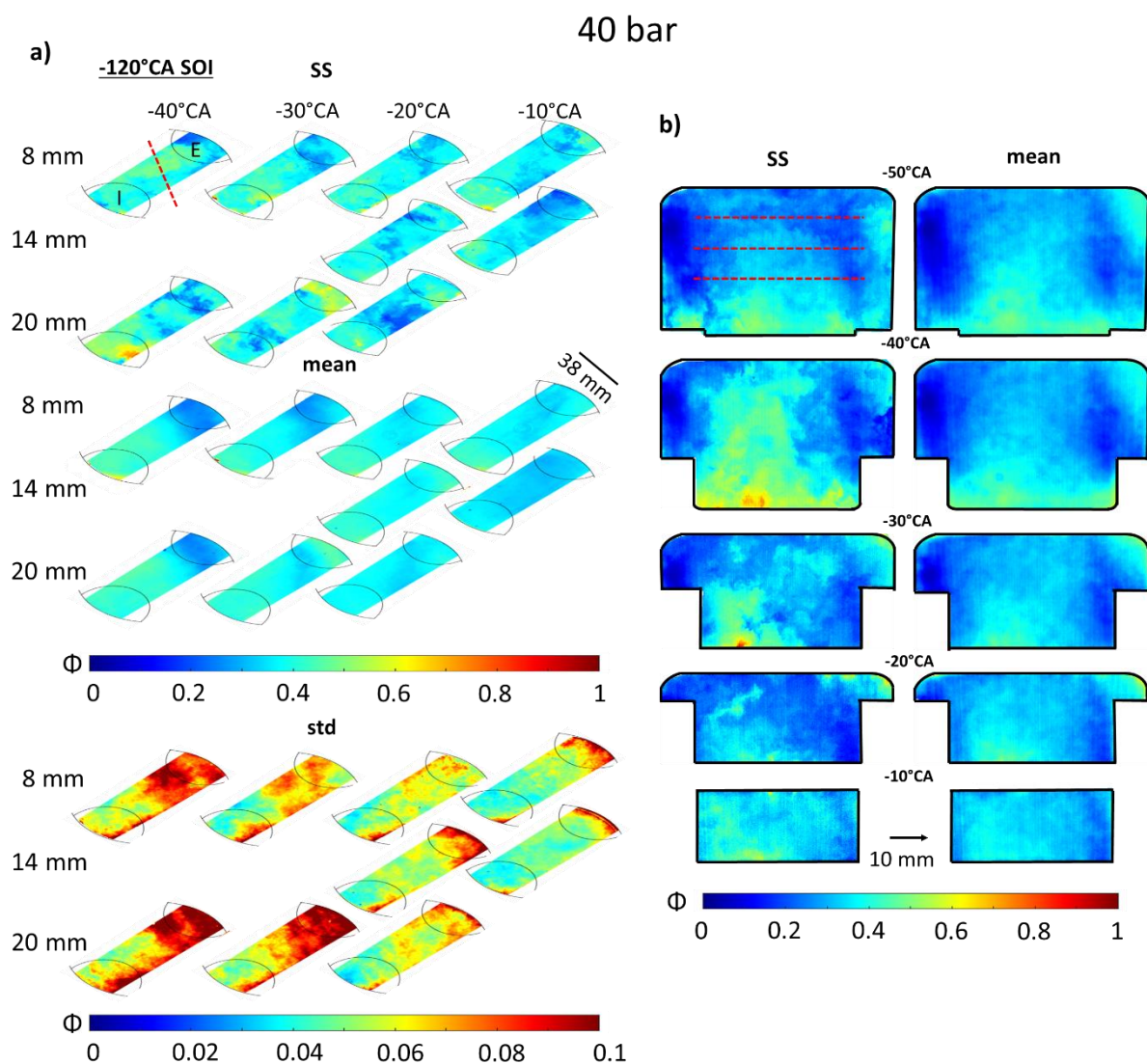
Figure 37 shows the mixture distribution for intermediate SOI at -120°CA and -90°CA with 40 bar injection pressure. In addition to horizontal-plane data, the vertical-plane single-shot and average mixture field is shown to help the interpretation. For SOI = -120°CA (Figure 37a), horizontal single-shots show even higher small-scale inhomogeneity than for -180°CA SOI. The equivalence ratio varies between 0.2 and 0.5, and the high CCV of the local mixture is also apparent in the standard deviation. In the ensemble average, the fuel is richer on the intake side at -40°CA and -30°CA while the mixture tends to homogenize at later imaging timings; nevertheless, the tendency of fuel inhomogeneity towards the intake side remains visible in the 8 mm plane. The standard deviation also decreases with time. An interesting trend is that the standard deviation is higher in the fuel-lean zones on the exhaust side, and at larger distance from the fire-deck. This implies that the fuel rich zone on the intake side has a rather repeatable equivalence ratio between cycles, while the equivalence ratio in the lean zone is sometimes close to zero and sometimes even higher than the global $\phi = 0.33$. A possible explanation is that fuel tends to accumulate in certain areas of combustion chamber after the injection-driven momentum has dissipated. At that point, only slow large vortices may persist in the flow-field and occasionally transport fuel into other areas of combustion chamber.

The corresponding vertical plane is shown in Figure 37b. Note that the vertical FOV is wider than the transverse dimension of the horizontal light sheet, and note the “ 45° ” orientation of the vertical plane with respect to the horizontal-plane FOV as indicated in the very top left of Figure 37a. The average is based on only 10 single shots and cannot be considered fully converged. However, the statistical significance is sufficient to draw some conclusions. Similarly, to the horizontal plane, there is significant small-scale variation within the vertical imaging plane, but the mixture homogenizes approaching the TDC. Inhomogeneity near the piston surface is visible, associated with the downwards fuel-jet trajectory during injection. After the impingement on the piston, the fuel jet likely recirculates through the parts of the cylinder than cannot be seen and re-enters the FOV from the side. Some indication of this is visible in the top-right image corner that shows richer mixture.

By delaying the SOI to -90°CA , the mixture variability within the imaging plane increases, as seen in Figure 37c. Small-scale variations in the local mixture distribution are visible with ϕ varying widely between $\phi = 0$ and 1. In the ensemble mean, remarkable changes in fuel distribution through time can be observed in each plane. The 8 mm plane at -40°CA show a rather uniform equivalence ratio around $\phi = 0.5$ except in a small area on the exhaust side close to the wall, which is leaner with $\phi = 0.3$. Also, the 20 mm plane shows a similar distribution at -40°CA . At -30°CA the whole mixture is leaner as expected considering the ongoing mixing, however, the formerly lean zone on exhaust side in 20 mm plane became much richer. It appears the ongoing compression and recirculation after the jet impingement on piston pushed a cloud of richer mixture into the FOV. This becomes more obvious at -20°CA , where also 14 mm imaging planes show this fuel richer pocket of gas at the exhaust side. At -10°CA , the fuel pocket on exhaust side becomes wider and the global fuel distribution shows leaner mixture in the center with fuel richer zones at the cylinder periphery. This asymmetry might originate from the piston-bowl cutout that disturbs the flow and mixture formation, as suggested by Figure 52

in the appendix. The standard deviation reveals particularly high variability on the exhaust side with values high as 0.25. This is the zone which initially showed lean mixture followed by the arrival of richer gas brought into the FOV by the recirculation vortex and piston motion. It is possible that this mixture variability is associated with CCV of the timing when this fuel enters the FOV. The variation in the rest of the FOV is lower with values below 0.1.

The corresponding vertical view for injection at -90°CA is shown in Figure 37d. The overall mixture distribution is consistent with the jet penetrating downwards from the injector (fuel-richer zone in the center) and then forming a re-circulation zone that re-introduces the flow from the side. The charge continues to mix resulting in a rather homogenous mixture around -10°CA . The combination of both views shows the high CCV and complexity typically associated with three-dimensional evolution of the mixture formation.



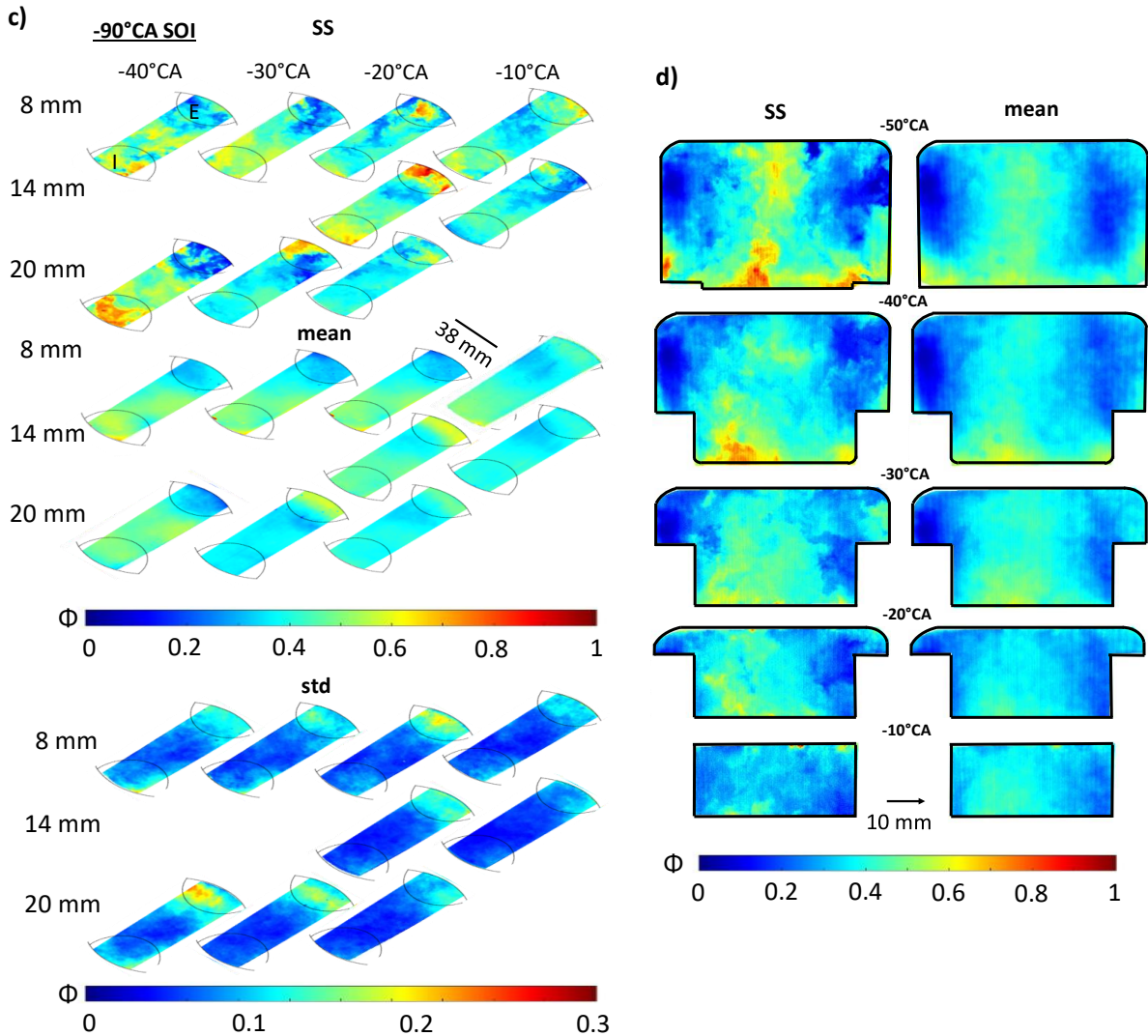
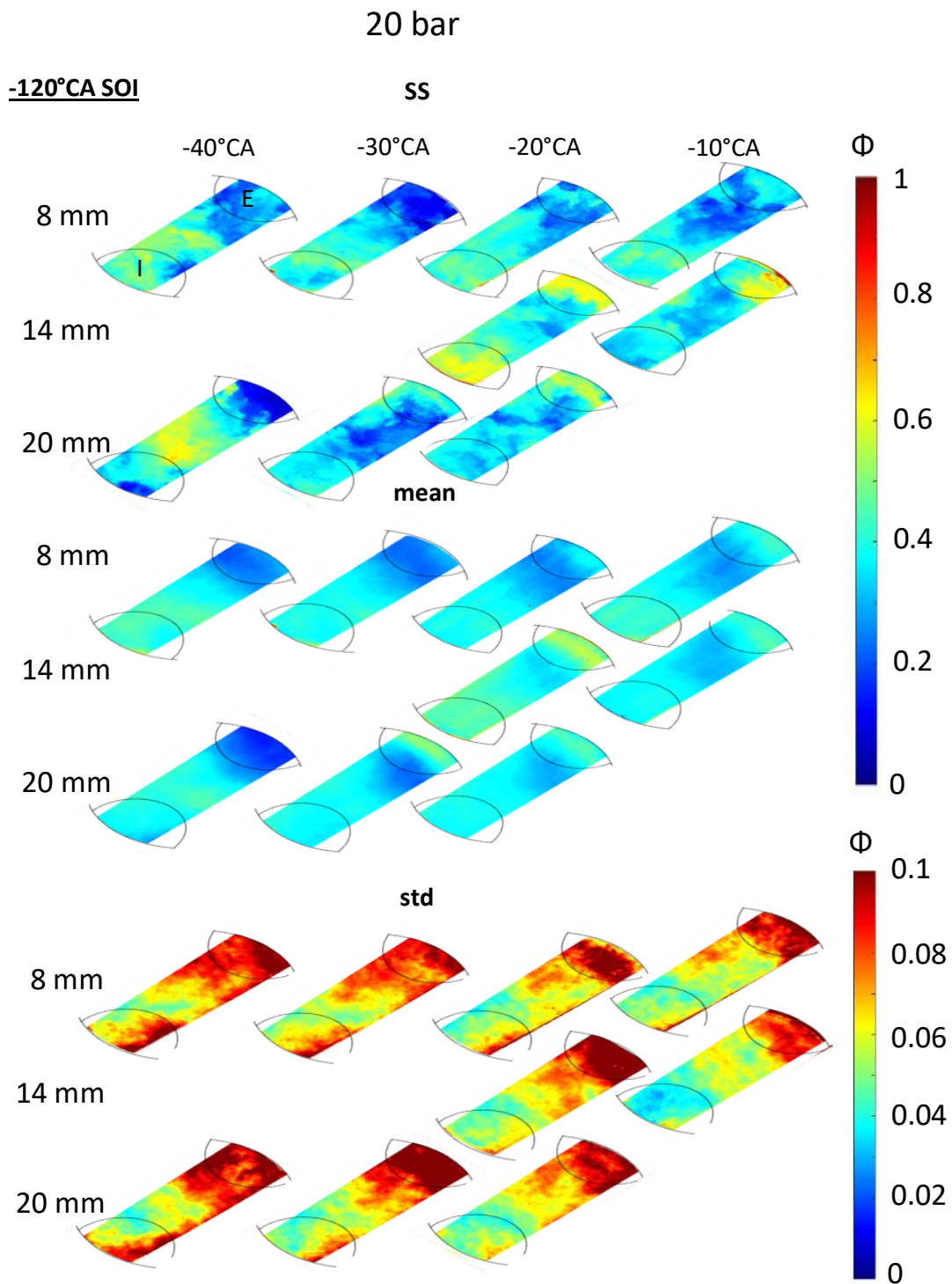


Figure 37. Single shots, ensemble mean, and standard deviation of the equivalence ratio at different heights for (a) -120°CA SOI and (c) -90°CA SOI and 40 bar injection pressure. (b) the corresponding vertical view for -120°CA SOI and (d) -90°CA SOI . Note that different parts of the figure may use different color plotting limits, as indicated on the right.

Figure 38 (top) shows the evolution of mixture formation for $\text{SOI} = -120$ and -90°CA at the lower injection pressure of 20 bar. Although the injection timing of -120°CA is early during the compression stroke, the impact of the longer injection duration is readily apparent. Single shots of the equivalence ratio exhibit strong gradients and much small-scale fluctuation. Compared to injection with 40 bar (Figure 37), the lower pressure results in a higher standard deviation but the overall mixture evolution is similar to that with 40 bar injection pressure. The same intake-biased mixture inhomogeneity at -40°CA and -30°CA is visible, followed by a fuel cloud arriving from below at the exhaust side of combustion chamber, which results in leaner mixture in the center and richer mixture at the combustion-chamber periphery. The standard deviation also shows spatial features similar to Figure 37. However, the standard deviation and the ensemble mean resemble those for 40 bar injection pressure and $\text{SOI} = -90^\circ\text{CA}$ more than for

SOI = -120°CA . Considering the nearly doubled injection duration but reduced jet momentum, it is not surprising that a longer mixing time is required to reach a similar mixture distribution.

The mixture evolution for -90°CA SOI and 20 bar injection pressure (bottom of Figure 38) shows features that are significantly different from what was seen for both the earlier injection at 20 bar and injections with 40 bar injection pressure. The single shots show a similar variation with ϕ ranging from almost zero to 1, with small scale variations and sharp gradients in the imaging plane. However, in the ensemble mean at -40°CA , most of the fuel is in the center of FOV rather than towards the intake side. This centered distribution is distorted by a richer pocket of gas entering on the exhaust side, from below (visible at -30°CA). Through -20°CA to -10°CA , the centered fuel-richer mixture is shifting towards the intake side while the richer-pocket entering the FOV from exhaust side is further expanding. The ensemble-mean fuel distribution at -20° and -10°CA therefore resembles that for earlier injection timings, however, the fuel-leaner region is somewhat off-center, biased to the exhaust side. Comparing the standard deviation for 20 bar injection pressure to that with 40 bar injection pressure, higher deviations especially at -40°CA are observed. Even though the values for 40 bar injection pressure show a higher maximum with roughly 0.2 on the exhaust side, overall, the variability with 20 bar is about 0.15, significantly greater than with higher injection pressure. However, towards later crank angles, the standard deviation approaches similar values and patterns as with 40 bar injection pressure.



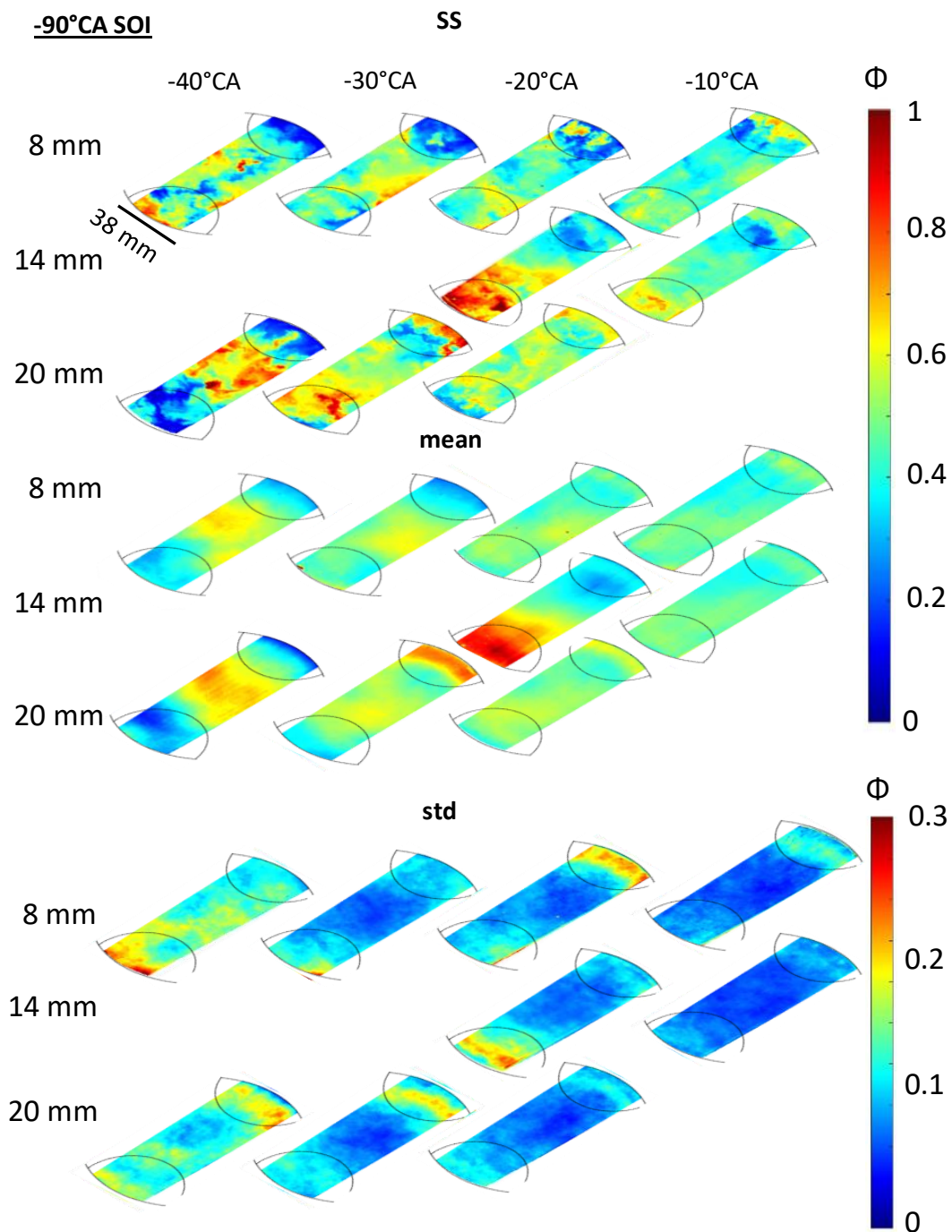


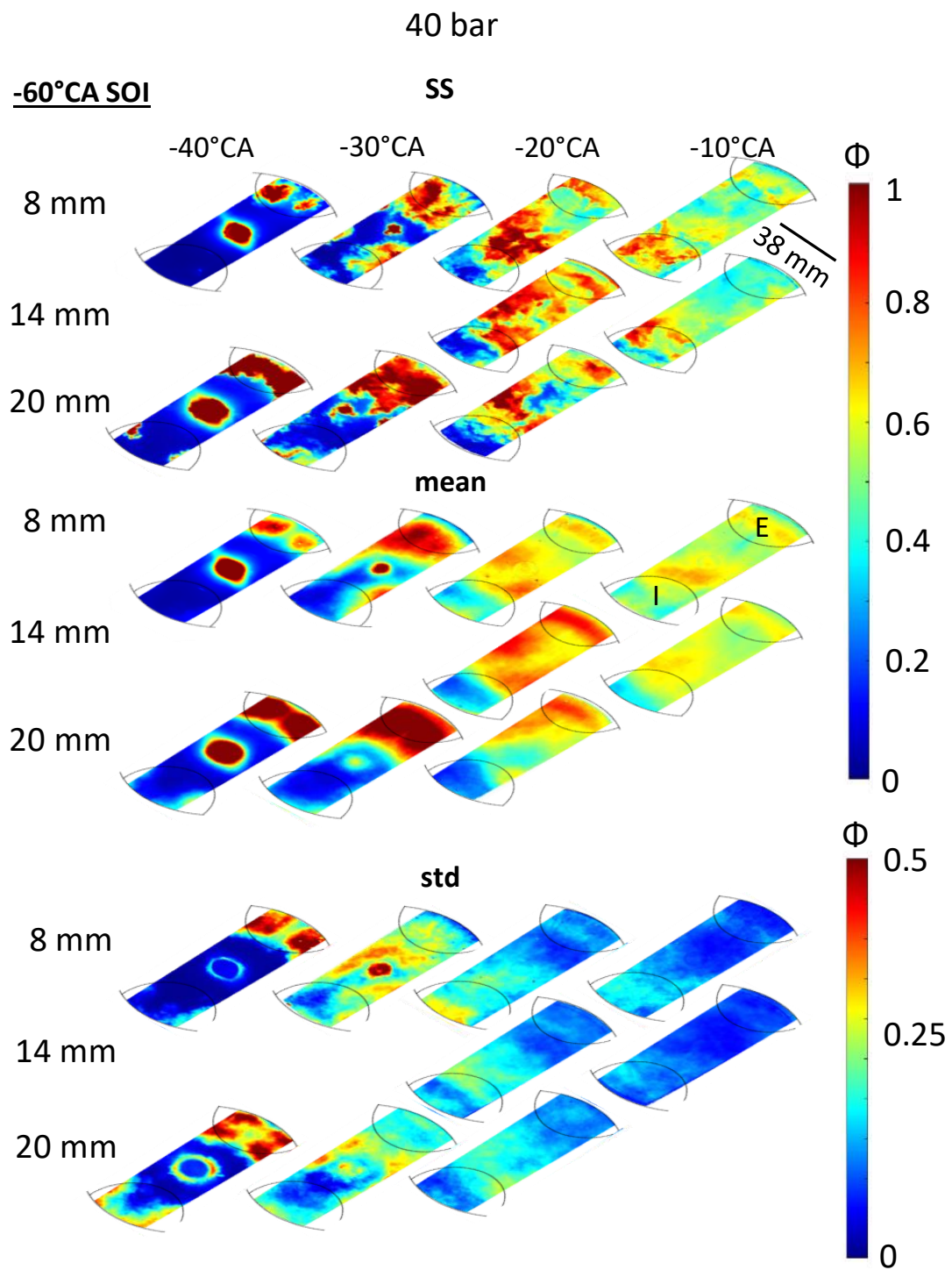
Figure 38. Single shots, ensemble mean, and standard deviation of the equivalence ratio at different heights for (top) -120°CA SOI and (bottom) -90°CA and 20 bar injection pressure. Note that different parts of the figure may use different color plotting limits, as indicated on the right.

Finally, the latest injection timing of -60°CA is analyzed for both injection pressures based on Figure 39. The injection ends at -39.3°CA and -24.7°CA for 40 bar and 20 bar OPs, respectively, assuming a 0.5 ms injector closing transient. This means that the injection is still ongoing at early imaging timings, which caused the fuel-richest regions in the jet center to be

overexposed, i.e., the detector saturated. The standard deviation there is then severely underestimated, but the rest of the images are not affected.

Figure 39 demonstrates the global pattern of the jet penetrating downwards, impinging on the piston, and then recirculating towards the cylinder head along the cylinder walls (which occurs similarly, but faster due to the then lower pressure, just after early injection at $\text{SOI} = -340^\circ\text{CA}$, see Figure 35 bottom row). At 40 bar -40°CA (Figure 39 top), the jet in the center and the recirculated fuel near the piston-bowl wall are visible. However, at reduced injection pressure (20 bar, Figure 39 bottom), it takes until -30°CA for the recirculated fuel to become visible, which is explained by the lower jet momentum and slower penetration. Asymmetry in the jet recirculation is visible for both injection pressures, with a much wider and more prominent fuel cloud visible on the exhaust side of combustion chamber. For this late injection timing, the asymmetry is attributed to the bowl-rim cutout on the intake side needed for optical diagnostics – mixing experiments with the bowl-rim rotated by 180° to shift the cutout from the intake to the exhaust side showed a 180° rotated mixture distribution (see Figure 52 in the appendix). The asymmetric recirculation remains apparent for both injection pressures even at -20°CA and -10°CA . However, for 40 bar injection pressure, the fuel reaches all parts of combustion chamber except for a narrow region near cylinder wall on the intake side. The differences between different planes are relatively small at -20 and -10°CA . In contrast, for 20 bar injection pressure, wide regions devoid of fuel remain at -20°CA and -10°CA due to insufficient time for mixing, reduced jet momentum, and longer injection duration.

Overall, the single shot images for injection at -60°CA show locally very rich mixtures exceeding stoichiometry even at the latest imaging timing of -10°CA (Figure 39). This results in a high standard deviation of mixture, particularly at the edges of regions with high fuel concentration. By -10°CA , the 40 bar case is sufficiently mixed such that maximum standard deviation has decreased to about 0.18, which is only somewhat higher than found for earlier injection timings. At 20 bar injection pressure, the mixing does not progress sufficiently, and the standard deviation remains high even at -10 CA.



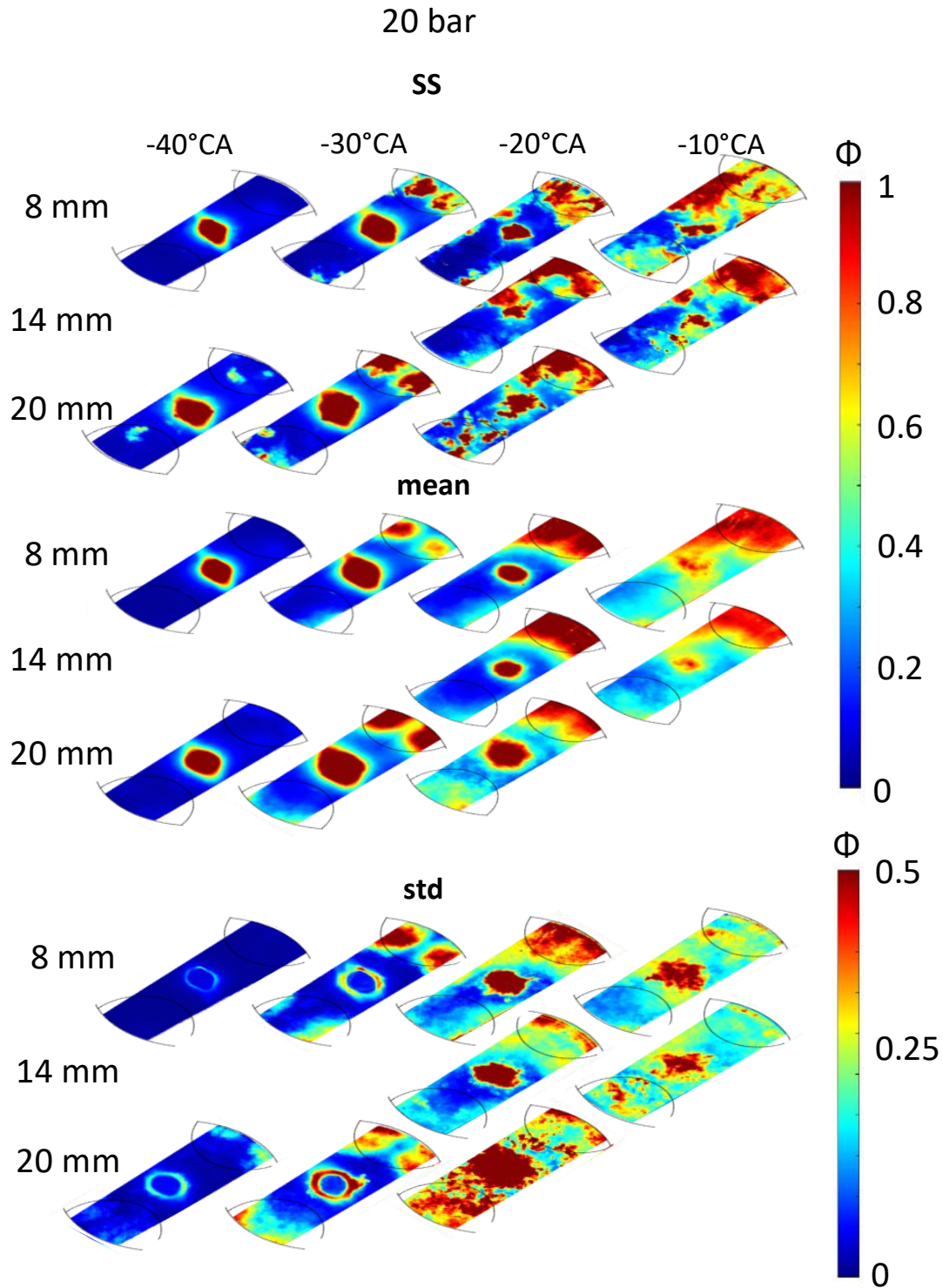


Figure 39. Single shots, ensemble mean, and standard deviation of the equivalence ratio at different heights for -60°CA SOI and (top) 40 bar and (bottom) 20 bar injection pressure. Note that different parts of the figure may use different color plotting limits, as indicated on the right.

5.3.3 Mixture statistics

One disadvantage of H_2 for engine combustion is associated with its high adiabatic flame temperature and associated tendency to form NO and then NO_2 . The formation rate of NO

increases exponentially with temperature and is therefore highly sensitive to local equivalence ratio. To obtain an indication of how much NO_x might be produced with the OPs from this study, Figure 40 represents the probability density functions (PDF) of the equivalence ratio at -20°CA, derived from accumulating over all single-shot images in all three horizontal imaging planes to gain an as representative information of global mixture state as possible. The -20°CA imaging timing corresponds to a typical spark timing for SI engines. Each PDF is normalized by the total number of data points (pixels), i.e., each has equal area under the trace. The vertical black dashed lines indicate the global equivalence ratio of $\phi = 0.33$.

The early injection timing (-340°CA) at 40 bar pressure is likely the best-mixed operating point. The PDF spans a range of ϕ from 0.25 to 0.48 with a peak at $\phi = 0.33$ and is somewhat skewed towards leaner values. The PDF mean value is at somewhat higher ϕ than the nominal global mean of 0.33, which is likely due to quantification errors. The effect of injection on global temperature may contribute as well. The slight shoulder at $\phi = 0.38$ stems from the plane 8 mm below the fire deck. In this plane the mixture is measured to be slightly richer than in the other two planes, which is likely to be a quantification error. Decreasing the injection pressure to 20 bar yields a similar, but more symmetric result. The peak of the PDF is at $\phi = 0.34$, with a similar overall width as for 40 bar but with a more symmetric distribution.

The equivalence-ratio PDFs for SOI = -180 CA are similar at both injection pressures: symmetric Gaussian-like PDFs that are wider than with injection at -340°CA and shifted towards globally leaner mixture, peaking at $\phi = 0.28$ -0.31. The PDFs for these cases have peaks at up to 17% leaner equivalence ratio than the global $\phi = 0.33$. It is possible that a significant portion of fuel is located near the piston and in the squish volume, both zones that were mostly outside of the FOV. Additionally, the increase in global temperature associated with injection of H₂ into a closed volume would yield lower LIF signal and thus lower apparent equivalence ratio. The uncertainty of tracer concentration in individual H₂ batches may have contributed as well.

For SOI = -120°CA and -90°CA, the peak of the PDFs is at higher ϕ than the global ϕ (20-60% deviation). The distribution becomes wider and with increased ϕ as the injection is delayed and the injection pressure reduced. Thermodynamic analysis shows that at these operating points, the injection has a neutral or even a cooling effect on the charge, contrary to the earlier timings. An additional source of error is associated with the 1st-order temperature correction applied here – in reality, the fuel-richer zones will be cooler than the global temperature, which in fact biases the mixture quantification to fuel-richer values. Potentially, some fuel is also located outside the zones probed by the laser light-sheet.

The latest injection timing (-60°CA) has the strongest inhomogeneity with the PDF spanning ϕ from 0 to >1. Similar reasons as in cases with SOI at -90° likely bias the maximum of PDF to values above the global ϕ . The PDF at -60°CA SOI and 20 bar is not to be interpreted quantitatively, with the injector closing less than 1 ms before the imaging time and the

associated strong fuel inhomogeneity. The peak is close to zero and wide areas are devoid of fuel.

Overall, increased NO_x formation can be expected with equivalence ratios above 0.5 [144]. The analysis in Figure 40 suggests that at a global $\phi = 0.33$ in this engine, the injection timings -120°CA and later will incur increased NO_x formation, with an increasing magnitude at late injection timings.

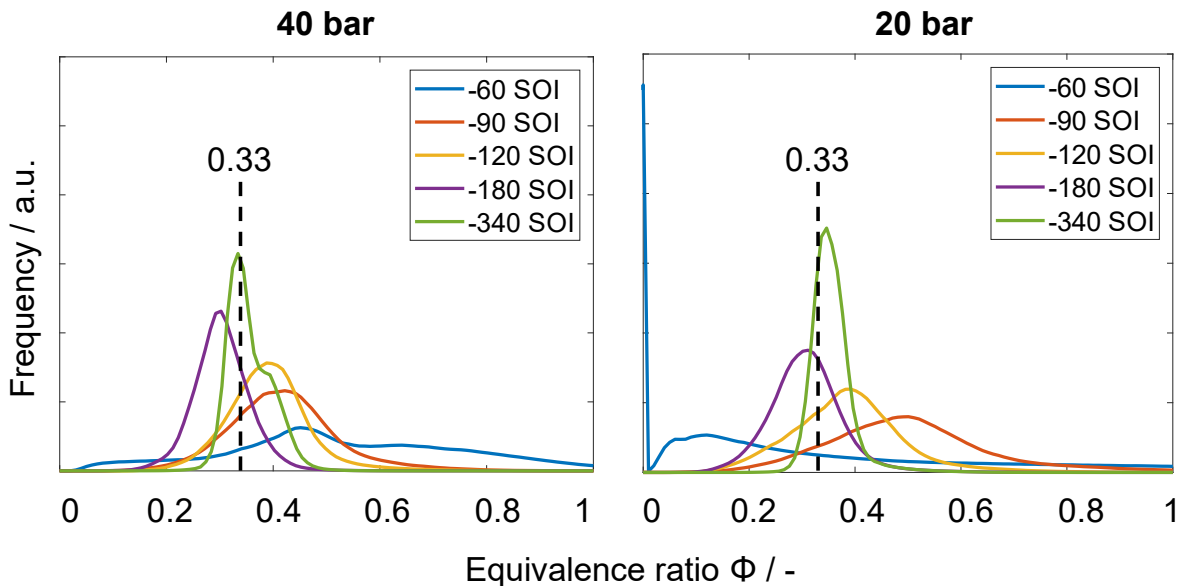


Figure 40. PDF of the equivalence ratio at -20°CA obtained from each SS of each plane for different injection timings and with (left) 40 bar and (right) 20 bar injection pressure.

While the global ϕ PDF offers insight into the NO formation potential, the local equivalence ratio at the potential spark-plug locations provides implications for CCV of combustion and the misfire tendency. Two regions of interest (ROIs) near the injector at 8 mm below the fire deck were chosen as potential spark-locations (Figure 41a). The equivalence ratio for each cycle within the selected regions was averaged to create a histogram plot (Figure 41b).

With an injection timing of -340°CA , the injection pressures lead to different results. The distribution for both injection pressure is between 0.27 and 0.5, but their peak is at 0.33 and 0.36 for 40 bar and 20 bar, respectively. As expected for a homogenous mixture, there are no major differences between the two regions. By delaying the injection timing to -180°CA , minor changes occur. The distribution for both injection pressures is wider and between 0.15 and 0.4, which indicates that some cycles may experience significantly leaner mixture at spark location, associated with a slower flame kernel evolution and CCV of combustion. The peak is at an equivalence ratio of about 0.3 and the red ROI (intake side) is at somewhat richer mixture. No major differences are seen between the two injection pressures.

When the injection takes place early during the compression stroke, at -120°CA , the first differences between the injection pressures become visible. With 40 bar the distribution is between 0.15 and 0.5, which is higher than with early injection timings. Furthermore, the red

ROI is slightly richer than the blue one. This is consistent with the inhomogeneity with a richer mixture near the intake valves. Decreasing the injection pressure to 20 bar reduced the ϕ at potential spark locations, though the red ROI was less impacted than the blue one. This is consistent with the mixture distribution from Figure 38. Moreover, the distribution spreads over a wider range of equivalence ratios for the blue ROI, implying an increased combustion CCV for this hypothetical spark location.

SOI = -90°CA shows predominantly richer conditions than the global ϕ , but a very wide distribution of equivalence ratio at potential spark timing. The width of the distribution at both pressures is roughly equal, though the 20 bar OP and the red ROI are slightly richer. At -60°CA and 40 bar injection pressure, the distribution remains very wide and predominantly at a higher equivalence ratio compared to earlier injection timings. However, at 20 bar, the mixture is predominantly leaner than global with only a few rich cycles detected. This is associated with the fact that the fuel jet that has not yet recirculated back into the imaging plane after the downward trajectory at injection. This operating point would be prone to misfire.

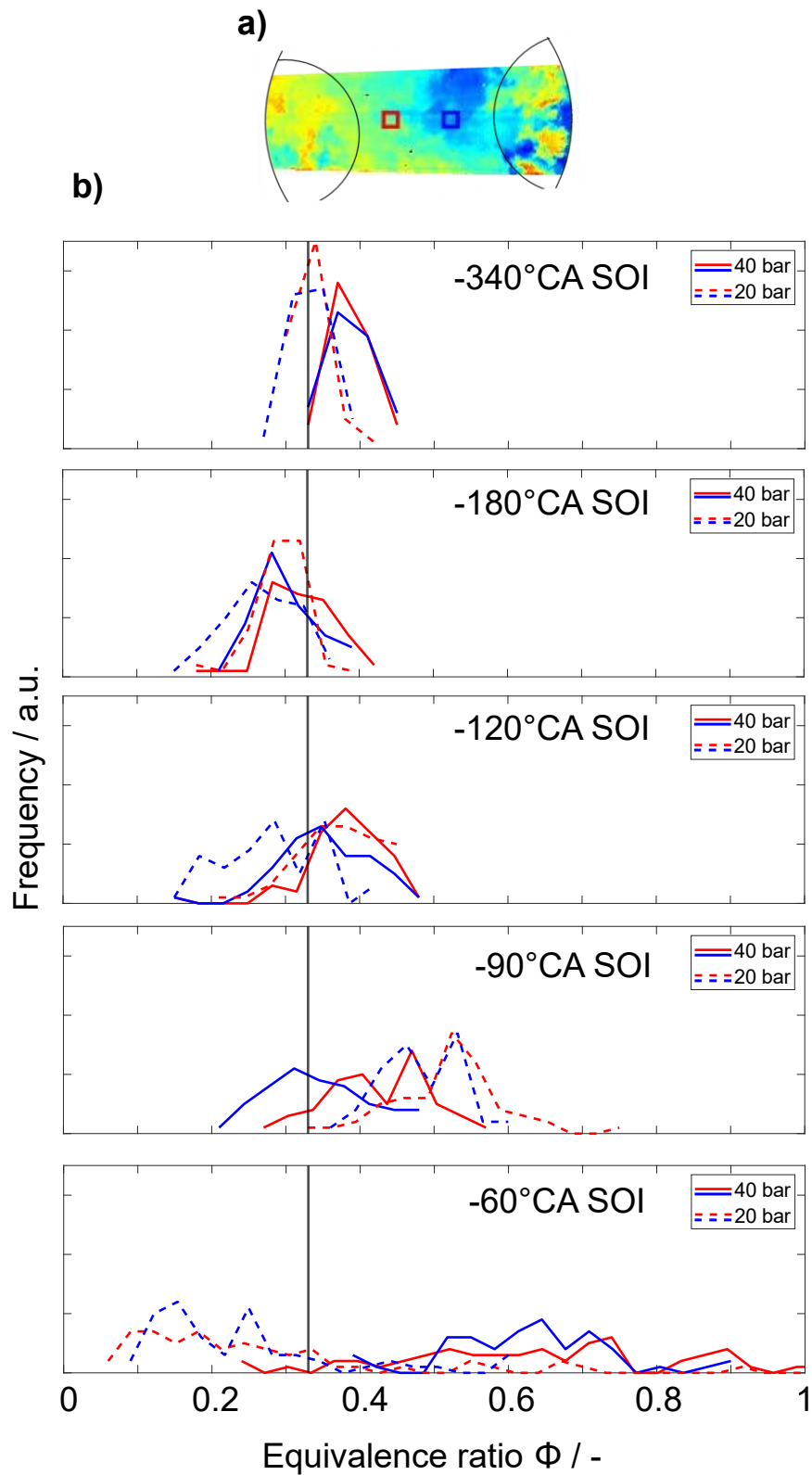


Figure 41. (a) Example single shot of the equivalence ratio and the areas used for the (b) PDFs. All PDFs are extract at a laser sheet position of 8 mm below the fire deck.

5.4 Chapter conclusion

A heavy-duty optical engine with diesel-type combustion chamber geometry was used to study in-cylinder mixture formation of H₂ directly injected from a centrally-mounted hollow-cone outward-opening medium-pressure injector. Via LIF imaging of a fuel tracer, the state of the mixture was quantified towards the end of compression stroke in different horizontal and vertical planes within the combustion chamber. The goal was to evaluate the effects of injection timing and injection pressure on the in-cylinder inhomogeneity and repeatability of fuel distribution. A statistical evaluation of the mixing state towards the end of compression offered insights into the potential impact of inhomogeneity on NO formation and the implications for combustion CCV.

As expected, retarding the injection timing and/or decreasing the injection pressure increased the mixture inhomogeneity, and more importantly, the CCV of mixture in certain areas of combustion chamber. In the ensemble average, injection during the intake stroke and at BDC created a homogeneous mixture, while injection at -120°CA created a mildly inhomogeneous mixture with the extreme mixture fractions deviating about 30% from the mean. However, significant inhomogeneity was observed for later injections at -90°CA and -60°CA, with a radially asymmetric mixture distribution. Single-shot images revealed significant CCV of the local equivalence ratio relative to ensemble-average. Even when injecting at -180°CA, the cyclic standard deviation of the equivalence ratio at certain locations exceeded 30% of the mean value. Later injection and/or reduced injection pressure additionally increased this standard deviation. In a fired engine, this would have implications for increased localized NO_x production. This engine is likely to produce less NO_x with injection timings at -120°CA or earlier. Late injection timings have a higher potential to produce NO_x. Furthermore, the late injection timings showed a high CCV in potential ignition locations, tending to cause misfire. Conversely, early injection should lead to fairly stable engine operation; however, this will be investigated in the following chapter 6.

The observed asymmetry of mixing in a rather symmetric combustion chamber with a centrally mounted injector and the high CCV in the mixture are not fully understood. Especially for late injections, the asymmetry appears to originate from the piston-bowl cutout made to allow optical access into the combustion chamber. Another likely explanation of asymmetry lies within the in-cylinder bulk flow field – a tumbling component of the flow and/or centripetal forces exerted on the jet by the swirl. In general, flow-field information is needed to explain this observation, along with the information on jet-induced flow and eddy structure. The CCV of mixture could stem from the low jet momentum and large combustion chamber geometry, which results in large-scale vortices and bulk-flow driving the mixing while mixing induced by the fine-scale turbulence is less prominent.

6 Cyclic variability in a hydrogen-fueled heavy-duty engine

This chapter presents a follow-up study on the findings discussed in chapter 5, and the measurements were also carried out at Sandia National Laboratories. The early flame evolution and the mixture distribution for different injection strategies and ignition locations with H₂ were investigated. Most of the work has been published in Laichter et al. [145] and was presented at the JSAE/SAE Powertrains, Energy and Lubricants International Meeting in Kyoto in August/September 2023.

6.1 State of the art

Significant optimization potential (efficiency, NO_x) exists for injection hardware and operating strategies with DI. The PFI approach suffers from several issues, such as backfiring, pre-ignition, increased turbocharging requirements, and limited engine power density, which makes DI more promising for demanding applications [107,146,147]. By injecting directly into the combustion chamber during the compression stroke, backfiring can be avoided, and the volumetric efficiency increases compared to PFI. Delaying the injection reduces the exposure time of a flammable mixture to hot-spots and therefore decreases the risk of pre-ignition to a certain extent, but requires higher injection pressures to ensure fast mixture formation because of the elevated in-cylinder pressure at the time of injection [110,147,148].

The injection timing in H₂-DI engines controls the mixture homogeneity that can range from nearly premixed to substantially inhomogeneous [49,58,105,111]. Various ignition concepts are compatible with H₂-DI, e.g., spark plug, pre-chamber, and diesel pilot, each featuring specific requirements for reliable operation. This work focuses on the impact of the H₂-DI operating strategy on engine performance with spark ignition. Work by BMW and Argonne National Laboratory [127,144,149] reported that retarding the injection timing improves the engine brake efficiency, while only a minor impact of ignition timing was observed. The delayed injection reduces the compression-stroke work, while the resulting mixture stratification and elevated in-cylinder turbulence accelerate the initial flame growth and improve combustion phasing. Furthermore, the engine heat losses can be reduced when fuel stratification reduces the occurrence of fuel-rich mixtures near the combustion chamber walls [115,116], but a sub-optimal fuel stratification leads to increased heat loss and potential formation of hot-spots which can trigger pre-ignition. However, too much fuel stratification can substantially increase NO_x production [118–121]. A further potential disadvantage for late DI is increased CCV of combustion associated with variable mixture and/or flow near the spark plug [74].

To better understand the trade-offs between injector configuration and operating strategy, injection timing, engine performance, and pollutant formation, a combination of metal and optical engine experiments as well as use of numerical simulations is imperative. While many metal engine studies reported the impact of injection timing on efficiency, CCV and emissions, optical engine studies are less numerous and mostly focus on light-duty engines with a tumble combustion chamber geometry. Local equivalence ratio measurements using tracer LIF showed

increased mixture stratification with delayed injection timings and quantified the local CCV of the mixture distribution [52,123,126,140,150]. Furthermore, measurements using PIV demonstrated that the in-cylinder bulk flow can be strongly influenced by the injection event. It is the repeatability of the fuel stratification and in-cylinder flow that govern the CCV via the early flame evolution [58,150]. The studies that provided information on the mixture and flow effects on flame evolution and combustion CCV mostly used fuels other than H₂. In larger converted diesel engines with a flat cylinder head and swirling bulk flow, like the typical 1st-generation H₂-ICEs entering the market, the in-cylinder mixture formation and injection-induced flow and their impact on combustion and CCV are even less explored. This, in addition to the lack of validation data for numerical simulations [124,128–130,133,134], which have their own challenges when using H₂ fuel, are the main motivation for this work.

Here, it is attempted to correlate the in-cylinder mixture formation and the flow effects induced by the injection to subsequent flame kernel evolution and CCV, while providing much-needed validation data for future CFD simulations. A hollow-cone medium-pressure H₂-DI was used to inject H₂, and five different injection timings and two injection pressures were used to influence the in-cylinder mixing and flow. The charge was ignited by a focused-laser pulse at three locations within the combustion chamber and high-speed OH* imaging was used to track the flame kernel evolution. To establish a connection between the flame evolution and in-cylinder mixture, the instantaneous mixture-distribution in the plane of ignition was quantified in each cycle at the time of ignition via tracer LIF.

6.2 Heavy-duty optical engine and operating conditions

The Sandia-Cummins single-cylinder heavy-duty optical engine used here is already described in chapter 5.2. A schematic layout of the optical engine with the optics is shown in Figure 42; the major specifications of the engine and fuel system are also given in chapter 5.2 (in Table 6). The engine has a Bowditch piston with a simplified non-re-entrant cylindrical bowl and a flat fused-silica piston-crown window that allows unrestricted optical access to the whole bowl when viewed from below (see Figure 42).

6.2.1 Fuel and injection

A Borg-Warner DI-CHG10 medium-pressure outward-opening hollow-cone prototype injector was used to inject H₂ directly into the cylinder. A simplified geometry of the injector nozzle and the injector mounting are shown in previous chapter 5.2.3. The far-field flow-pattern of this injector resembles a single-hole nozzle flow – the initial hollow-cone jet rapidly collapses and the momentum of the resulting flow is primarily aligned with the injector axis, with limited axial spreading as it was shown in chapter 5.3.1.

The design steady flow rate for this injector is 10 g/s of H₂, and the actual flow is dependent on injection pressure. At 20 – 40 bar injection pressure used in this work, the pressure ratio across the needle creates choked flow. Therefore, the in-cylinder (back) pressure is not expected to impact the injected fuel mass, and the fuel flow-rate is roughly proportional to the injection

pressure. To determine the necessary energizing time to reach the desired in-cylinder equivalence ratio, the injected fuel volume was characterized at atmospheric back-pressure for a range of injection durations and injection pressures. The engine operating conditions are summarized in Table 8.

Table 8. Experimental conditions and test case specifications. SOI: start of injection.

Experimental Conditions					
Intake temperature [°C]	30				
Air flow rate [g/s]	22				
Engine speed [min ⁻¹]	1200				
Intake pressure [kPa]	100				
Injected H ₂ mass [mg/cycle]	21.6				
Ignition timing [°CA]	-20				
Skip-fire mode	9 motored cycles / 1 fired cycle				
DI fuel injection parameters					
Start of injection [°CA]	-340	-180	-120	-90	-60
Fuel pressure - p_{inj} [bar]	40			20	
Injection duration [ms / °CA]	2.37 / 17.0			4.40 / 31.7	
Imaging parameters					
Timing [°CA]	-20				
Light sheet position below fire deck [mm]	14				

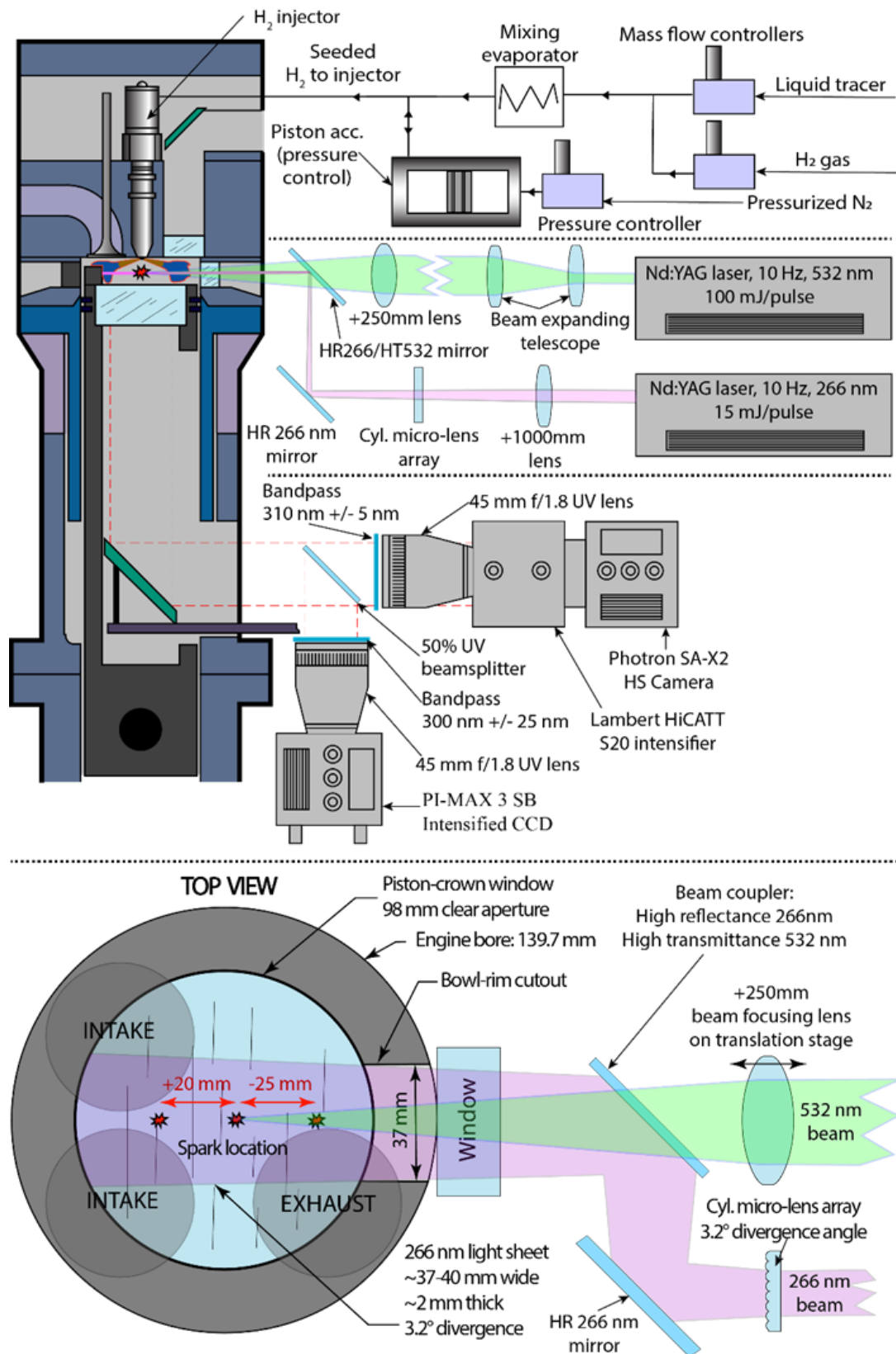


Figure 42. Schematic set-up of the optical engine including side-view optical setup details (top). Top-view optical setup (bottom). Note that for clarity, in the top view the 266 nm beam is shown incident on the beam coupler from the side, but the actual geometry was the vertical arrangement shown in the side view.

6.2.2 *Optical setup*

The optical setup served the purposes of ignition (laser spark), tracking the flame evolution (OH^* chemiluminescence), and imaging the fuel equivalence ratio just before ignition in one plane in the combustion chamber (tracer LIF). Both lasers (ignition and tracer LIF) were phase-locked to the engine rotation and operated at their nominal pulse frequency of 10 Hz, which yields 1 pulse per 2 engine revolutions at 1200 rpm engine speed. The tracer-LIF laser was triggered 1 μs (or 0.0072 $^\circ\text{CA}$) before the ignition laser, which can be considered quasi-simultaneous.

Laser ignition

Laser-induced plasma ignition was used to ignite the H_2 -air charge. For this purpose, a pulsed laser beam (Nd:YAG, Spectra-Physics Quanta-Ray Pro-270, 100 mJ/pulse at 532 nm) was focused in the engine combustion chamber to create a plasma at the focal point 15 mm below the fire-deck, with the corresponding optical setup shown in Figure 42. For repeatability and reliability, the pulse energy was set 30% higher than the minimum energy that created a spark. First, the laser beam was expanded to roughly 20 mm diameter to reduce the risk of damaging engine optical elements, and then focused by a 250 mm focal-length spherical lens mounted on a translation stage to shift the spark location. Three spark locations were used to explore the role of spark location on subsequent flame evolution: a central position, one shifted +20 mm to the intake side, and one shifted -25 mm towards the exhaust side. The risk of damage to optical elements due to back reflections prevented spark locations closer to the edges of the bowl.

In addition to laser-induced ignition at the intended location, two other, unintended phenomena occurred: *misfiring*, in which a flame kernel failed to form, and *additional* laser-induced ignition spots that started flame kernels in locations other than the intended one. Both were relatively rare in most, but not all, operating points, and they are discussed in more detail in the section “Results”.

OH^ chemiluminescence imaging*

The flame evolution after ignition was tracked by high-speed OH^* chemiluminescence imaging at 40 kHz frame rate. The chemically excited hydroxyl (OH^*) radical is one of the few species in H_2 combustion emitting chemiluminescence, in the wavelength band 305-320 nm. This emission was collected by a 310 ± 5 filter (Edmunds #34-980) and 45 mm f/1.8 UV lens (Cercos 2073) and recorded by a high-speed camera (Photron SA-X2) equipped with an image intensifier (Lambert Instruments HiCATT, S20 photocathode). The resulting projected pixel size was 0.26 mm/pixel and the intensifier exposure time was set to 20 μs .

Tracer LIF

The mixture distribution just before ignition was probed by LIF imaging of anisole added to the fuel, as discussed in the section “Fuel and injection”. Tracer fluorescence was excited by an Nd:YAG laser (Spectra Physics GCR-270) at 266 nm. A roughly 2 mm thick light sheet was

formed by a spherical lens (+1000 mm focal length) and a cylindrical micro-lens array (Edmunds, #86-844). This light sheet was combined with the focused beam used for laser-ignition using a dichroic mirror, and the two beams were aligned to propagate along the same axis to enter the combustion chamber through the cylinder-liner window and a 37 mm wide cutout in the cylinder head. This allowed imaging the local equivalence ratio in a horizontal plane that included the ignition location. As indicated in Figure 42, the sheet was slightly diverging in the transverse direction. The pulse-energy of the light sheet in the combustion chamber was about 10 mJ/pulse. At this laser fluence of about 13 mJ/cm² with air as the bath gas, the fluorescence intensity is in good approximation linear in laser energy [50,151,152]. A fast photo diode (Thorlabs DET10A) connected to a boxcar integrator (SRS SR250) measured the energy of each laser shot.

The tracer fluorescence was imaged through the piston-crown window by an intensified CCD camera (Princeton Instruments PI-MAX 3, SB photocathode) equipped with another 45 mm f/1.8 lens and a 300±25 nm bandpass filter (Edmunds #12-097). The camera operated with 500 ns intensifier exposure time and no binning, resulting in projected pixel size of about 0.13 mm/pixel. The OH* and tracer LIF cameras shared the same optical axis via a 50% broadband UV beamsplitter (Thorlabs, #48-192).

6.2.3 Post-processing

The data processing and the uncertainties of tracer LIF imaging in motored operation with nitrogen were discussed in detail in chapter 5.3. With air as the bulk gas, according to the FAR-LIF approach from Reboux et al. [51] the equivalence ratio ϕ is proportional to the LIF signal. The images can therefore be quantified by referencing them to a “flat-field” derived from LIF images with a homogeneous fuel distribution at known equivalence ratio. In this study, an early injection timing at -320°CA under otherwise the same operating conditions was used for the flat field. This very early injection was shown in previous work to form a highly homogeneous mixture. Reboux’s FAR-LIF approach is inaccurate when the local oxygen concentration is low, which here corresponds to extremely rich mixtures during and just after injection [63].

The described single-step flat-field correction accounts in first order for the global temperature dependency in the fluorescence and for inhomogeneities in illumination and detection. Late injections timings result in high mixture inhomogeneity. The local temperature variations then translate into variations in fluorescence yield that are not corrected by the flat-field approach. Previous work showed that the associated maximum error is about 5% in nitrogen atmosphere (see Fig. 5 in [153]). Since the temperature dependency of anisole’s fluorescence quantum yield is lower in air than in nitrogen (Fig. 8 in [154]), the expected uncertainty is also lower here.

To extract the burnt gas area from the OH* chemiluminescence images, in a first step, an average of 10 dark images (recorded before the ignition) in each cycle is subtracted from the single shots of the flame. A 5x5 pixel median filter reduced shot noise. The apparent burnt area was extracted by a “predictor-corrector scheme” [82], where a dynamically adjusted intensity threshold segments the images

6.3 Results

6.3.1 In-cylinder mixture formation

An overview of the ensemble-averaged mixture distribution just before ignition for variations in injection timing and injection pressure is shown in Figure 43. Early injections at -180°CA yield a rather homogeneous mixture at spark timing (-20°CA), with an equivalence ratio of $\phi \approx 0.3$ for both injection pressures. Also, the standard deviation of equivalence ratio within the measurement plane (std_ϕ) is quite low (0.05-0.07) with this SOI. The somewhat higher standard deviation with reduced injection pressure (20 bar, bottom plot) is associated with longer injection duration and slower mixing, which can lead to locally inhomogeneous zones in some cycles.

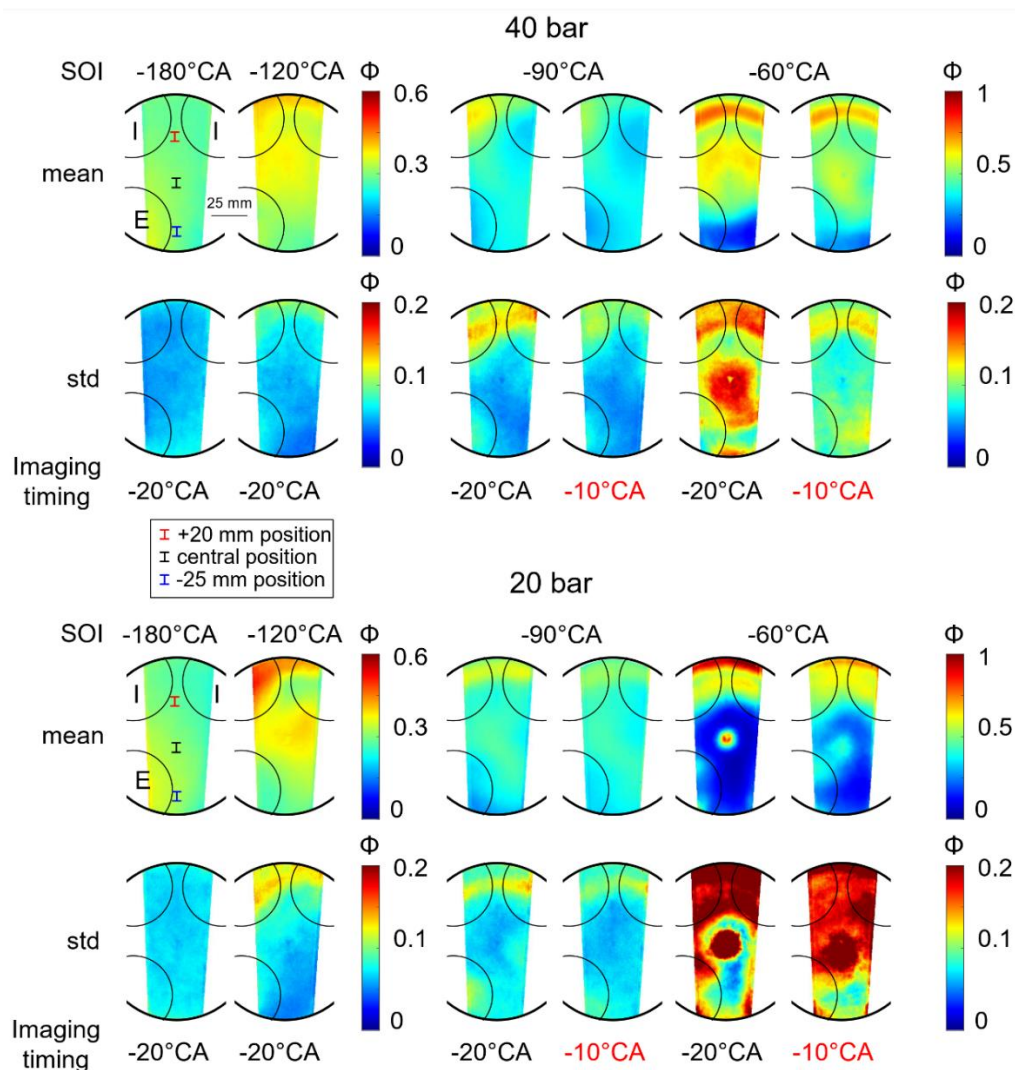


Figure 43. Ensemble mean of the equivalence ratio and corresponding standard deviation at different injection timings and pressures. For the late injection timings two different imaging timings are shown. (For the earlier ones the fuel distribution did not change significantly over 10°CA .) Each image panel shows the entire FOV within the 98 mm piston bowl. The light sheet is 37 to 40 mm wide. “I” and “E” indicate the intake and exhaust valves, respectively. Note that different parts of the figure use different color plotting limits, as indicated with the color bars.

Retarding the injection timing to -120°CA increases the mixture inhomogeneity at ignition for both injection pressures. The mixture is richer on the intake side of the combustion chamber and shows a small gradient throughout the FOV from $\phi = 0.4$ at the intake side to 0.25 at exhaust side for 40 bar injection pressure, and from 0.5 to 0.25 for 20 bar injection pressure. As expected, the standard deviation also increases; however, the distribution of the standard deviation is not uniform but it increases from $\text{std}_\phi = 0.05$ in the center and exhaust side of the combustion chamber towards 0.1 on the intake side. The standard deviation is again somewhat higher at reduced injection pressure. Both the asymmetric mixture distribution and the increased CCV on the intake side are likely associated with the asymmetric in-cylinder flows caused by the bowl-rim cutout. In the previous chapter 5 it was shown that rotating the bowl-rim by 180° around the cylinder axis rotated the mixture field correspondingly by 180° .

Delaying the SOI to -90°CA , the mixture is even more stratified but with an overall similar distribution as for injection at -120°CA at both injection pressures. Two imaging timings (-20°CA and -10°CA) were used because the fast combustion associated with late injection (see below) resulted in very early combustion phasing with ignition at -20°CA . In comparison, the mixture becomes more homogeneous and shows reduced standard deviation at -10°CA , but the large-scale pattern remains the same. This means that the mixture distribution at -20°CA is quite representative for the entire phase of early flame propagation (but information is only available in that single plane 14 mm below the fire deck, not in three dimensions).

The latest injection timing used in this study is -60°CA . As expected, both injection pressures yield significantly increased mean mixture stratification and standard deviation relative to earlier SOI. Particularly with 20 bar injection pressure, where the injection ends around the imaging timing, the fuel likely enters the bowl-rim cutout volume and is not visible within the FOV at the exhaust side. The toroidal high- ϕ zone that forms roughly 15 mm from the piston-bowl rim on the intake-side is most likely a result of toroidal flow recirculation created in the piston bowl and is also visible for earlier injection timings. This recirculation is disturbed by the bowl-rim cutout on the exhaust side.

6.3.2 Thermodynamic combustion analysis

A successful ignition requires suitable fuel concentration at the ignition location and also depends on the local flow field and potential heat-losses to the spark plug electrodes. By eliminating the latter effect, laser ignition can reduce the COV of the IMEP [155]. Since the flow field was not measured in this study, the focus is on the effects of local mixture on ignition and flame evolution. The resulting IMEP and its COV of the cycles that ignited as intended, calculated from the pressure traces, are summarized in Table 9. The overall trend is that the COV decreases with later injection timings, while the IMEP is nearly constant for each injection pressure, with injection at 20 bar yielding a slightly lower IMEP. The latter might be due to inaccuracy of the off-line atmospheric-pressure injector calibration, i.e., the low-pressure cases may have had slightly less fuel.

Table 9 also provides statistics of abnormal ignition events and misfires. Figure 53 in the appendix gives an impression what early combustion with additional ignition spots looks like. These spots are likely induced by the laser beam encountering a particle or oil droplet along its propagation to the focal point, causing additional ignition sites. This theory is supported by the higher probability of abnormal ignition when igniting at +20 mm, when the laser has to traverse a longer path through the combustion chamber. The cycles with abnormal ignition were excluded from further statistical analysis.

Table 9. Overview of operating conditions, basic cycle metrics, and ensemble statistics of ignition outcome. The COV is based only on the fired cycles without additional ignition spots.

SOI	Injection pressure	Spark position	IMEP / COV	No. of cycles	Ignition as intended	Additional ignition spots	Misfires
°CA	bar	mm	bar / %	-	%		
-340	40	+20	3.7 / 8.4	160	39,4	56,9	3,8
		central	3.8 / 1.6		75,0	24,4	0,6
		-25	3.7 / 2.8		93,8	6,3	0
-180		+20	3.3 / 19.7	80	36,3	57,5	6,3
		central	3.6 / 1.9		66,3	31,3	2,5
		-25	3.4 / 5.3		88,8	11,3	0
-120		+20	3.8 / 1	80	47,5	48,8	3,8
		central	3.8 / 1		71,3	28,8	0
		-25	3.7 / 1.9		90,0	10,0	0
-90		+20	3.9 / 1.1	80	46,3	50,0	3,8
		central	3.8 / 1.5		81,3	18,8	0
		-25	3.8 / 1.5		91,3	8,8	0
-60		+20	3.7 / 1.7	80	37,5	61,3	1,3
		central	3.8 / 2		75,0	25,0	0
		-25	3.9 / 2		87,5	10,0	2,5
-340	20	+20	3.1 / 12.16	160	51,3	45,0	3,8
		central	3.37 / 2.54		67,5	32,5	0
		-25	3.13 / 5		89,4	10,6	0
-180		+20	2.94 / 6.37	80	36,3	57,5	5,0
		central	3.15 / 4.62		70,0	30,0	0
		-25	2.98 / 0.07		88,8	11,3	0
-120		+20	3.32 / 1.87	80	27,5	70,0	2,5
		central	3.36 / 1.67		75,0	25,0	0
		-25	3.31 / 2.44		88,8	11,3	0
-90		+20	3.44 / 1.78	80	37,5	62,5	0
		central	3.43 / 1.46		70,0	30,0	0
		-25	3.48 / 1.62		98,8	1,3	0
-60		+20	3.5 / 2.25	80	37,5	55,0	7,5
		central	3.44 / 2.95		85,0	7,5	7,5
		-25	3.61 / 1.01		15,0	41,3	43,8

6.3.3 Misfiring cycles

Statistically, the ignition location at +20 mm was most prone to misfire. Table 9 shows a trend towards higher likelihood of misfire for early injections at 40 bar injection pressure and for the late injection timing at -60°CA with 20 bar injection pressure. In contrast to Peterson et al. [33], who found that in a spray-guided DISI engine with iso-octane as the fuel the flame never fails to *form*, but fails to *develop* sufficiently and then extinguishes, here, no flame at all was observed in misfired cycles or at least the imaging system's sensitivity was insufficient to detect it. Figure 44 seeks to explain the misfire by comparing the local equivalence ratio in misfired cycles to that for successful ignition events for injection at -90°CA , 40 bar injection pressure and the +20 mm ignition location. This choice of operating conditions is motivated by high-enough misfire frequency (3 cycles) and significant std_ϕ near the ignition location.

The global mixture distribution in all individual cycles exhibits locally very lean and richer zones with $0 < \phi < 0.6$. The gradients in the fired cycles are more pronounced, and all of them have a rich region in the upper left corner of the FOV while the extremely lean regions are smaller compared to the misfired cycles. However, comparing ϕ in the region close to the ignition location suggests that mixture distribution might not be the only reason for misfire. While cycle #09 and cycle #59 are indeed leaner near the ignition location ($\phi \sim 0.2$), cycle #57 appears to have sufficient fuel with $\phi > 0.25$ at ignition location. The successfully-ignited cycles #22 and #62 also show $\phi > 0.25$ at the ignition location, while cycle #40 seems to be an outlier with rather lean mixture at ignition location and yet successful ignition.

There are several reasons to explain these phenomena. One reason might be slight misalignment of the two laser beams, such that the ignition location does not perfectly overlap with the LIF measurement plane. Another explanation might be in the laser failing to produce a plasma, either due to beam-steering effects along its path, or pulse-to-pulse laser energy fluctuations resulting in some pulses below the threshold energy. In the next section, the correlation between the local mixture distribution and early flame kernel evolution is investigated.

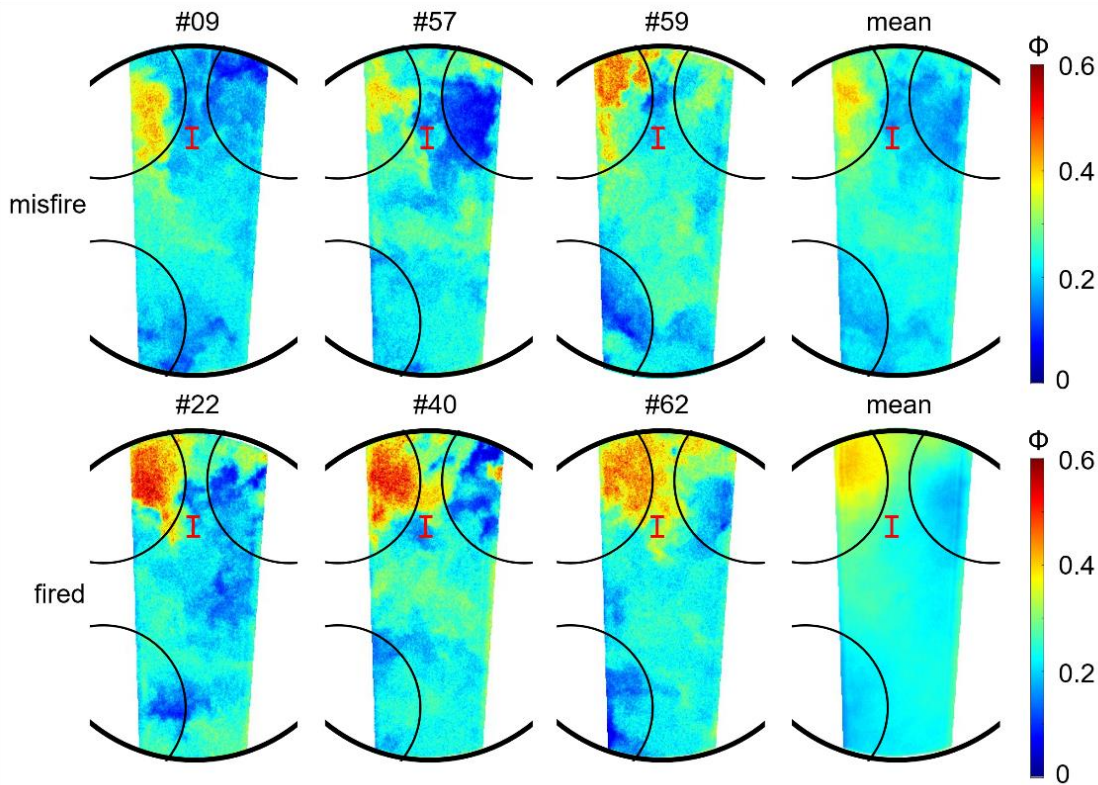


Figure 44. Comparison of the mixture distribution in misfire events (top row) with successful ignition (bottom row). The first three columns show single-cycle ϕ for randomly selected cycles, the last column shows the ensemble-average. Ignition timing at -20°CA , 40 bar injection pressure, SOI at -90°CA . The ignition location is marked in red.

6.3.4 Correlation between local mixture and early flame evolution

Central spark location

Figure 45 shows single shots of equivalence ratio and the corresponding flame development for different injection timings with 40 bar injection pressure. The selected cycles are “typical” in terms of their equivalent flame radius evolution being closest to the ensemble average at the specific operating conditions. The top row shows the “homogeneous mixture” reference case with SOI at -340°CA . The flame growth is reasonably symmetrical as expected based on homogeneous mixture and weak in-cylinder flow, in line with previous H_2 experiments reported by Aleiferis et al. [58].

Similar results are found with an SOI at -180°CA . Despite the locally inhomogeneous mixture (in single cycles, but more homogeneous in the ensemble average), the flame in this individual cycle shows a round shape with a steady growth in the center of the combustion chamber. The flame brightness is also similar to what is seen for SOI = -340°CA .

By retarding the injection to -120°CA the flame no longer evolves spherically. Note that wider ϕ plotting limits are chosen for this and later injection timings. At SOI = -120°CA , the equivalence ratio is higher on the intake side of the combustion chamber. At the ignition

location, $\phi = 0.5$ (higher than global ϕ) can be found. The brightness of the initial flame kernel 1°CA AIT and 5°CA AIT is more uniform, but less circular than with earlier injection timings. Notably larger flame area relative to earlier injection timings is visible at 5°CA AIT, and towards 10°CA AIT, preferential flame evolution towards the bottom right corner of the FOV is apparent. By 15°CA AIT the flame already reaches the edge of the FOV. When this happens, the data processing algorithm can no longer distinguish the dark zones in the center of the flame from the unburnt mixture. However, this happens late AIT, therefore, this algorithm deficiency does not impact the main conclusions of this work that focus on the early flame kernel growth.

An SOI of -90°CA yields a high- ϕ zone on the intake side and a more homogeneous mixture within the rest of FOV. At the ignition location, ϕ ranges from 0.4 to 0.5. As expected from comparable ϕ at ignition, the early flame kernel growth at 1°CA AIT and 5°CA AIT is similar to case with SOI = -120°CA, with a first asymmetry of the flame kernel noticeable by 5°CA AIT. Again, the flame preferentially propagates towards the exhaust side and grows much faster than with an SOI of -120°CA, reaching the edge of FOV by ~11°CA AIT. However, the preferential direction of flame propagation is not well-aligned with the equivalence ratio – based on the initial mixture distribution, one would expect the flame for these injection parameters to propagate equally towards the bottom-right and top-left direction in Figure 45, and a fast burning rate as the flame reaches the stratified zone at the intake side of combustion chamber. Three possible explanations are offered here: a) non-uniform mixture distribution in the third dimension (normal to the imaging plane 14 mm below the fire deck), and b) engine swirl and injection-induced flow convecting the flame kernel along with the flow, and c) changing mixture distribution between the imaging time (0°CA AIT) and the actual time when flame is observed (5°-15°CA AIT).

The equivalence ratio for SOI at -60°CA is highly stratified and significant fuel gradients can be found around the spark location. In addition, the injection-induced in-cylinder flow and turbulence will be strongest with these injection parameters. The flame kernel 1°CA AIT is slightly larger compared those for other injection parameters. 5°CA AIT, the flame is not only increasing in size, but also in brightness. At 10°CA AIT the flame already burned through more than half of the FOV with significant brightness gradients within the flame – some burnt zones are very bright and others dark. By comparing the flame across the different injection timings, it can be seen that retarding the injection towards ignition timing accelerates the flame growth. The dynamic range in intensity of OH* emission is wider for late injection timings and more homogeneous for early injection timings. This was also reported in [58] and is associated with inhomogeneous equivalence ratio.

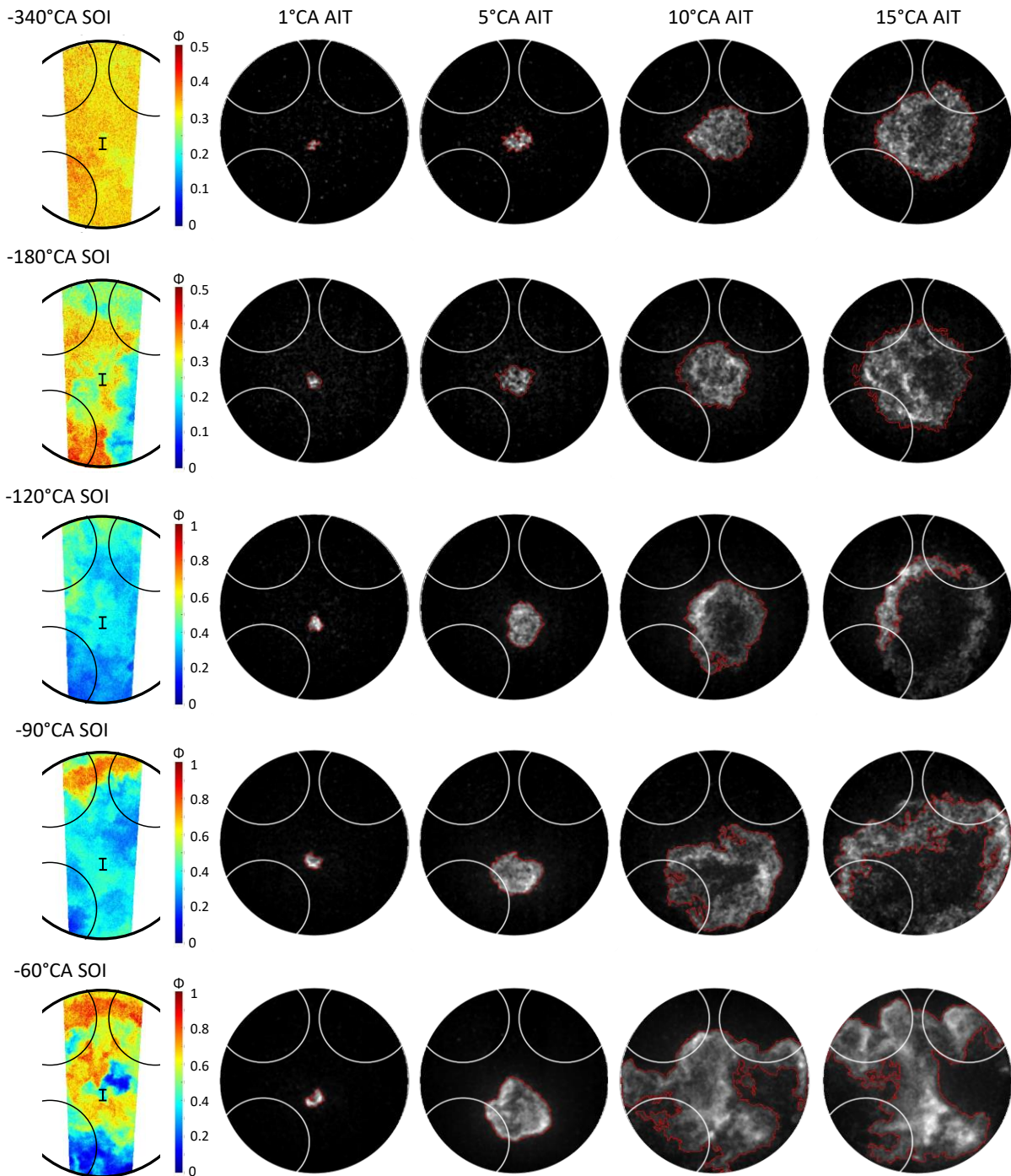


Figure 45. (First column) Single shots of the equivalence ratio at ignition timing at different SOIs and 40 bar injection pressure from a typical cycle according to the average flame radius evolution. (Remaining columns) Corresponding flame propagation with central spark location. The red line indicates the detected flame area. Each flame image is normalized by its maximum intensity. As recorded, images at later crank angles are much brighter than those at earlier ones.

Additional insights into the role of mixing and early flame evolution can be gained by an analysis of ensemble-averaged data. Figure 46 shows the average equivalence ratio at ignition and the corresponding flame probability maps within the FOV. The color of each individual pixel in these maps represents the probability that the flame (more precisely, the area

corresponding to burnt gas in the line of sight) was detected at the particular pixel at the selected time AIT (white – all cycles burnt at that location, black – no cycles burnt at that location, gray – some cycles burnt). The ignition location is in the center for all cases included in Figure 46.

The early injection during the intake stroke (SOI = -340°CA) results in homogenous mixture and repeatable symmetric flame evolution with low variability, as expected. A somewhat later injection (SOI = -180°CA) results in mostly homogeneous mixture with minor stratification towards the exhaust side. Despite the low stratification, the flame evolution is less repeatable, and some cycles show faster flame progression towards the exhaust side of combustion chamber (well visible at 10°CA AIT) where the ensemble average mixture is fuel-richer.

At SOI = -120°CA, the mixture appears somewhat fuel-richer in the LIF imaging plane relative to earlier injections, with the highest ϕ at ignition timing on the intake side. The flame evolves fairly symmetrical at 5°CA AIT – by 10°CA AIT, it becomes a bit asymmetric and, counter-intuitively, skewed towards leaner zones. This is either due to fuel-distribution outside the imaging plane or due to injection-induced flow. The overall trend of faster flame propagation with later injection timing is well visible in the flame probability.

Retarding the injection to -90°CA results in the fuel-richest zone in the upper left corner of the FOV, and leaner zones in the upper-right and bottom-left areas of the FOV. Quite repeatable flame evolution is observed at 5°CA AIT with a preferential propagation direction towards bottom-right, which becomes even more apparent by 10°CA AIT. Then, the flame for most cycles reaches the edge of the FOV on the exhaust side. Again, the preferential direction is likely caused by flow and/or out-of-plane stratification, though the result at SOI = -90°CA is less counter-intuitive than with earlier injection timings. Interestingly, similar trends were observed also with reduced injection pressure as demonstrated by Figure 54 in the appendix.

For SOI at -60°CA the mixture is highly non-uniform. Most of the fuel is on the intake side, and there is almost no fuel on the exhaust side. The center of the combustion chamber is varying around $0.4 < \phi < 0.6$. The initial flame kernel 1°CA AIT is slightly bigger than for the other cases, which is consistent with fast flame propagation. The cyclic variation of the flame-kernel evolution is quite high, and the flame does not burn towards the fuel rich zone on the intake side, but rather towards the lean zone. This phenomenon starts already at an SOI of -120°CA and becomes more pronounced towards later injection timings.

By calculating the centroid position of the flame and averaging the x- and y-position, the average movement of the flame centroids is shown for all SOIs in the burnt gas area 10°CA AIT. With a central spark location, the flame remains in the center for most of the injection timings. Only an SOI of -90°CA results in pronounced movement of the centroid, moving towards the bottom-right area of the FOV.

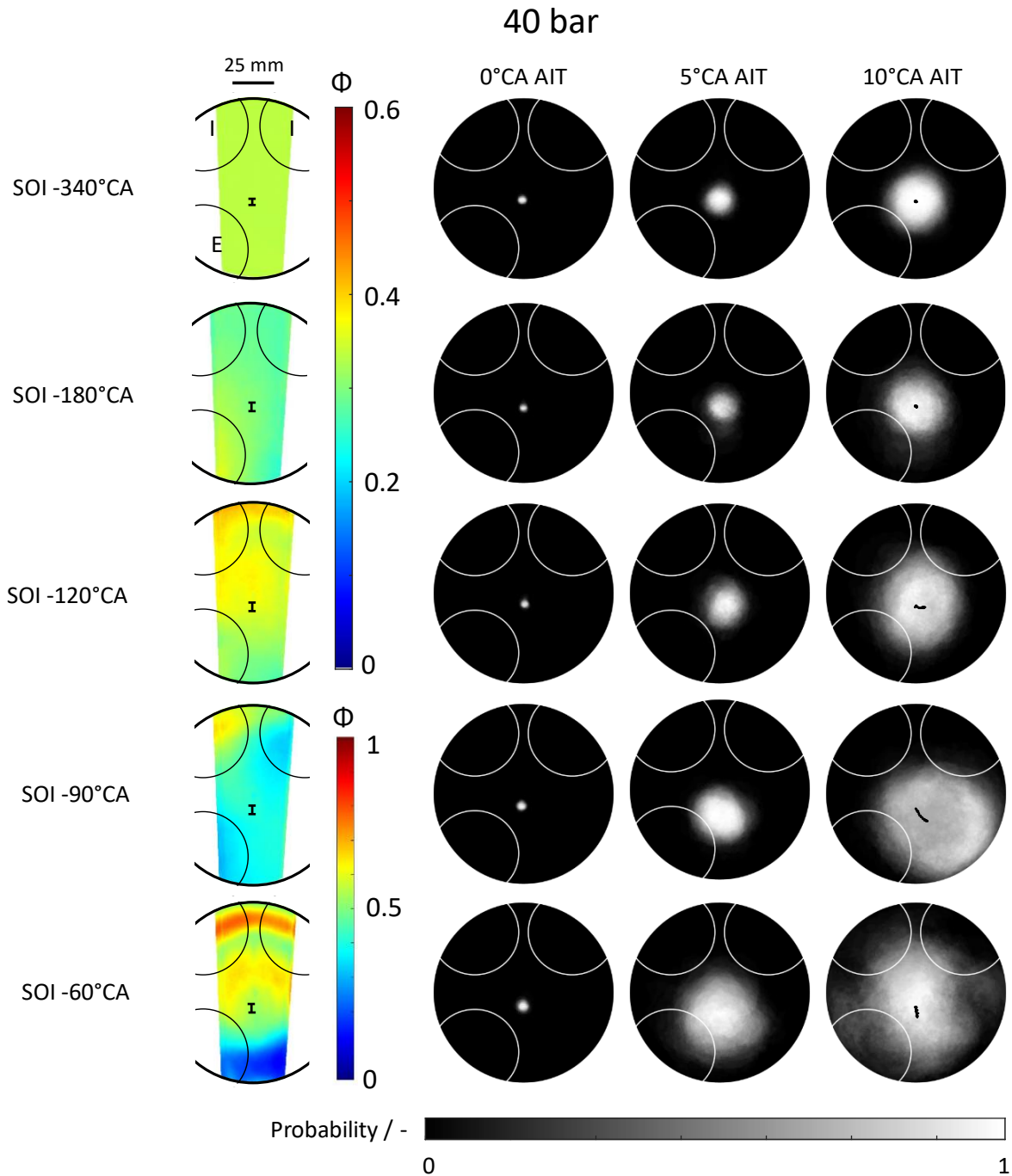


Figure 46. Average equivalence ratio and corresponding probability maps of detecting burnt zone at selected times AIT for varied SOI and 40 bar injection pressure. Additionally, the average flame centroid position from 0 to 10°CA AIT is marked in black in the burnt gas area 10°CA AIT. Central spark location (0 mm).

+25 mm and -25 mm spark location

For the two off-center ignition locations Figure 47 shows the flame probability maps. The flame kernels at 1°CA AIT seen here are very similar in size regardless of injection timing and ignition position, confirming the high repeatability of the laser ignition. Only the late injection timing

(-60°CA) indicates a slightly bigger initial flame kernel, i.e., immediately faster flame speed. For SOI of -180°CA and -120°CA, both spark positions yield similar combustion evolutions as observed with the central spark position. Minor variations in the size of flame kernel at 5°CA and 10°CA AIT are in agreement with the average ϕ around the ignition locations. As expected, a somewhat faster flame speed is observed when igniting in zones with higher ϕ , e.g., the +20 mm for an SOI at -60°CA compared to the -25 mm location.

With an SOI = -90°CA, consistently faster flame growth was observed relative to earlier injection, regardless of the ignition location. When igniting at -25 mm (top side Figure 47), the flame is rather symmetrical with a small preference to grow towards the right at later CAD. Note that the flame detection algorithm at 10°AIT for this ignition location (-90° and -60°CA SOI) does not work well since the intensity of the flame drops when the flame touches the wall, which affects the flame probability map (gray area at the bottom of FOV). When igniting at +20 mm, the ignition spot is close to the high ϕ zone at the top of FOV. This results in an asymmetric flame evolution preferentially towards the fuel-richer zone, stretched along the higher- ϕ ridge extending from the fuel-richer zone in the top-left corner towards the bottom-right side. The flame kernel spreads faster when igniting at +20 mm compared to other two ignition locations, which is in line with the locally higher ϕ near the ignition site.

The latest SOI at -60°CA shows the highest sensitivity of flame kernel evolution to ignition location, in agreement with the measured fuel distribution. When igniting at -25 mm, in the low- ϕ region, a rather slow initial kernel evolution was observed at 5°CA AIT, which resulted in a smaller flame by 10°AIT compared to other ignition locations. Conversely, when igniting at +20°mm, faster flame evolution than with central ignition location was observed, with a preferential direction towards the high ϕ zone on the intake side.

The flame centroids reveal only minor differences between a spark location -25 mm and 20 mm. Most of the SOIs show no or only little movement of the flame centroid within 10°CA. With a spark at -25 mm and an SOI of -90°CA it seems that the flame burns towards the intake side, but here the algorithm fails at later crank angles and the centroid of the flame moves with the bright flame front. The same happens for the flame movement with an SOI at -60°CA. At the +20 mm spark location and an SOI of -90°CA the flame moves towards the upper intake side of the FOV, contrary to an SOI of -60°CA where the flame burns more into a central position.

For completeness, Figure 55 in the appendix shows the same data as Figure 47 but for 20 bar injection pressure. Similar trends in the flame growth and movement are observed as for 40 bar injection pressure. For SOI of -60°CA, the grey-scale apparent discretization stems from the fact that more self-ignited and misfired cycles occurred, which were excluded here, decreasing the statistical basis.

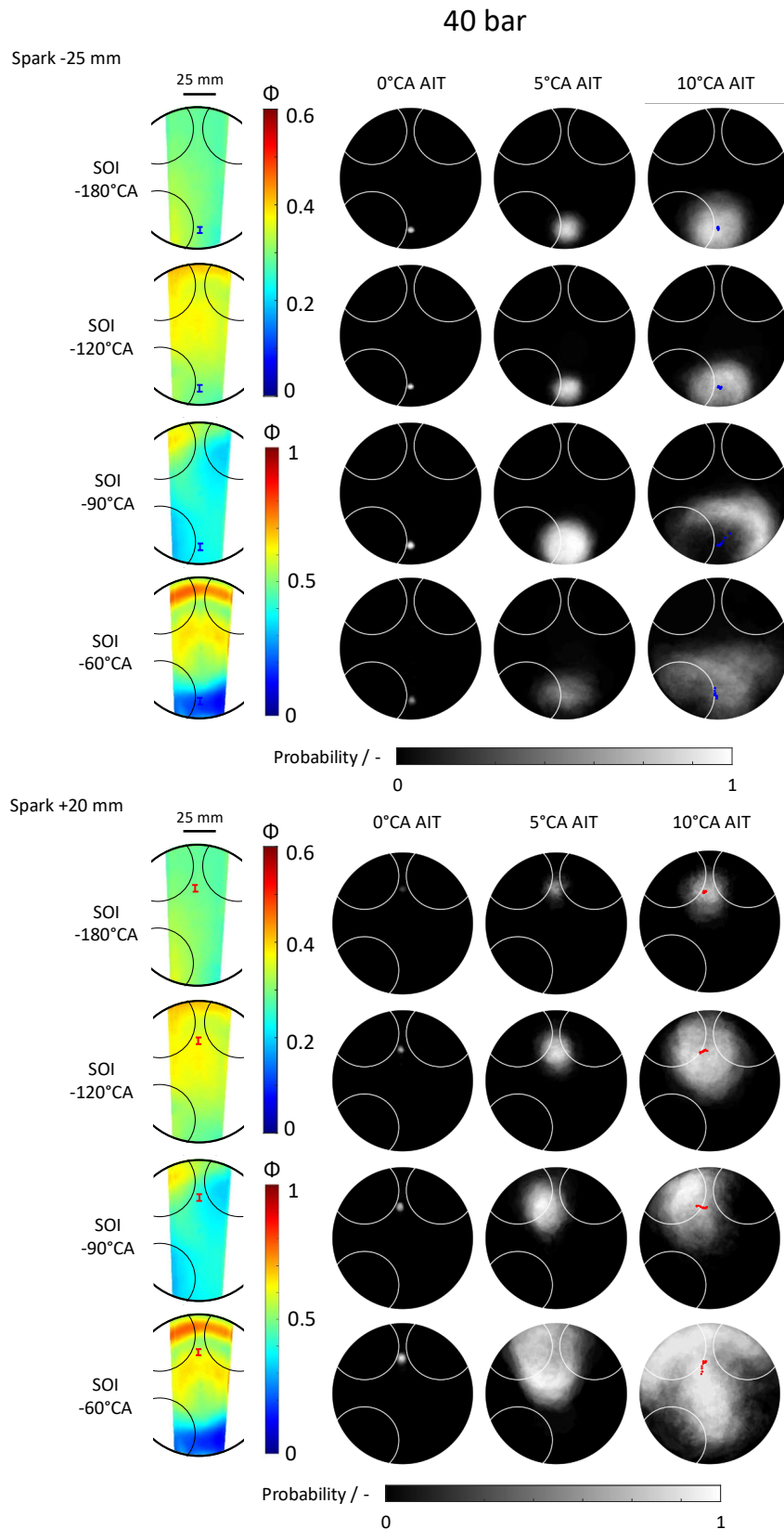


Figure 47. Average equivalence ratio and corresponding probability maps of detecting burnt zone for different injection timings at 40 bar injection pressure for the -25 mm ignition location (top) and the +20 mm ignition location (bottom). Additionally, the flame centroids from 0 to 10°CA AIT are marked in the burnt gas area 10°CA AIT.

Equivalent flame radius and heat release

This section seeks to establish correlations between the mixture distribution at spark timing, early flame kernel evolution, and global combustion properties like combustion duration and CCV. For this purpose, Figure 48 compares the evolution of equivalent flame radius to cumulative combustion heat release (CHR), representing the standard deviation of each metric as a shaded band around the mean trace.

With an SOI of -180°CA , the equivalent flame radius for all spark locations and both injection pressures slowly and almost linearly increases until 10 to 15°CA AIT , when the image segmentation algorithm becomes unreliable as discussed earlier. The central and -25 mm spark location have a similar initial flame speed, but as suggested by the corresponding cumulative heat release, this no longer applies after about 10°CA AIT . The -25 mm spark location yields the fastest combustion speed. Overall, the CHR trends match well with the initial flame evolution speed, which itself matches well with the local equivalence ratio for both injection pressures. The deviation between the CHR for central and $+20$ mm ignition locations between 10 - 30°CA AIT despite the comparable early kernel evolution may be due to geometrical constraints on flame evolution and/or the three-dimensionality of the process and locally-fluctuating equivalence ratio. When the flame burns through slightly richer zones, more heat is released, which may or may not show up in the flame radius.

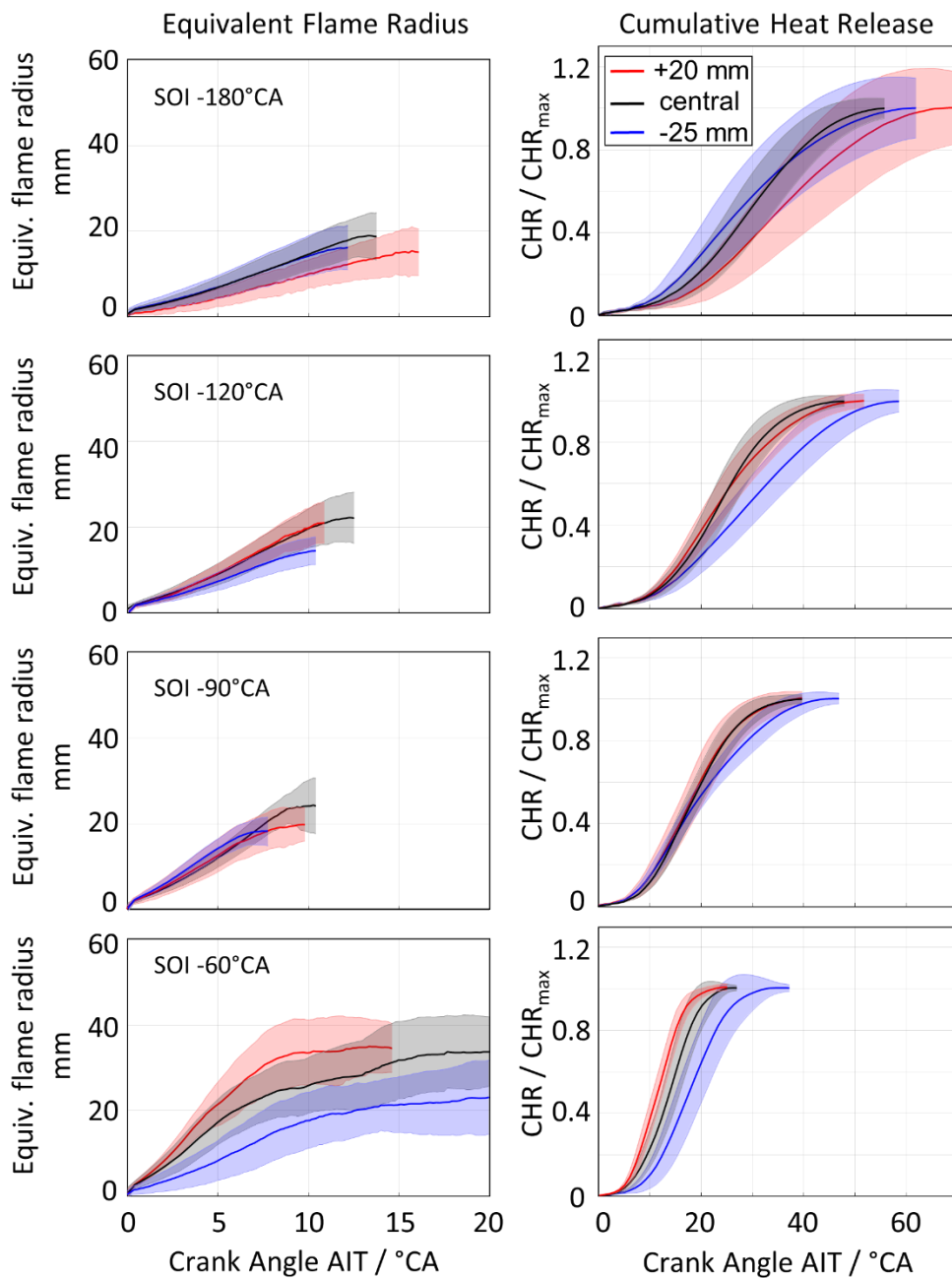
Retarding the injection timing to -120° increases the speed of combustion and changes the ignition locations that lead to fastest flame propagation, in line with a different equivalence ratio distribution at ignition. At both injection pressures, the equivalent flame radius shows nearly identical flame growth for central and $+20$ mm spark locations, while the flame at -25 mm spark location grows somewhat slower. The CHR shows only minor differences between the $+20$ mm and central spark location, and a slower combustion for spark at -25 mm.

An injection timing of -90°CA , the difference in early flame evolution between different ignition location is reduced. For an injection pressure of 40 bar, the flame growth between 0 and 8°CA is similar for the central and $+20$ mm spark location and slightly faster for -25 mm spark location. The corresponding CHRs reveal similar results. Also at 20 bar injection pressure, similar conclusions can be reached.

Retarding the injection timing to -60°CA yields for both injection pressures the fastest flame growth and heat release, but also higher CCV and differences between individual ignition locations. The fastest flame growth for 40 bar injection pressure can be found with the $+20$ mm spark location. This is also true for the corresponding CHR and is consistent with the LIF images, where most of the fuel at ignition timing is in the spark area. The spark location shifted -25 mm towards the exhaust has the slowest flame speed and a retarded heat release, which one would expect since the charge is very lean here at ignition. Decreasing the injection pressure to 20 bar results in even more CCV with standard deviations up to 10 mm for the equivalent flame radius. The fast flame growth with a central spark originates most likely from the ignition in the fuel jet.

With a more homogeneous mixture (early injection) the central and -25 mm spark location yield a more stable and faster flame development than the +20 mm spark locations. When the inhomogeneity in the mixture is increased for later injection timings, e.g., SOI = -90°CA, the heat release is not impacted as much by the spark location anymore, even though minor differences between the flame radii occur. The latest SOI at -60°CA shows that also an off-center spark location can reach even higher IMEP (Table 9) and faster flame growth than a central location, when most of the fuel is in the area around the spark. However, for all late injection timings the spark location shifted towards the exhaust has a negative impact on the combustion speed.

40 bar



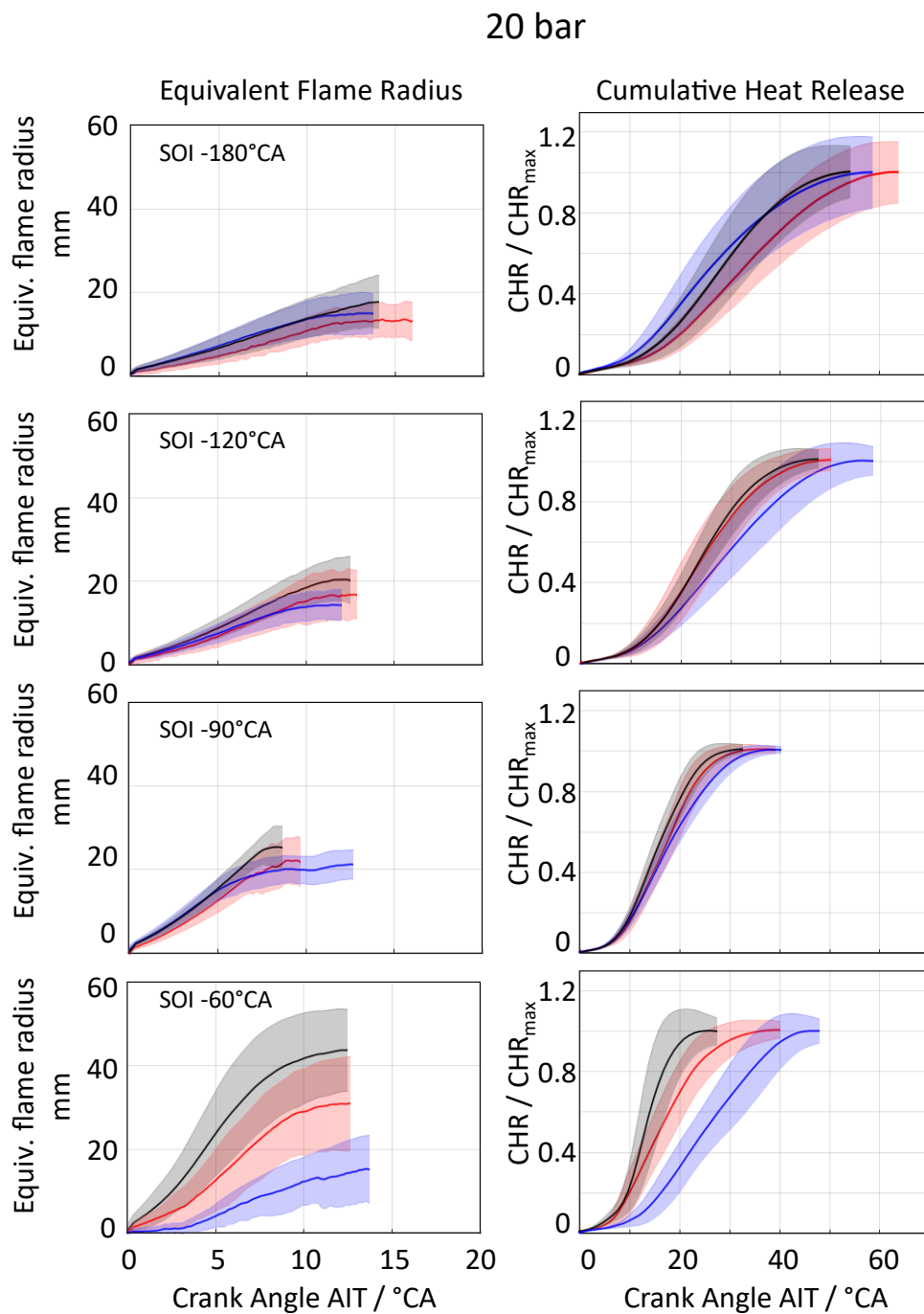


Figure 48. (First column) Equivalent flame radius vs. crank angle AIT at different injection timings for all ignition locations at 40 bar and 20 bar injection pressure. Corresponding cumulative heat release (CHR) are shown for 40 bar and 20 bar in the second column. Note that the crank angle plotting limits differ between flame radius and heat release plots.

Condensing Figure 48 to better compare the different cases among each other, Figure 49 plots the crank angle AIT at which the flame reaches a radius of 5 mm (CA 5 mm) versus that at which 50% of the mass fraction is burned (CA 50, sometimes termed “center of combustion”). This links the early flame evolution from optical diagnostics with the energetically relevant part of the combustion derived from the pressure traces.

Figure 49a shows the ensemble mean of each case. Consistent with Figure 48 and literature results for gasoline [8] and H₂ [114] SI, there is a strong positive correlation between the early flame kernel and the later main heat release. The spread along this correlation indicates the influence of each parameter variation. Interestingly, only the variation in SOI has any systematic influence along this correlation: For injection at -90°CA, 5 mm equivalent flame radius are typically reached within less than 2° and CA 50 within 20°CA AIT, while for injection at -180°CA it takes 5° and 30°CA, respectively. Injection at -120°CA yields intermediately fast early and main combustion. However, the earliest injection timing, -60°CA, does not follow this pattern. Here, the influence of ignition location is much more pronounced. In particular, for ignition at -25 mm it takes long to reach 5 mm radius, but 50% of the fuel mass is already burned 15° and 20°CA AIT for 40 and 20 bar injection pressure, respectively. This can be traced back to unfavorable mixture around the ignition spot at ignition timing, see bottom rows in Figure 47 and Figure 54. When the flame expands into the fuel-rich zones, the flame speed increases, and this leads most likely to the fast heat release indicated by the early CA 50. Conversely, for the earlier injection timings (-180° and -120°CA) and the ignition location of -25 mm, the equivalent flame radius of 5 mm is reached relatively quickly, but CA 50 late. This means that the conditions in the beginning of combustion are as good as for other spark locations, but during combustion the flame becomes slower as it encounters less favorable conditions.

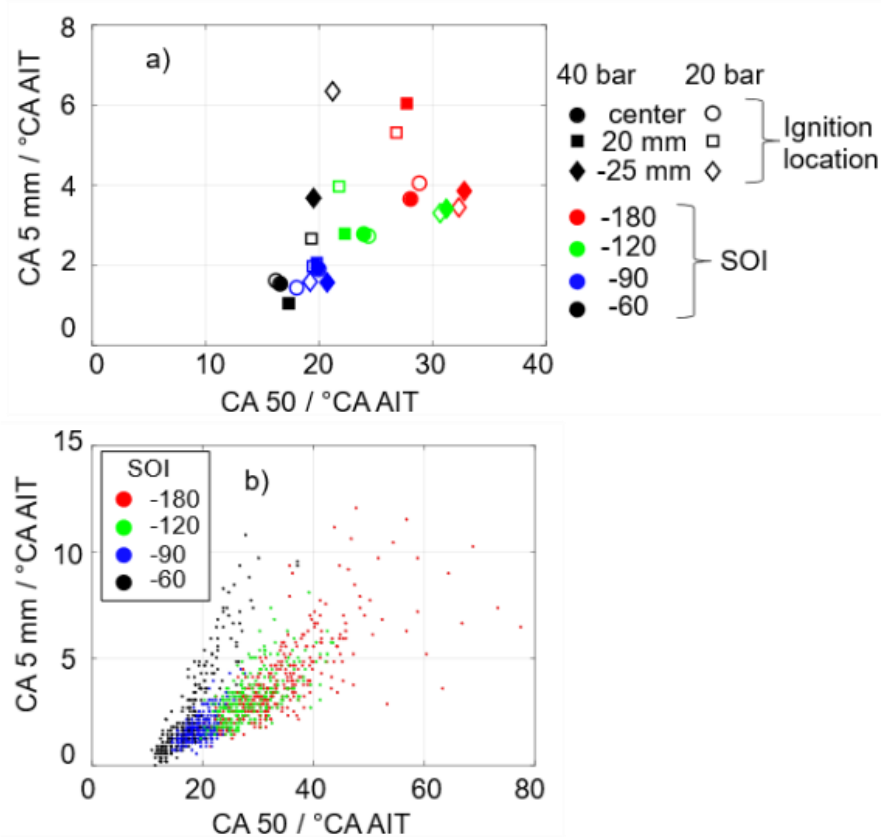


Figure 49. Crank angle AIT at which the flame radius reached 5 mm (CA 5 mm) vs. the crank angle AIT at which 50% of the mass is burned (CA 50). (a) Ensemble mean of each case and (b) single-cycle data, the latter differentiated only by SOI, aggregating all ignition locations and injection pressures. Note the wider plotting limits in (b).

Figure 49b shows the same data, but on a single-cycle basis. Here, the cases are color-coded by SOI regardless of injection pressure and ignition location. It can be seen that the variation between the cycles spreads the data similarly to the variation in SOI. This can be seen particularly well for SOI of -180°CA , where the multi-cycles average values in Figure 49a are nearly equidistant from the coordinate origin, but the cyclic variation shows a strong correlation between early flame propagation and main combustion, i.e., away from the origin. Again, the latest injection timing, -60°CA , is distinct. While data for the three earlier SOI scatter around a common linear trend, those from the latest SOI form a much steeper slope. This indicates that in most cycles ignition and early flame propagation finds relatively unfavorable conditions – maybe too rich or too lean or in very strong flow – but the overall state of the fuel-air mixture and turbulence is conducive to fast combustion.

So far, mainly the ensemble-average mixture distribution with the flame evolution is correlated. To see if the flame developments can be connected with the equivalence ratio at ignition timing on a single cycle basis, the next paragraph focuses on the correlation between those data sets.

Correlation maps

The correlation between the mixture field and the early flame propagation was analyzed in “correlation maps”, as suggested by [81]. Here, a scalar field quantity (here, ϕ in each pixel) is correlated with a single-valued quantity (here, the equivalent flame radius $r_{\text{flame}} 5^{\circ}\text{CA AIT}$). This results in the correlation maps shown in Figure 50. Plotted in false color is the local correlation coefficient, which is essentially the normalized covariance of the two metrics. Values close to 1 show a positive correlation, i.e., high equivalence ratio correlates with larger flame radius. Conversely, values close to -1 mean that a high equivalence ratio correlates with a small flame radius. With the given number of recorded cycles correlation values (nominally 80, but less when misfires or cycles with additional ignition spots were excluded) between -0.22 and 0.22 are not significant. The corresponding regions are blanked out in Figure 50.

In almost all cases the highest correlation coefficients can be found in the region around or near the spark location, as expected. For injection at -180° , -120° , and -90°CA , later injection tends to yield a smaller high-correlation region with lower peak values. While the former may be expected, since with later injection the mean equivalence ratio field is structured on a smaller scale (see Figure 46, Figure 47, Figure 54, and in the previous chapter 5.3.2), the latter may be somewhat surprising, since higher mean stratification could be expected to lead to a stronger correlation with the ensuing flame propagation. It is likely that the later injection timings increase the out-of-plane component of the flow and the mixture gradients, i.e., the two-dimensional LIF imaging is less representative of the actually three-dimensional spatial correlations.

The most fuel-homogeneous cases with an SOI of -180°CA yield similar results for both injection pressures for the central spark location and the -25 mm spark location. A region of higher correlation up to correlation coefficients of 0.6 can be found around the spark locations.

For the central spark location, the values in the remaining FOV are low, which means only the mixture near the spark impacts the early flame development. Sparking at -25 mm, a negative correlation coefficient of -0.4 is found on the left intake side of the FOV. This is likely just a result of a fuel-rich zone on the exhaust side leading to a fuel-lean zone near the intake, since the total amount of fuel is constant. Somewhat surprisingly, sparking at +20 mm results in a more spotted pattern of interchanging high and low correlation zones. One reason might be the smaller data set available for this spark location because of the large share of abnormal ignition events for this case. Another reason might be that the laser-ignition plasma quality varies more due to the longer pathway of the beam. The beam steering at the entry window might defocus the beam.

The highest correlation can be found around the ignition location for SOI = -60°CA, central spark position and 40 bar injection pressure. With 20 bar, the general level of correlation decreases, which is attributed to the injection event still ongoing at the imaging time. Here, ϕ at the ignition location is always high and therefore, combustion is less sensitive to variations in local ϕ . Surprisingly, no significant correlation can be found for SOI = -60°CA, 40 bar injection pressure, and -25 mm spark location. Also, with 20 bar injection pressure the corresponding cases with +20 mm spark location and both off-center spark locations show weak correlation between local mixture and flame kernel growth, likely due to strong out-of-plane flow and mixture gradients.

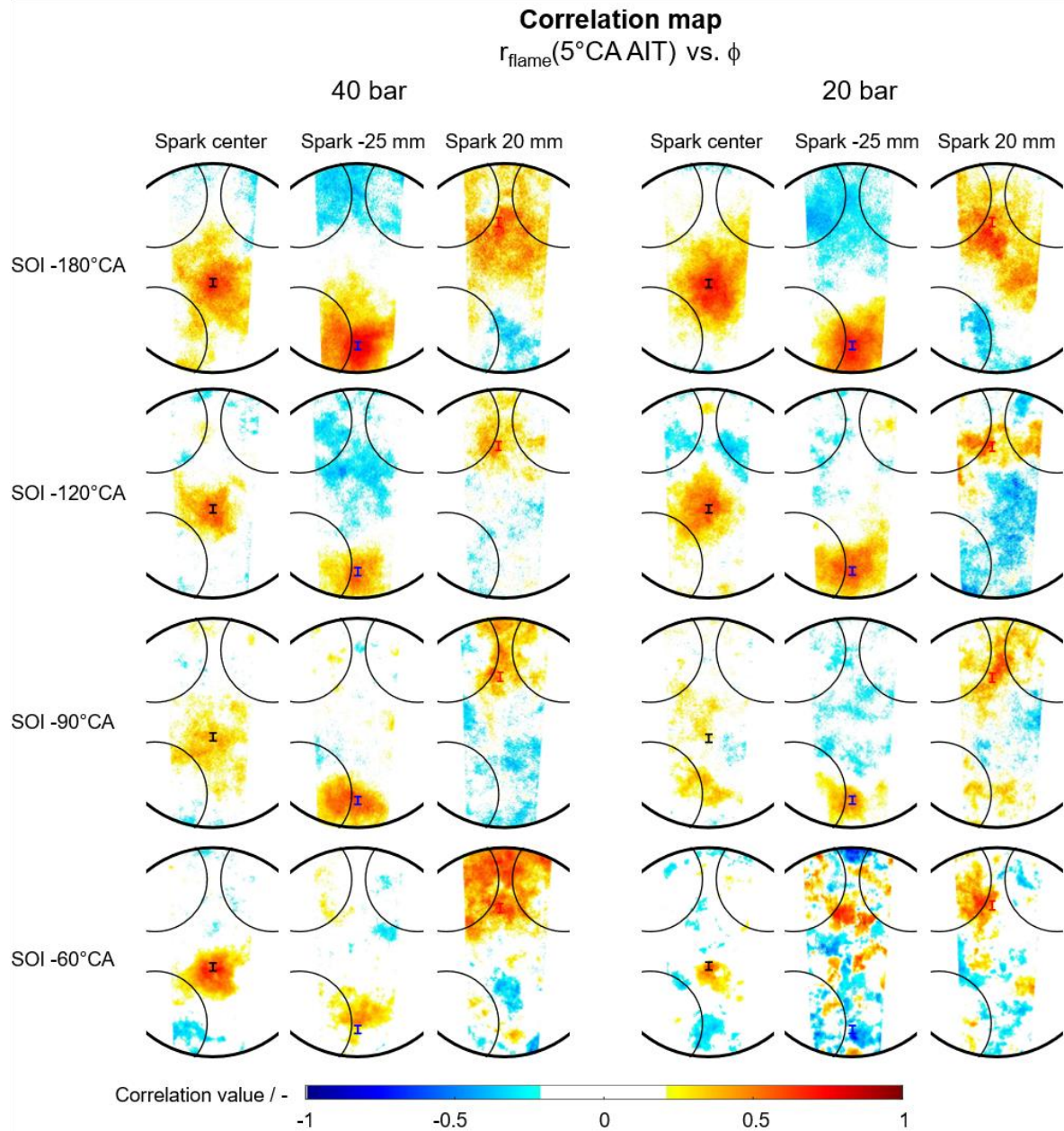


Figure 50. Correlation map of the equivalent flame radius 5°CA after ignition timing with the equivalence ratio at ignition. (Left three columns) 40 bar, (right three columns) 20 bar injection pressure. Statistically insignificant values are blanked.

6.4 Chapter conclusion

Mixing and combustion in an optically accessible heavy-duty engine with $\text{H}_2\text{-DI}$ from a centrally-mounted outward-opening hollow-cone injector was analyzed. Igniting the mixture by a focused laser beam allowed positioning the ignition at different locations. Laser-induced fluorescence imaging of anisole seeded into the fuel quantified the mixture state at ignition timing in a horizontal plane 14 mm below the fire deck – the plane in which the laser ignition

occurred. Varying the injection timing, pressure, and the ignition location, this study investigated the correlation between mixture formation and early flame propagation.

Disregarding cycles with misfires and additional, unintended laser-ignition spots, the COV of IMEP decreases with later injection timings. An analysis of the mixture formation showed that both late injection and decreased injection pressure increase mixture inhomogeneity in the ensemble average as well as deviations across cycles. Even though the in-cylinder flow field here is not measured, presumably increased mixture inhomogeneity correlates with increased large-scale flow and turbulence. Since later injection also significantly shortened combustion, the conclusion is that in these experiments the beneficial effect of increased turbulence dominates the presumably detrimental effect of mixture inhomogeneity.

For the central and -25 mm spark location and most SOIs the flame remains centered around the spark location and does not move towards any particular direction. For the +20 mm spark location the flame burns slightly towards fuel-richer zones. Across all cases, however, it was surprisingly difficult to establish a relation between the mean preferred propagation direction of the flame and the mean mixture distribution at the time of ignition. This is not because the equivalence ratio was only measured at a single crank angle – in fact, for the cases where images 10°CA later were available, the mean mixture distribution had not changed much. Thus, it appears that in particular for late injection the three-dimensionality of the mixture and the flow complicate interpretations that are based on the planar, two-dimensional equivalence ratio measurement.

For almost all cases, a faster early flame kernel growth corresponds to faster heat release and shorter combustion. This is consistent with investigations in both hydrocarbon and H₂-fueled SI engines [58,114,145]. Over the range in which each parameter – injection timing, injection pressure, and ignition location – was varied, the injection timing impacts the combustion speed the most. The effect of CCV was similar to that of varying the injection timing in that both yield a strong correlation between early flame propagation and later energetically relevant combustion.

Even though in the *mean* and on a longer spatial scale equivalence ratio and flame propagation were difficult to correlate, this was mostly not the case on a *single-cycle* basis and closer distances. The equivalent flame radius 5°CA AIT with the equivalence ratio fields is correlated in that same cycle across each data set, yielding correlation maps. For ignition in the center and at -25 mm, the highest positive correlation coefficient is found around the ignition location, as expected. For a globally lean mixture, more fuel at the ignition location results in a higher flame speed, thus faster early flame propagation. However, for the +20 mm ignition location, the correlation is weaker and spatially less homogeneous. This indicates that fluctuations in the early flame kernel are due to a source different from fluctuations in the equivalence ratio, which might be the gradient-induced steering of the laser-ignition beam, which is stronger for locations farther from the entry window.

7 Conclusions and future work

The four studies presented above investigated flow behavior, injection strategies, mixture formation and flame propagation to understand the fundamental causal chain leading to combustion CCV.

First, optical imaging techniques were employed to examine the CCV of the early flame development in an optically accessible light-duty SI engine fueled with liquid iso-octane. Operating conditions with PFI as well as with DI were investigated. The research utilized conditional averaging of image data and correlation maps to show trends in the flame behavior. For PFI, slow cycles tended to burn towards the intake side of the spark plug, whereas DI exhibited a preference for burning towards the exhaust side. Interestingly, faster cycles exhibited increased variability in flame location but generally centered around the spark plug. Furthermore, the flow field analysis revealed shifts in vortex centers, particularly with PFI, demonstrating the critical role of in-cylinder flow dynamics. Moreover, correlation maps indicated regions with predictive influence on the combustion process, often deviating from the location of the tumble vortex center. In the case of DI, the equivalence ratio was correlated with CA10, emphasizing the significance of the mixture gradient in influencing combustion behavior.

The correlation between the flow field and the combustion speed was further investigated via ICA. Experimentally, the two in-plane components of the velocity are measured in the central cylinder plane by high-speed PIV with the engine running slightly lean at 1500 rpm in skip-fired mode. In 213 cycles, measurements are made during the late compression stroke before ignition with approximately 1° crank angle temporal resolution. ICA then decomposes the set of 213 flow fields at each time step, yielding a set of “source” flow patterns – the independent components (ICs). The temporal coherence between the ICs is then examined in a persistence analysis, comparing each IC with the one from the previous time step starting at ignition timing and going backwards in time. The results show which ICs persist how long throughout the compression stroke. To investigate the link between the ICs and combustion, CA10 in each cycle is correlated with the extent to which a given IC can be found in each flow field. The most persistent IC can be traced over more than half of the 70 degrees crank angle over which images were acquired. The IC that correlates best with CA10 visually more resembles some of the flow features found in conditional averaging of fast-burning versus slow-burning cycles.

In the second half of this work the liquid fuel was replaced by H₂ and the test facility used was a heavy-duty optical engine with a diesel-type combustion chamber. With this configuration the in-cylinder mixture formation of H₂ injected from a centrally-mounted hollow-cone injector was investigated under motored operation. LIF imaging was employed to evaluate the state of the mixture at the end of the compression stroke, focusing on the effects of injection timing and injection pressure on mixture inhomogeneity and repeatability of fuel distribution. As anticipated, retarding the injection timing and decreasing injection pressure resulted in increased mixture inhomogeneity and CCV in specific regions of the combustion chamber. The

study indicated that injection during the intake stroke or at BDC generated a more homogeneous mixture, while later injections, such as at -90°CA and -60°CA , exhibited a radially asymmetric mixture distribution with significant CCV. This variability could lead to localized NO_x production and increased cyclic combustion variation in a fired engine, depending on the spark plug's location within the chamber. The findings suggest that earlier injection timings are more likely to produce less NO_x emissions.

In the same test facility, a subsequent study was performed under fired operation, focusing on the correlation between mixture formation and early flame propagation. The research revealed that later injection timings, despite increasing mixture inhomogeneity in the ensemble average and deviations across cycles, led to a decrease in the COV of IMEP. The findings suggest that the benefits of increased turbulence associated with later injections outweigh the drawbacks of mixture inhomogeneity in the given experimental conditions. Moreover, variations in flame propagation direction were challenging to correlate with the mean mixture distribution at the time of ignition, particularly for late injections, emphasizing the complexities of three-dimensional mixture interactions and flow patterns. Here, injection timing emerged as the most influential parameter impacting combustion speed across the range of variations studied.

Future work

An important goal is the joint analysis of simulations for a more complete explanation and evaluation of experimental results. In all experiments presented in this work, only a two-dimensional plane of the flow field and/or mixture distribution is measured. The application of analysis methods, such as correlation maps and ICA, to three-dimensional data from numerical simulations could potentially address the limitations identified in this work related to two dimensionality. These methods need to be further extended to trace the causal chain of CCV back to its causes.

In the initial attempt to apply ICA to experimentally measured flow fields for investigating CCV, it was found that the combination of ICA and the current implementation of the persistence analysis does not provide a direct indication of how any presumed underlying reorganization of the flow occurs. To comprehensively characterize how ICA may be used for the purpose of investigating CCV, a broader range of conditions and engine configurations needs to be studied. This would also help to develop guidelines for best practices, similar to what has been done for POD [90,91].

The use of H₂ as a fuel is still relatively new, and on the methodological side, one goal is the further development of spatio-temporally resolved diagnostics. For example, schlieren measurement techniques can be useful in order to visualize the near-nozzle H₂ jet and the early flame propagation across the respective density gradients. The former answers the question to what details the near injection can be visualized in an engine. To use the schlieren technique within the cylinder with its round, thick quartz glass lining, the significant astigmatism of the optical system must be corrected using specially designed cylindrical lenses. Using tracer LIF in H₂-fueled engines assumes implicitly that the Reynolds number in the intake and

compression stroke is high enough to neglect differences in diffusivity. Verifying this experimentally is challenging. Therefore, this question needs to be investigated in simulations with detailed transport.

One limitation of the studies on CCV in the H₂-fueled heavy-duty engine from Sandia National Laboratories was the lack of information about the flow field. The observed asymmetry and CCV of the fuel distribution are attributed to factors such as the piston-bowl cutout and in-cylinder bulk flow dynamics, showing the need for further research into flow-field interactions and eddy structures. Additionally, improvements in quantification techniques and corrections for factors such as light absorption would lead to more accurate measurements.

7 Bibliography

7.1 References

- [1] *Verkehr belastet Luft und Klima - Minderungsziele der Bundesregierung*, Umwelt Bundesamt, available at <<https://www.umweltbundesamt.de/daten/verkehr/emissionendes-verkehrs#verkehr-belastet-luft-und-klima-minderungsziele-der-bundesregierung>>, accessed 18/10/23.
 - [2] J. Hardler, R. Szengel, H. Middendorf, A. Kuphal, W. Siebert, L. Hentschel (Eds.), *Minimaler Verbrauch - Maximale Kraft TSI Technik im neuen 1.2l Motor von Volkswagen*, 30. Internationales Wiener Motorensymposium, May 07-08, No. 697 in Fortschritt-Berichte VDI, VDI Verlag, Düsseldorf, 2009.
 - [3] P. Lückert, F. Kreitmann, N. Merdes, R. Weller, A. Rehberger, K. Bruchner, K. Schwedler (Eds.), *Der neue 1,8l 4-Zylinder Turbo-Direkteinspritz-Ottomotor für alle PKW mit Standardantrieb von Mercedes-Benz*, 30. Internationales Wiener Motorensymposium, May 07-08, No. 697 in Fortschritt-Berichte VDI, VDI Verlag, Düsseldorf, 2009.
 - [4] F. Steinparzer, H. Unger, T. Brüner, D. Kannenberg (Eds.), *Der neue BMW 2,0l 4-Zylinder Ottomotor mit Twin Power Turbo Technologie*, 32. Internationales Wiener Motorensymposium, May 05-06, No. 735 in Fortschritt-Berichte VDI, VDI Verlag, Düsseldorf, 2011.
 - [5] J.B. Heywood, *Internal combustion engine fundamentals*, McGraw-Hill Education, New York, 2018.
 - [6] R. van Basshuysen, *Ottomotor mit Direkteinspritzung und Direkteinblasung*, Springer Fachmedien Wiesbaden, Wiesbaden, 2017.
 - [7] G.P. Merker, R. Teichmann, *Grundlagen Verbrennungsmotoren*, Springer Fachmedien Wiesbaden, Wiesbaden, 2019.
 - [8] P.G. Aleiferis, A. Taylor, K. Ishii, Y. Urata, *The nature of early flame development in a lean-burn stratified-charge spark-ignition engine*, Combustion and Flame 136 (3):283–302, 2004.
 - [9] P.G. Aleiferis, Taylor, A. M. K. P., J.H. Whitelaw, K. Ishii, Y. Urata, *Cyclic Variations of Initial Flame Kernel Growth in a Honda VTEC-E Lean-Burn Spark-Ignition Engine*, SAE Technical Paper 2000-01-1207, 2000.
 - [10] R.N. Dahms, M.C. Drake, T.D. Fansler, T.-W. Kuo, N. Peters, *Understanding ignition processes in spray-guided gasoline engines using high-speed imaging and the extended spark-ignition model SparkCIMM*, Combustion and Flame 158 (11):2245–2260, 2011.
 - [11] V. Sick, *High speed imaging in fundamental and applied combustion research*, Proceedings of the Combustion Institute 34 (2):3509–3530, 2013.
 - [12] X. Li, M. Soteriou, *High-Fidelity Simulation Of Fuel Atomization In A Realistic Swirling Flow Injector*, Atomization and Sprays 23 (11):1049–1078, 2013.
-

-
- [13] F.-X. Demoulin, J. Reveillon, B. Duret, Z. Bouali, P. Desjonqueres, T. Menard, *Toward Using Direct Numerical Simulation To Improve Primary Break-Up Modeling*, *Atomization and Sprays* 23 (11):957–980, 2013.
- [14] M. Bode, T. Falkenstein, H. Pitsch, T. Kimijima, H. Taniguchi, T. T. Arima (Eds.), *Numerical study on the impact of cavitation on the spray development processes for GDI injection*, 13th Triennial ILASS, Taiwan, August 23-27, Taiwan, 2015.
- [15] M. Buschbeck, N. Bittner, T. Halfmann, S. Arndt, *Dependence of combustion dynamics in a gasoline engine upon the in-cylinder flow field, determined by high-speed PIV*, *Experiments in Fluids* 53 (6):1701–1712, 2012.
- [16] W. Zeng, M. Sjöberg, D.L. Reuss, *Combined effects of flow/spray interactions and EGR on combustion variability for a stratified DISI engine*, *Proceedings of the Combustion Institute* 35 (3):2907–2914, 2015.
- [17] W. Zeng, S. Keum, T.-W. Kuo, V. Sick, *Role of large scale flow features on cycle-to-cycle variations of spark-ignited flame-initiation and its transition to turbulent combustion*, *Proceedings of the Combustion Institute* 37 (4):4945–4953, 2019.
- [18] J. Bode, J. Schorr, C. Krüger, A. Dreizler, B. Böhm, *Influence of three-dimensional in-cylinder flows on cycle-to-cycle variations in a fired stratified DISI engine measured by time-resolved dual-plane PIV*, *Proceedings of the Combustion Institute* 36 (3):3477–3485, 2017.
- [19] J. Bode, J. Schorr, C. Krüger, A. Dreizler, B. Böhm, *Influence of the in-cylinder flow on cycle-to-cycle variations in lean combustion DISI engines measured by high-speed scanning-PIV*, *Proceedings of the Combustion Institute* 37 (4):4929–4936, 2019.
- [20] D. Dreher, M. Schmidt, C. Welch, S. Ourza, S. Zündorf, J. Maucher, S. Peters, A. Dreizler, B. Böhm, A. Hanuschkin, *Deep feature learning of in-cylinder flow fields to analyze cycle-to-cycle variations in an SI engine*, *International Journal of Engine Research* 22 (11):3263–3285, 2021.
- [21] O. Colin, A. Benkenida, C. Angelberger, *3d Modeling of Mixing, Ignition and Combustion Phenomena in Highly Stratified Gasoline Engines*, *Oil & Gas Science and Technology - Rev. IFP* 58 (1):47–62, 2003.
- [22] F. Cavallo M., T. Ma, A.M. Kempf, *Large eddy simulations of the Darmstadt turbulent stratified flame series*, *Proceedings of the Combustion Institute* 34 (1):1307–1315, 2013.
- [23] F. Proch, A.M. Kempf, *Numerical analysis of the Cambridge stratified flame series using artificial thickened flame LES with tabulated premixed flame chemistry*, *Combustion and Flame* 161 (10):2627–2646, 2014.
- [24] F. Seffrin, F. Fuest, D. Geyer, A. Dreizler, *Flow field studies of a new series of turbulent premixed stratified flames*, *Combustion and Flame* 157 (2):384–396, 2010.
- [25] M.S. Sweeney, S. Hochgreb, M.J. Dunn, R.S. Barlow, *The structure of turbulent stratified and premixed methane/air flames I: Non-swirling flows*, *Combustion and Flame* 159 (9):2896–2911, 2012.
-

-
- [26] J.B. Ghandhi, F.V. Bracco, *Mixture Preparation Effects on Ignition and Combustion in a Direct-Injection Spark-Ignition Engine*, SAE Technical Paper 962013, 1996.
- [27] T. Fujikawa, Y. Nomura, Y. Hattori, T. Kobayashi, M. Kanda, *Analysis of cycle-by-cycle variation in a direct injection gasoline engine using a laser-induced fluorescence technique*, International Journal of Engine Research 4 (2):143–153, 2003.
- [28] T.D. Fansler, M.C. Drake, B. Stojkovic, M.E. Rosalik, *Local fuel concentration, ignition and combustion in a stratified charge spark combustion in a stratified charge spark ignited direct injection engine: Spectroscopic, imaging and pressure-based measurements*, International Journal of Engine Research 4 (2):61–86, 2003.
- [29] T.D. Fansler, D.T. French, M.C. Drake, *Fuel Distributions in a Firing Direct-Injection Spark-Ignition Engine Using Laser-Induced Fluorescence Imaging*, SAE Technical Paper 950110, 1995.
- [30] F. Zhao, M.-C. Lai, D. Harrington, *Automotive spark-ignited direct-injection gasoline engines*, Progress in Energy and Combustion Science 25 (5):437–562, 1999.
- [31] J.D. Smith, V. Sick, *Factors Influencing Spark Behavior in a Spray-Guided Direct-Injected Engine*, SAE Technical Paper 2006-01-3376, 2006.
- [32] B. Peterson, V. Sick, *High-Speed Flow and Fuel Imaging Study of Available Spark Energy in a Spray-Guided Direct-Injection Engine and Implications on Misfires*, International Journal of Engine Research 11 (5):313–329, 2010.
- [33] B. Peterson, D.L. Reuss, V. Sick, *High-speed imaging analysis of misfires in a spray-guided direct injection engine*, Proceedings of the Combustion Institute 33 (2):3089–3096, 2011.
- [34] E. Pomraning, K. Richards, P.K. Senecal, *Modeling Turbulent Combustion Using a RANS Model, Detailed Chemistry, and Adaptive Mesh Refinement* SAE Technical Paper 2014-01-1116, 2014.
- [35] R. Scarcelli, K. Richards, E. Pomraning, P.K. Senecal, T. Wallner, J. Sevik, *Cycle-to-Cycle Variations in Multi-Cycle Engine RANS Simulations* SAE Technical Paper 2016-01-0593, 2016.
- [36] C. Hasse, V. Sohm, B. Durst, *Numerical investigation of cyclic variations in gasoline engines using a hybrid URANS/LES modeling approach*, Computers & Fluids 39 (1):25–48, 2010.
- [37] D. Goryntsev, A. Sadiki, J. Janicka, *Analysis of misfire processes in realistic Direct Injection Spark Ignition engine using multi-cycle Large Eddy Simulation*, Proceedings of the Combustion Institute 34 (2):2969–2976, 2013.
- [38] S. Fontanesi, A. d’Adamo, C.J. Rutland, *Large-Eddy simulation analysis of spark configuration effect on cycle-to-cycle variability of combustion and knock*, International Journal of Engine Research 16 (3):403–418, 2015.
-

-
- [39] K. Truffin, C. Angelberger, S. Richard, C. Pera, *Using large-eddy simulation and multivariate analysis to understand the sources of combustion cyclic variability in a spark-ignition engine*, *Combustion and Flame* 162 (12):4371–4390, 2015.
- [40] S. Wadekar, P. Janas, M. Oevermann, *Large-eddy simulation study of combustion cyclic variation in a lean-burn spark ignition engine*, *Applied Energy* 255:113812, 2019.
- [41] S.H.R. Müller, B. Böhm, M. Gleißner, R. Grzeszik, S. Arndt, A. Dreizler, *Flow field measurements in an optically accessible, direct-injection spray-guided internal combustion engine using high-speed PIV*, *Experiments in Fluids* 48 (2):281–290, 2010.
- [42] W. Zeng, M. Sjöberg, D.L. Reuss, Z. Hu, *High-speed PIV, spray, combustion luminosity, and infrared fuel-vapor imaging for probing tumble-flow-induced asymmetry of gasoline distribution in a spray-guided stratified-charge DISI engine*, *Proceedings of the Combustion Institute* 36 (3):3459–3466, 2017.
- [43] A.A. Adamczyk, L. Rimai, *2-Dimensional particle tracking velocimetry (PTV): Technique and image processing algorithms*, *Experiments in Fluids* 6 (6):373–380, 1988.
- [44] M. Shimura, S. Yoshida, K. Osawa, Y. Minamoto, T. Yokomori, K. Iwamoto, M. Tanahashi, H. Kosaka, *Micro particle image velocimetry investigation of near-wall behaviors of tumble enhanced flow in an internal combustion engine*, *International Journal of Engine Research* 20 (7):718–725, 2019.
- [45] M. Schmidt, C.-P. Ding, B. Peterson, A. Dreizler, B. Böhm, *Near-Wall Flame and Flow Measurements in an Optically Accessible SI Engine*, *Flow, Turbulence and Combustion* 106 (2):597–611, 2021.
- [46] L. Rao, S. Kook, *Optimisation of Image Processing Parameters for Flame Image Velocimetry (FIV) Measurement in a Single-Cylinder, Small-Bore Optical Diesel Engine*, *SAE International Journal of Advances and Current Practices in Mobility* 1 (3):1311–1324, 2019.
- [47] Z. Sun, S. Yang, M. Nour, X. Li, D. Hung, M. Xu, *Significant Impact of Flash Boiling Spray on In-Cylinder Soot Formation and Oxidation Process*, *Energy & Fuels* 34 (8):10030–10038, 2020.
- [48] M. Cui, Z. Sun, M. Xu, D. Hung, X. Li, in: *ASME 2020 Internal Combustion Engine Division Fall Technical Conference*, ASME 2020 Internal Combustion Engine Division Fall Technical Conference, Virtual, Online, 04-Nov-20 - 06-Nov-20, American Society of Mechanical Engineers, 2020.
- [49] S.A. Kaiser, C.M. White, *PIV and PLIF to Evaluate Mixture Formation in a Direct-Injection Hydrogen-Fuelled Engine*, *SAE International Journal of Engines* 1 (1):657–668, 2009.
- [50] P. Kranz, D. Fuhrmann, M. Goschütz, S. Kaiser, S. Bauke, K. Golibrzuch, H. Wackerbarth, P. Kawelke, J. Luciani, L. Beckmann, J. Zachow, M. Schuette, O. Thiele, T. Berg, *In-Cylinder LIF Imaging, IR-Absorption Point Measurements, and a CFD Simulation to Evaluate Mixture Formation in a CNG-Fueled Engine*, *SAE International Journal of Engines* 11 (6):1221–1238, 2018.
-

-
- [51] J. Reboux, D. Puechberty, F. Dionnet, *A New Approach of Planar Laser Induced Fluorescence Applied to Fuel/Air Ratio Measurement in the Compression Stroke of an Optical S.I. Engine*, SAE Technical Paper 941988, 1994.
- [52] V.M. Salazar, S.A. Kaiser, *An Optical Study of Mixture Preparation in a Hydrogen-fueled Engine with Direct Injection Using Different Nozzle Designs*, SAE International Journal of Engines 2 (2):119–131, 2009.
- [53] M. Schütte, H. Finke, G. Grünefeld, S. Krüger, P. Andresen, B. Stiebels, B. Block, H. Meyer, W. Hentschel, *Spatially Resolved Air–Fuel Ratio and Residual Gas Measurements by Spontaneous Raman Scattering in a Firing Direct Injection Gasoline Engine*, SAE Technical Paper 2000-01-1795, 2000.
- [54] J. Manin, L.M. Pickett, S.A. Skeen, J.H. Frank, *Image processing methods for Rayleigh scattering measurements of diesel spray mixing at high repetition rate*, Applied Physics B 127 (5), 2021.
- [55] C. Espey, J.E. Dec, T.A. Litzinger, D.A. Santavicca, *Planar laser rayleigh scattering for quantitative vapor-fuel imaging in a diesel jet*, Combustion and Flame 109 (1-2):65–86, 1997.
- [56] C.M. Fajardo, J.D. Smith, V. Sick, *PIV, high-speed PLIF and chemiluminescence imaging for near-spark-plug investigations in IC engines*, Journal of Physics: Conference Series 45:19–26, 2006.
- [57] Y. Liu, J. Tan, M. Wan, X. Yao, *OH* and CH* chemiluminescence characteristics in low swirl methane-air flames*, AIP Advances 10 (5), 2020.
- [58] P.G. Aleiferis, M.F. Rosati, *Flame chemiluminescence and OH LIF imaging in a hydrogen-fuelled spark-ignition engine*, International Journal of Hydrogen Energy 37 (2):1797–1812, 2012.
- [59] B. Peterson, E. Baum, A. Dreizler, B. Böhm, *An experimental study of the detailed flame transport in a SI engine using simultaneous dual-plane OH-LIF and stereoscopic PIV*, Combustion and Flame 202:16–32, 2019.
- [60] M. Raffel, C.E. Willert, F. Scarano, C.J. Kähler, S.T. Wereley, J. Kompenhans, *Particle Image Velocimetry*, Springer International Publishing, Cham, 2018.
- [61] M. Sauer, J. Hofkens, J. Enderlein, *Handbook of fluorescence spectroscopy and imaging: From single molecules to ensembles / Markus Sauer, Johan Hofkens, Jörg Enderlein*, Wiley-VCH, Weinheim, 2011.
- [62] J.L. Kinsey, *Laser-Induced Fluorescence*, Annual Review of Physical Chemistry 28 (1):349–372, 1977.
- [63] C. Schulz, V. Sick, *Tracer-LIF diagnostics: quantitative measurement of fuel concentration, temperature and fuel/air ratio in practical combustion systems*, Progress in Energy and Combustion Science 31 (1):75–121, 2005.
- [64] C. Tropea, A.L. Yarin, J.F. Foss, *Springer handbook of experimental fluid mechanics*, Springer, Berlin, 2007.
-

-
- [65] W. Koban, J.D. Koch, R.K. Hanson, C. Schulz, *Toluene LIF at elevated temperatures: implications for fuel–air ratio measurements*, Applied Physics B 80 (2):147–150, 2005.
- [66] M. Lackner, Á. Palotás, F. Winter, *Combustion: From basics to applications*, Wiley-VCH, Weinheim, 2013.
- [67] M.I. Najafabadi, L. Egelmeers, B. Somers, N. Deen, B. Johansson, N. Dam, *The influence of charge stratification on the spectral signature of partially premixed combustion in a light-duty optical engine*, Applied Physics B 123 (4), 2017.
- [68] B.D. Stojkovic, T.D. Fansler, M.C. Drake, V. Sick, *High-speed imaging of OH* and soot temperature and concentration in a stratified-charge direct-injection gasoline engine*, Proceedings of the Combustion Institute 30 (2):2657–2665, 2005.
- [69] P.C. Miles, in: *Volume 2: Instrumentation, Controls, and Hybrids; Numerical Simulation; Engine Design and Mechanical Development; Keynote Papers*, ASME 2014 Internal Combustion Engine Division Fall Technical Conference, Columbus, Indiana, USA, 19-Oct-14 - 22-Oct-14, American Society of Mechanical Engineers, 2014.
- [70] H. Zhao, *Laser diagnostics and optical measurement techniques in internal combustion engines*, SAE International, Warrendale, PA, 2012.
- [71] H.J. Eichler, J. Eichler, *Laser: Bauformen, Strahlführung, Anwendungen*, Springer Vieweg, Berlin, Heidelberg, 2015.
- [72] W. Demtröder, *Laserspektroskopie: Grundlagen und Techniken*, 5th ed., Springer, Berlin [etc.], 2007.
- [73] *IRO X Intensified Relay Optics*, LaVision GmbH, Product Manual, p. 11-16, 2022.
- [74] J. Laichter, S.A. Kaiser, *Optical Investigation of the Influence of In-cylinder Flow and Mixture Inhomogeneity on Cyclic Variability in a Direct-Injection Spark Ignition Engine*, Flow, Turbulence and Combustion, 2022.
- [75] M. Mansour, N. Peters, L.U. Schrader, *Experimental study of turbulent flame kernel propagation*, Experimental Thermal and Fluid Science 32 (7):1396–1404, 2008.
- [76] N. Ozdor, M. Dulger, E. Sher, *Cyclic Variability in Spark Ignition Engines A Literature Survey*, SAE Technical Paper 940987, 1994.
- [77] B. Peterson, D.L. Reuss, V. Sick, *On the ignition and flame development in a spray-guided direct-injection spark-ignition engine*, Combustion and Flame 161 (1):240–255, 2014.
- [78] A. Hanuschkin, S. Zündorf, M. Schmidt, C. Welch, J. Schorr, S. Peters, A. Dreizler, B. Böhm, *Investigation of cycle-to-cycle variations in a spark-ignition engine based on a machine learning analysis of the early flame kernel*, Proceedings of the Combustion Institute 38 (4):5751–5759, 2021.
- [79] C. Fajardo, V. Sick, *Flow field assessment in a fired spray-guided spark-ignition direct-injection engine based on UV particle image velocimetry with sub crank angle resolution*, Proceedings of the Combustion Institute 31 (2):3023–3031, 2007.
-

-
- [80] S. Einecke, C. Schulz, V. Sick, *Measurement of temperature, fuel concentration and equivalence ratio fields using tracer LIF in IC engine combustion*, Applied Physics B 71 (5):717–723, 2000.
- [81] R. Stiehl, J. Bode, J. Schorr, C. Krüger, A. Dreizler, B. Böhm, *Influence of intake geometry variations on in-cylinder flow and flow–spray interactions in a stratified direct-injection spark-ignition engine captured by time-resolved particle image velocimetry*, International Journal of Engine Research 17 (9):983–997, 2016.
- [82] S. Shawal, M. Goschutz, M. Schild, S. Kaiser, M. Neurohr, J. Pfeil, T. Koch, *High-Speed Imaging of Early Flame Growth in Spark-Ignited Engines Using Different Imaging Systems via Endoscopic and Full Optical Access*, SAE International Journal of Engines 9 (2):704–718, 2016.
- [83] M. Holický, *Introduction to Probability and Statistics for Engineers*, 1st ed., Springer Berlin Heidelberg; Imprint: Springer, Berlin Heidelberg, 2013.
- [84] J. Borée, S. Maurel, R. Bazile, *Disruption of a compressed vortex*, Physics of Fluids 14 (7):2543, 2002.
- [85] J. Laichter, P. Kranz, S.A. Kaiser, *Statistical analysis of flow field variations via independent component analysis*, Experiments in Fluids, 2024.
- [86] D.L. Reuss, *Cyclic Variability of Large-Scale Turbulent Structures in Directed and Undirected IC Engine Flows*, SAE Technical Paper 2000-01-0246, 2000.
- [87] J. Borée, *Extended proper orthogonal decomposition: a tool to analyse correlated events in turbulent flows*, Experiments in Fluids 35 (2):188–192, 2003.
- [88] H. Chen, D.L. Reuss, V. Sick, *Analysis of misfires in a direct injection engine using proper orthogonal decomposition*, Experiments in Fluids 51 (4):1139–1151, 2011.
- [89] K. Liu, D.C. Haworth, *Development and Assessment of POD for Analysis of Turbulent Flow in Piston Engines*, SAE Technical Paper 2011-01-0830, 2011.
- [90] H. Chen, D.L. Reuss, D.L.S. Hung, V. Sick, *A practical guide for using proper orthogonal decomposition in engine research*, International Journal of Engine Research 14 (4):307–319, 2013.
- [91] H. Chen, D.L. Reuss, V. Sick, *On the use and interpretation of proper orthogonal decomposition of in-cylinder engine flows*, Measurement Science and Technology 23 (8):85302, 2012.
- [92] P. Druault, P. Guibert, F. Alizon, *Use of proper orthogonal decomposition for time interpolation from PIV data*, Experiments in Fluids 39 (6):1009–1023, 2005.
- [93] L. Graftieaux, M. Michard, N. Grosjean, *Combining PIV, POD and vortex identification algorithms for the study of unsteady turbulent swirling flows*, Measurement Science and Technology 12 (9):1422–1429, 2001.
-

-
- [94] P.S. Abraham, X. Yang, S. Gupta, T.-W. Kuo, D.L. Reuss, V. Sick, *Flow-pattern switching in a motored spark ignition engine*, International Journal of Engine Research 16 (3):323–339, 2015.
- [95] H. Chen, M. Xu, D.L.S. Hung, H. Zhuang, *Cycle-to-cycle variation analysis of early flame propagation in engine cylinder using proper orthogonal decomposition*, Experimental Thermal and Fluid Science 58:48–55, 2014.
- [96] A. Hyvärinen, *Fast and robust fixed-point algorithms for independent component analysis*, IEEE transactions on neural networks 10 (3):626–634, 1999.
- [97] A. Hyvärinen, J. Karhunen, E. Oja, S. Haykin, *Independent Component Analysis*, John Wiley & Sons, Inc, New York, USA, 2001.
- [98] *The FastICA package for MATLAB*, A. Hyvärinen, available at <<https://research.ics.aalto.fi/ica/fastica/>>, accessed 04/04/23.
- [99] K. Bizon, G. Continillo, S. Lombardi, E. Mancaruso, P. Sementa, B.M. Vaglieco, *Independent Component Analysis of Combustion Images in Optically Accessible Gasoline and Diesel Engines*, SAE Technical Paper 2013-09-08, 2013.
- [100] A. Hyvärinen, E. Oja, *Independent component analysis: algorithms and applications*, Neural networks the official journal of the International Neural Network Society 13 (4-5):411–430, 2000.
- [101] K. Bizon, G. Continillo, S. Lombardi, P. Sementa, B.M. Vaglieco, *Independent component analysis of cycle resolved combustion images from a spark ignition optical engine*, Combustion and Flame 163:258–269, 2016.
- [102] K. Bizon, S. Lombardi, G. Continillo, E. Mancaruso, B.M. Vaglieco, *Analysis of Diesel engine combustion using imaging and independent component analysis*, Proceedings of the Combustion Institute 34 (2):2921–2931, 2013.
- [103] T. Wu, G. He, *Independent component analysis of streamwise velocity fluctuations in turbulent channel flows*, Theoretical and Applied Mechanics Letters 12 (4):100349, 2022.
- [104] M. Holický, *Introduction to Probability and Statistics for Engineers*, Springer Berlin Heidelberg, Berlin, Heidelberg, 2013.
- [105] J. Laichter, R. Rajasegar, S.A. Kaiser, A. Srna, *Optical Investigation of Mixture Preparation in a Hydrogen-Fueled Heavy-Duty Engine with Direct-Injection*, SAE Technical Paper 2023-01-0240, 2023.
- [106] J.T. Lee, Y.Y. Kim, C.W. Lee, J.A. Caton, *An Investigation of a Cause of Backfire and Its Control Due to Crevice Volumes in a Hydrogen Fueled Engine*, Journal of Engineering for Gas Turbines and Power 123 (1):204–210, 2001.
- [107] C. White, R. Steeper, A. Lutz, *The hydrogen-fueled internal combustion engine: a technical review*, International Journal of Hydrogen Energy 31 (10):1292–1305, 2006.
-

-
- [108] T. Kondo, S. Lio, M. Hiruma, *A Study on the Mechanism of Backfire in External Mixture Formation Hydrogen Engines -About Backfire Occurred by Cause of the Spark Plug-*, SAE Technical Paper 971704, 1997.
- [109] S. Verhelst, T. Wallner, *Hydrogen-fueled internal combustion engines*, *Progress in Energy and Combustion Science* 35 (6):490–527, 2009.
- [110] H.L. Yip, A. Srna, A.C.Y. Yuen, S. Kook, R.A. Taylor, G.H. Yeoh, P.R. Medwell, Q.N. Chan, *A Review of Hydrogen Direct Injection for Internal Combustion Engines: Towards Carbon-Free Combustion*, *Applied Sciences* 9 (22):4842, 2019.
- [111] N.S. Matthias, T. Wallner, R. Scarcelli, *A Hydrogen Direct Injection Engine Concept that Exceeds U.S. DOE Light-Duty Efficiency Targets*, *SAE International Journal of Engines* 5 (3):838–849, 2012.
- [112] R. Babayev, A. Andersson, A.S. Dalmau, H.G. Im, B. Johansson, *Computational characterization of hydrogen direct injection and nonpremixed combustion in a compression-ignition engine*, *International Journal of Hydrogen Energy* 46 (35):18678–18696, 2021.
- [113] S. Frankl, S. Gleis, S. Karmann, M. Prager, G. Wachtmeister, *Investigation of ammonia and hydrogen as CO₂-free fuels for heavy duty engines using a high pressure dual fuel combustion process*, *International Journal of Engine Research* 22 (10):3196–3208, 2021.
- [114] V. Salazar, S.A. Kaiser, *Influence of the Flow Field on Flame Propagation in a Hydrogen-Fueled Internal Combustion Engine*, *SAE International Journal of Engines* 4 (2):2376–2394, 2011.
- [115] Y. Wang, A. Evans, A. Srna, A. Wehrfritz, E. Hawkes, X. Liu, S. Kook, Q.N. Chan, *A Numerical Investigation of Mixture Formation and Combustion Characteristics of a Hydrogen-Diesel Dual Direct Injection Engine*, SAE Technical Paper 2021-01-0526, 2021.
- [116] H. Obermair, R. Scarcelli, T. Wallner, *Efficiency Improved Combustion System for Hydrogen Direct Injection Operation*, SAE Technical Paper 2010-01-2170, 2010.
- [117] M. Fischer, S. Sterlepper, S. Pischinger, J. Seibel, U. Kramer, T. Lorenz, *Operation principles for hydrogen spark ignited direct injection engines for passenger car applications*, *International Journal of Hydrogen Energy* 47 (8):5638–5649, 2022.
- [118] X. Liu, A. Srna, H.L. Yip, S. Kook, Q.N. Chan, E.R. Hawkes, *Performance and emissions of hydrogen-diesel dual direct injection (H₂DDI) in a single-cylinder compression-ignition engine*, *International Journal of Hydrogen Energy* 46 (1):1302–1314, 2021.
- [119] Y. Takagi, M. Oikawa, R. Sato, Y. Kojiya, Y. Mihara, *Near-zero emissions with high thermal efficiency realized by optimizing jet plume location relative to combustion chamber wall, jet geometry and injection timing in a direct-injection hydrogen engine*, *International Journal of Hydrogen Energy* 44 (18):9456–9465, 2019.
- [120] S. Lee, G. Kim, C. Bae, *Effect of injection and ignition timing on a hydrogen-lean stratified charge combustion engine*, *International Journal of Engine Research* 23 (5):816–829, 2022.
-

-
- [121] T. Tsujimura, Y. Suzuki, *Development of a large-sized direct injection hydrogen engine for a stationary power generator*, International Journal of Hydrogen Energy 44 (22):11355–11369, 2019.
- [122] H.L. Yip, A. Srna, X. Liu, S. Kook, E.R. Hawkes, Q.N. Chan, *Visualization of hydrogen jet evolution and combustion under simulated direct-injection compression-ignition engine conditions*, International Journal of Hydrogen Energy 45 (56):32562–32578, 2020.
- [123] W. Kirchweger, R. Haslacher, M. Hallmannsegger, U. Gerke, *Applications of the LIF method for the diagnostics of the combustion process of gas-IC-engines*, Experiments in Fluids 43 (2-3):329–340, 2007.
- [124] A. Hamzehloo, P.G. Aleiferis, *Computational Study of Hydrogen Direct Injection for Internal Combustion Engines*, SAE Technical Paper 2013-01-2524, 2013.
- [125] S. Lee, G. Kim, C. Bae, *Behavior of hydrogen hollow-cone spray depending on the ambient pressure*, International Journal of Hydrogen Energy 46 (5):4538–4554, 2021.
- [126] V. Salazar, S.A. Kaiser, *Interaction of Intake-Induced Flow and Injection Jet in a Direct-Injection Hydrogen-Fueled Engine Measured by PIV*, SAE Technical Paper (2011-01-0673), 2011.
- [127] A. Wimmer, T. Wallner, J. Ringler, F. Gerbig, *H₂-Direct Injection – A Highly Promising Combustion Concept*, SAE Technical Paper 2005-01-0108, 2005.
- [128] S.K. Addepalli, Y. Pei, Y. Zhang, R. Scarcelli, *Multi-dimensional modeling of mixture preparation in a direct injection engine fueled with gaseous hydrogen*, International Journal of Hydrogen Energy 47 (67):29085–29101, 2022.
- [129] A. Hamzehloo, P.G. Aleiferis, *Large eddy simulation of highly turbulent under-expanded hydrogen and methane jets for gaseous-fuelled internal combustion engines*, International Journal of Hydrogen Energy 39 (36):21275–21296, 2014.
- [130] R. Whitesides, R.P. Hessel, D.L. Flowers, S.M. Aceves, *Application of gaseous sphere injection method for modeling under-expanded H₂ injection*, Combustion Theory and Modelling 15 (3):373–384, 2011.
- [131] K. Nasrifar, *Comparative study of eleven equations of state in predicting the thermodynamic properties of hydrogen*, International Journal of Hydrogen Energy 35 (8):3802–3811, 2010.
- [132] G.M. Kosmadakis, E.G. Pariotis, C.D. Rakopoulos, *Heat transfer and crevice flow in a hydrogen-fueled spark-ignition engine: Effect on the engine performance and NO exhaust emissions*, International Journal of Hydrogen Energy 38 (18):7477–7489, 2013.
- [133] J. Le Moine, P.K. Senecal, S.A. Kaiser, V.M. Salazar, J.W. Anders, K.I. Svensson, C.R. Gehrke, *A Computational Study of the Mixture Preparation in a Direct-Injection Hydrogen Engine*, Journal of Engineering for Gas Turbines and Power 137 (11), 2015.
-

-
- [134] T. Lucchini, G. D'Errico, M. Fiocco, *Multi-Dimensional Modeling of Gas Exchange and Fuel-Air Mixing Processes in a Direct-Injection, Gas Fueled Engine*, SAE Technical Paper 2011-24-0036, 2011.
- [135] C.L. Genzale, R.D. Reitz, M.P.B. Musculus, *Optical Diagnostics and Multi-Dimensional Modeling of Spray Targeting Effects in Late-Injection Low-Temperature Diesel Combustion*, SAE International Journal of Engines 2 (2):150–172, 2009.
- [136] C. Espey, J.E. Dec, *Diesel Engine Combustion Studies in a Newly Designed Optical-Access Engine Using High-Speed Visualization and 2-D Laser Imaging*, SAE Technical Paper 1993-03-01, 1993.
- [137] J.E. Dec, *A Conceptual Model of DI Diesel Combustion Based on Laser-Sheet Imaging**, SAE Technical Paper 970873, 1997.
- [138] T. Benzler, T. Dreier, C. Schulz, *UV absorption and fluorescence properties of gas-phase p-difluorobenzene*, Applied Physics B 123 (1), 2017.
- [139] L. Itani, *Development and application of optical diagnostic techniques for assessing the effects of preferential evaporation of multi-component fuels under engine-relevant conditions*, Dissertation, University of Duisburg-Essen, 2015.
- [140] V.M. Salazar, S.A. Kaiser, F. Halter, *Optimizing Precision and Accuracy of Quantitative PLIF of Acetone as a Tracer for Hydrogen Fuel*, SAE International Journal of Fuels and Lubricants 2 (1):737–761, 2009.
- [141] E. Franquet, V. Perrier, S. Gibout, P. Bruel, *Free underexpanded jets in a quiescent medium: A review*, Progress in Aerospace Sciences 77:25–53, 2015.
- [142] W. Hwang, J.E. Dec, M. Sjöberg, *Fuel Stratification for Low-Load HCCI Combustion: Performance & Fuel-PLIF Measurements*, SAE Technical Paper 2007-01-4130, 2007.
- [143] R. Rajasegar, Y. Niki, J.M. Garcia-Oliver, Z. Li, M. Musculus, *Spatio-Temporal Progression of Two-Stage Autoignition for Diesel Sprays in a Low-Reactivity Ambient: n-Heptane Pilot-Ignited Premixed Natural Gas*, SAE Technical Paper 2021-01-0525, 2021.
- [144] T. Wallner, A.M. Nande, J. Naber, *Evaluation of Injector Location and Nozzle Design in a Direct-Injection Hydrogen Research Engine* SAE Technical Paper 2008-06-23, 2008.
- [145] J. Laichter, S. Kaiser, R. Rajasegar, A. Srna, *Impact of Mixture Inhomogeneity and Ignition Location on Early Flame Kernel Evolution in a Direct-Injection Hydrogen-Fueled Heavy-Duty Optical Engine*, SAE Technical Paper 2023-32-0044, 2023.
- [146] A. Mohammadi, M. Shioji, Y. Nakai, W. Ishikura, E. Tabo, *Performance and combustion characteristics of a direct injection SI hydrogen engine*, International Journal of Hydrogen Energy 32 (2):296–304, 2007.
- [147] S. Verhelst, P. Maesschalek, N. Rombaut, R. Sierens, *Efficiency comparison between hydrogen and gasoline, on a bi-fuel hydrogen/gasoline engine*, International Journal of Hydrogen Energy 34 (5):2504–2510, 2009.
-

-
- [148] S. Verhelst, *Recent progress in the use of hydrogen as a fuel for internal combustion engines*, International Journal of Hydrogen Energy 39 (2):1071–1085, 2014.
- [149] T. Wallner, A.M. Nande, J. Naber, *Study of Basic Injection Configurations using a Direct-Injection Hydrogen Research Engine*, SAE International Journal of Engines 2 (1):1221–1230, 2009.
- [150] V.M. Salazar, S.A. Kaiser, *Influence of the In-Cylinder Flow Field (Tumble) on the Fuel Distribution in a DI Hydrogen Engine Using a Single-Hole Injector*, SAE International Journal of Engines 3 (1):309–325, 2010.
- [151] S. Faust, T. Dreier, C. Schulz, *Photo-physical properties of anisole: temperature, pressure, and bath gas composition dependence of fluorescence spectra and lifetimes*, Applied Physics B 112 (2):203–213, 2013.
- [152] K.H. Tran, C. Morin, M. Kühni, P. Guibert, *Fluorescence spectroscopy of anisole at elevated temperatures and pressures*, Applied Physics B 115 (4):461–470, 2014.
- [153] Q. Wang, K.H. Tran, C. Morin, J. Bonnety, G. Legros, P. Guibert, *Predicting fluorescence quantum yield for anisole at elevated temperatures and pressures*, Applied Physics B 123 (7), 2017.
- [154] S. Faust, M. Goschütz, S.A. Kaiser, T. Dreier, C. Schulz, *A comparison of selected organic tracers for quantitative scalar imaging in the gas phase via laser-induced fluorescence*, Applied Physics B 117 (1):183–194, 2014.
- [155] P. Kumar, P. Anil Kishan, M. Nikhil Mathew, A. Dhar, *Flame kernel growth study of spark ignited hydrogen air premixed combustion at engine conditions*, Thermal Science and Engineering Progress 21:100769, 2021.
-

7.2 Contributions of the author

Journal articles

- [74] J. Laichter, S.A. Kaiser, *Optical Investigation of the Influence of In-cylinder Flow and Mixture Inhomogeneity on Cyclic Variability in a Direct-Injection Spark Ignition Engine*, *Flow Turbulence Combust* 110, 171–183, 2023, doi:10.1007/s10494-022-00344-8.
I carried out the experiments, post-processed and visualized the data. I wrote the first draft and was responsible for managing the paper.
- [85] J. Laichter, S.A. Kaiser, *Statistical analysis of flow field variations via independent component analysis*, submitted to *Experiments in Fluids*, 30.10.2023, doi: 10.21203/rs.3.rs-3512583/v1.
I developed most of the methodology, wrote most of the first draft and was responsible for managing the paper.
- [105] J. Laichter, R. Rajasegar, S.A. Kaiser, and A. Srna, *Optical Investigation of Mixture Formation in a Hydrogen-Fueled Heavy Duty Engine with Direct-Injection*, SAE Technical Paper 2023-01-0240, 2023.
This paper was selected for 2024 issue 2 of SAE International Journal of Advances and Current Practices in Mobility.
I carried out the experiments, post-processed and visualized the data. I wrote most of the first draft and was responsible for managing the paper.
- [145] J. Laichter, S.A. Kaiser, R. Rajasegar, and A. Srna, *Impact of Mixture Inhomogeneity and Ignition Location on Early Flame Kernel Evolution in a Direct-Injection Hydrogen-Fueled Heavy-Duty Optical Engine*, SAE Technical Paper 2023-32-0044, 2023.
This paper was selected for 2024 issue 4 of SAE International Journal of Advances and Current Practices in Mobility.
I carried out the experiments, post-processed and visualized the data. I wrote the first draft and was responsible for managing the paper.
- [156] Engelmann, L., Laichter, J., Wollny, P. et al. *Cyclic Variations in the Flame Propagation in an Spark-Ignited Engine: Multi Cycle Large Eddy Simulation Supported by Imaging Diagnostics*, *Flow Turbulence Combust* 110, 91–104, 2023, <https://doi.org/10.1007/s10494-022-00350-w>.
This study investigates CCV in an SI engine using experimental measurements and large eddy simulations. High-speed imaging captures flame characteristics, while simulations provide data on flame and kinetic energy. I performed the experiment, processed and analyzed the data and Linus Engelmann and I compared the data in discussions. I wrote the section on the experimental set up and reviewed the manuscript.
-

*Conference contributions*Paper including oral presentation:

J. Laichter, S.A. Kaiser, *Investigation of cyclic variations in a direct-injection spark-ignition engine by high-speed optical diagnostics*, in 30. Deutscher Flammentag, September 28th – 29th 2021, online.

Paper including poster presentation:

J. Laichter, C. Schulz, S.A. Kaiser, *Investigation of cyclic variations in a direct-injection spark-ignition engine by high-speed optical diagnostics*, in Proceedings of the European Combustion Meeting 2021, April 14th – 15th 2021, online.

Oral presentations:

J. Laichter, S.A. Kaiser, *Investigation of cyclic variability in a spark-ignited engine via independent component analysis*, at the FOR 2687 Workshop – Cyclic variations in highly optimized spark-ignition engines, October 6th – 7th 2022, Aachen, Germany.

J. Laichter, S.A. Kaiser, R. Rajasegar, and A. Srna, *Optical Investigation of Mixture Formation in a Hydrogen-Fueled Heavy Duty Engine with Direct-Injection*, at the SAE World Congress Experience 2023, April 18th – 20th 2023, Detroit, MI, USA.

J. Laichter, S.A. Kaiser, R. Rajasegar, and A. Srna, *Impact of Mixture Inhomogeneity and Ignition Location on Early Flame Kernel Evolution in a Direct-Injection Hydrogen-Fueled Heavy-Duty Optical Engine*, at the Powertrains, Energy and Lubricants International Meeting 2023, August 29th – September 1st 2023, Kyoto, Japan.

Poster:

J. Laichter, S.A. Kaiser, *Investigation of cyclic variation in a spark-ignition engine via independent component analysis*, at the 39th International Symposium on Combustion 2022, July 24th – 29th 2022, Vancouver, Canada.

Supervised theses

A.E. Sahin, *Untersuchung des Strömungsfeldes in einem optisch zugänglichen Ottomotor mit Direkteinspritzung durch Hochgeschwindigkeits-PIV*, bachelor's thesis, University of Duisburg-Essen, 2021.

S. Bahar, *Ein Konzept zur laserbasierten Zündung in einem Versuchs-Ottomotor*, bachelor's thesis, University of Duisburg-Essen, 2021.

8 Appendix

20 bar

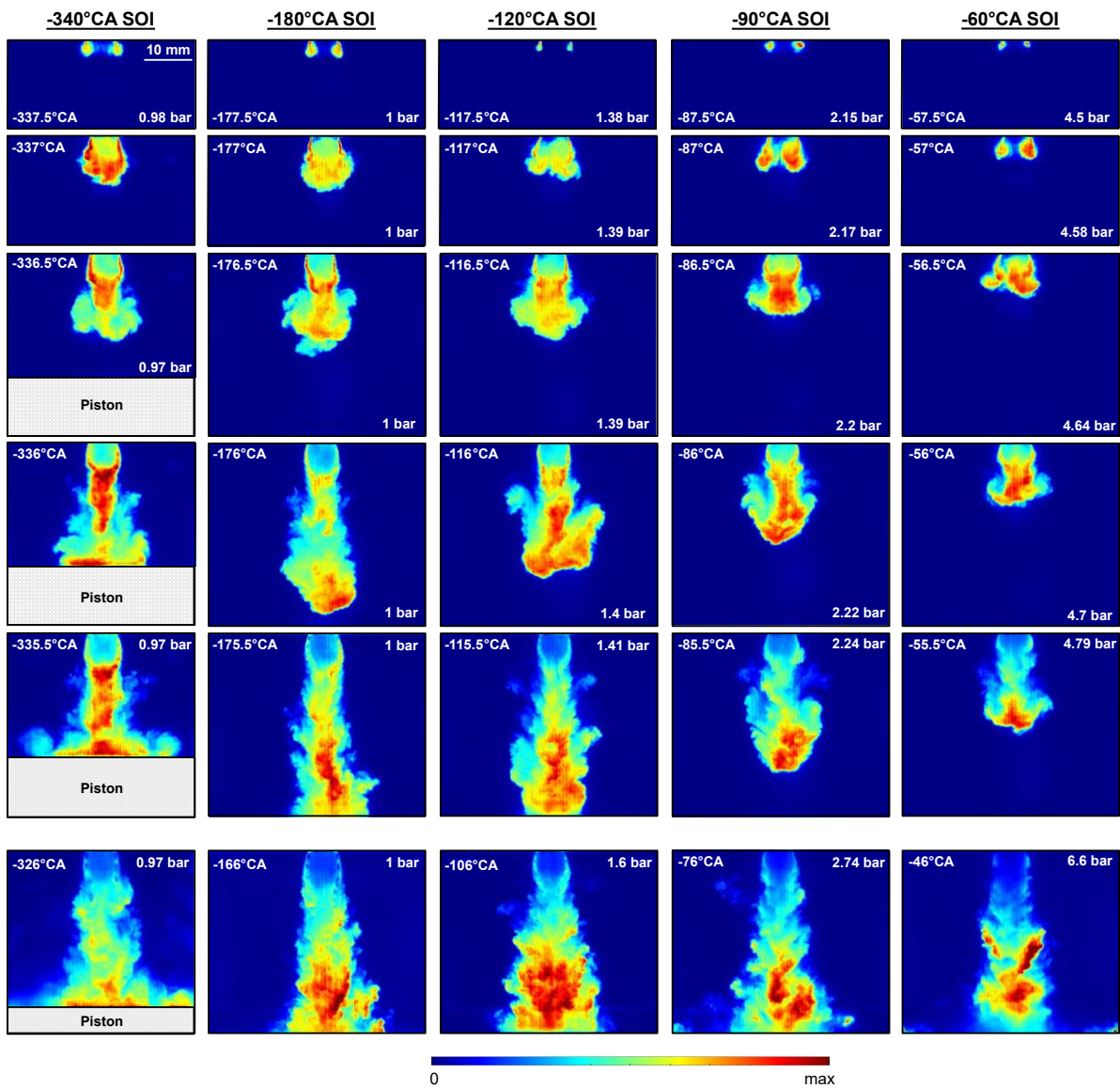


Figure 51. Qualitative single shots of the equivalence ratio in the vertical plane during the injection event for different injection timings with 20 bar injection pressure. The top 5 rows show the early injection while the bottom-row images were taken halfway through the injection event in the “quasi-steady” phase. Note that each image is from a different cycle. Each image is normalized at roughly its own maximum intensity value. For each image, crank angle and measured in-cylinder pressure are given.

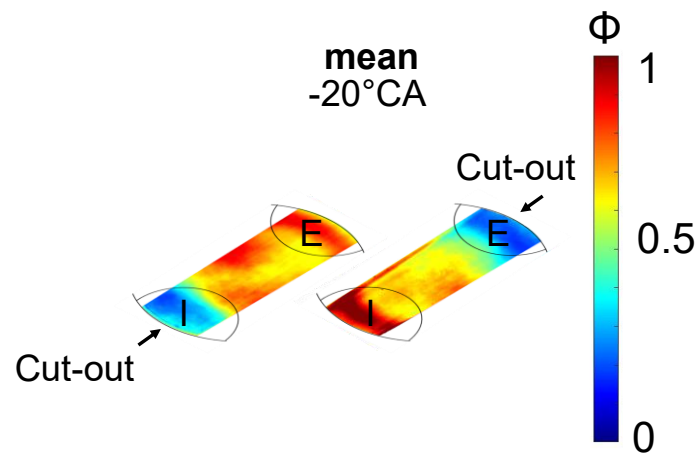


Figure 52. The effect of bowl-rim cut-out position on ensemble-averaged equivalence ratio distribution at -20°CA with -60°CA SOI 14 mm below the fire deck. Image on the left was acquired using the standard configuration used throughout this work. The right image was acquired in a configuration where the cut-out location was rotated by 180° , so it is located on the engine exhaust side. The approximately mirrored equivalence ratio distribution suggests that the cutout significantly affects the observed asymmetric mixture distribution.

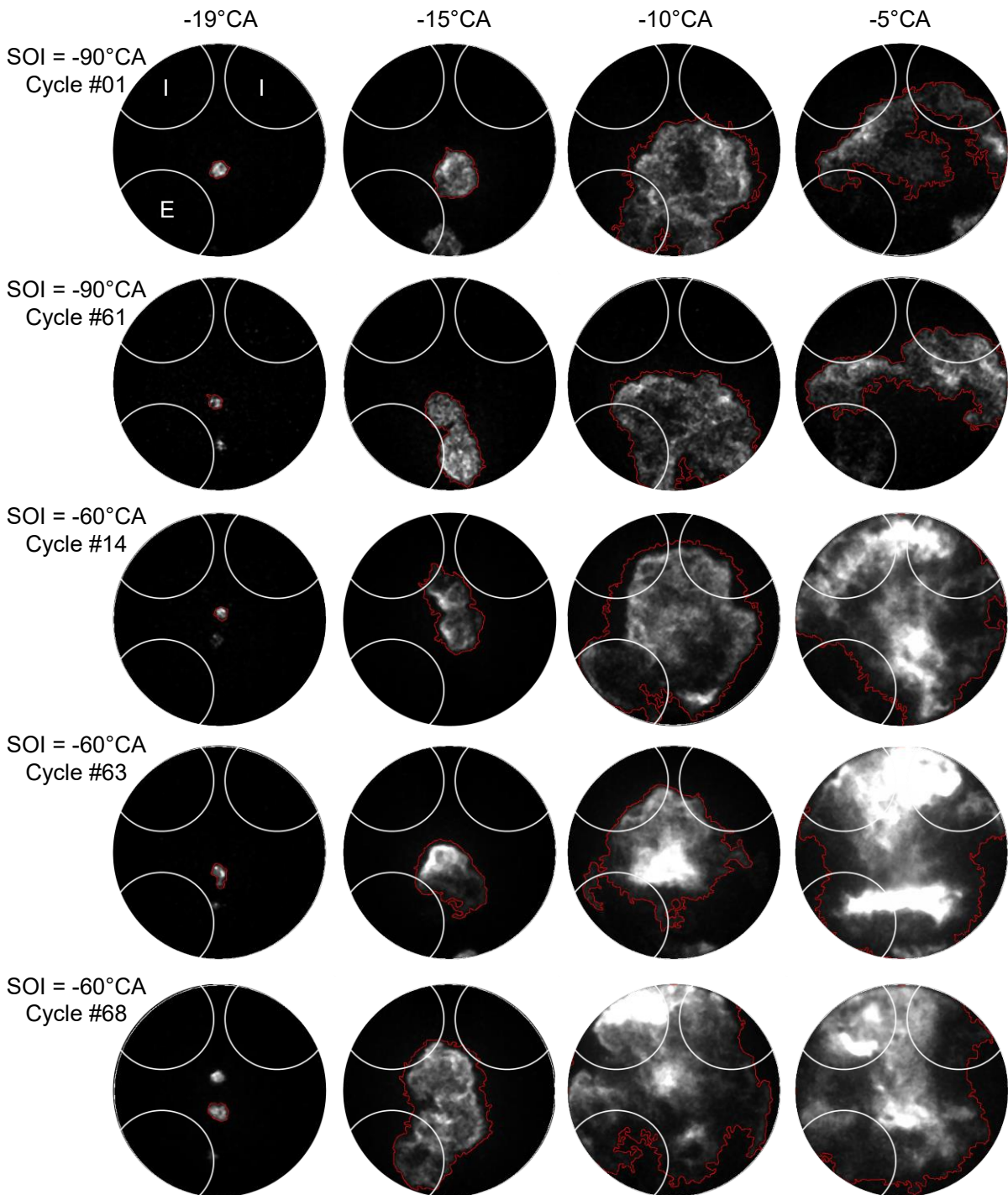


Figure 53. Examples of additional ignition spots from experiments with 40 bar injection pressure and different SOIs. The original ignition location is in the center. The red line indicates the detected flame area.

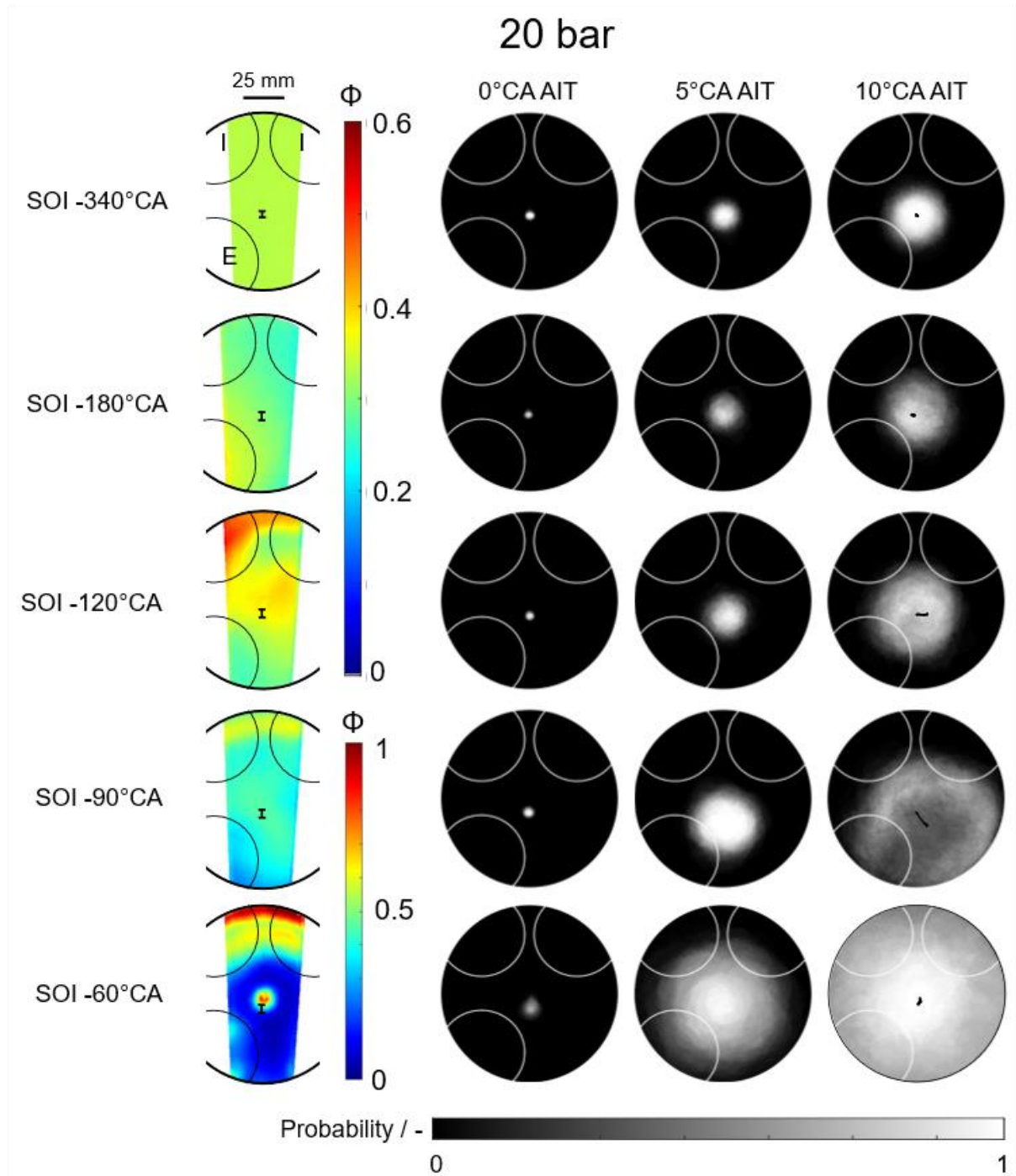


Figure 54. Average equivalence ratio for different injection timings with 20 bar injection pressure and corresponding probability of finding the burnt gas area at different $^{\circ}\text{CA}$ AIT. The spark location is in the center and marked in black within the equivalence ratio. Additionally, the flame centroids from 0 to 10 $^{\circ}\text{CA}$ AIT are marked in the burnt gas area 10 $^{\circ}\text{CA}$ AIT.

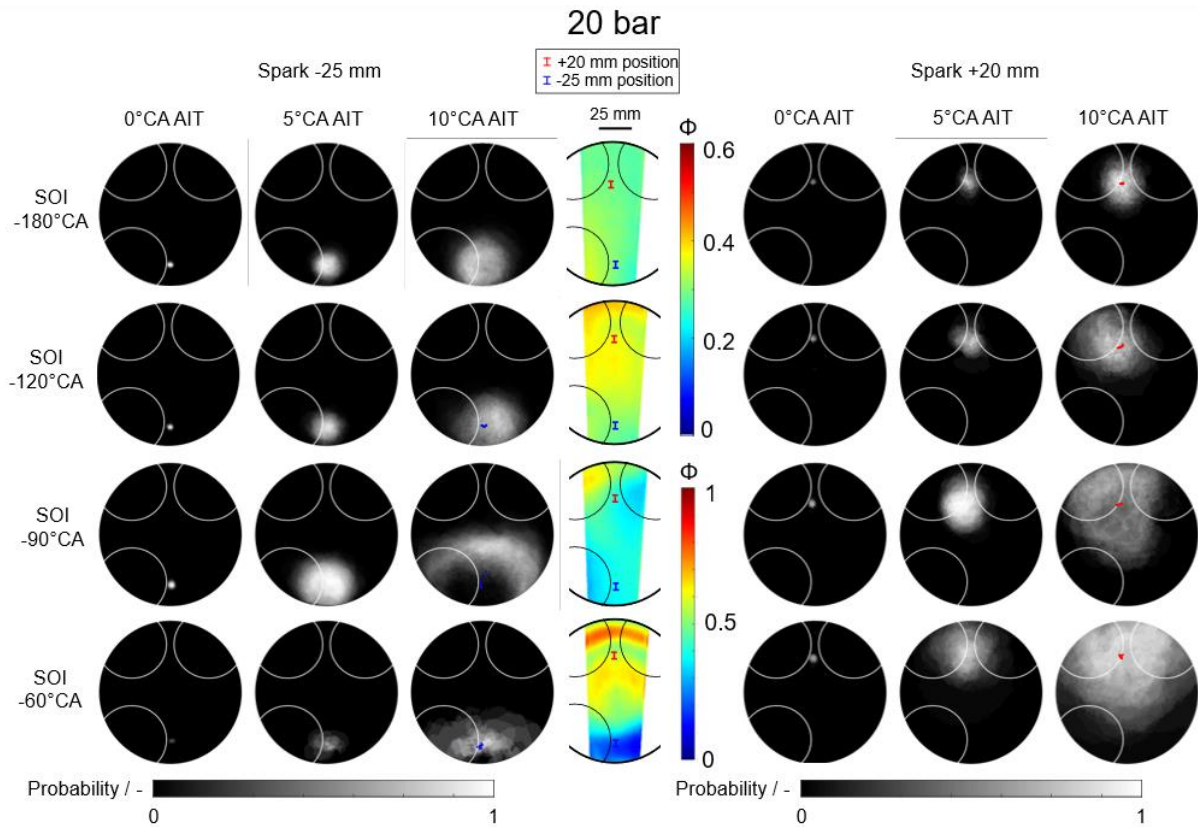


Figure 55. Average equivalence ratio and corresponding probability of finding the burnt gas area for different injection timings at 20 bar injection pressure and (left three columns) the -25 mm ignition location and (right three columns) the 20 mm ignition location (marked in green and blue within the equivalence ratio). Additionally, the flame centroids from 0 to 10°CA AIT are marked for (red) fast and (blue) slow cycles in the burnt gas area 10°CA AIT.

DuEPublico

Duisburg-Essen Publications online

UNIVERSITÄT
DUISBURG
ESSEN

Offen im Denken

ub | universitäts
bibliothek

Diese Dissertation wird via DuEPublico, dem Dokumenten- und Publikationsserver der Universität Duisburg-Essen, zur Verfügung gestellt und liegt auch als Print-Version vor.

DOI: 10.17185/duepublico/81746

URN: urn:nbn:de:hbz:465-20240314-080155-9

Alle Rechte vorbehalten.